The Measurement of Time Delays in Gravitational Lenses

by

Christopher B. Moore

S.B. Physics
Massachusettts Institute of Technology, 1990

Submitted to the Department of Physics
in partial fulfillment of the requirements for the degree of

Doctor of Philosophy

at the

MASSACHUSETTS INSTITUTE OF TECHNOLOGY

September 1996

Author.......
Department of Physics
12 August 1996

Certified by . ...
Jacqueline N. Hewitt
Associate Professor of Physics
Thesis Supervisor

Accepted by.......... ....
George F. Koster
Professor of Physics
Chairman, Departmental Committee on Graduate Students

The Measurement of Time Delays in Gravitational Lenses

by

Christopher B. Moore

S.B. Physics

Massachusettts Institute of Technology, 1990

Submitted to the Department of Physics
on 12 August 1996, in partial fulfillment of the
requirements for the degree of
Doctor of Philosophy

Abstract

This thesis describes two sets of observations directed at the measurement of a time delay in the gravitational lens MG0414+0534 as well as the design of an experiment to measure time delays due to microlensing of distant quasars by compact masses in an intervening galaxy.

The first MG0414 monitoring experiment, a 63 epoch 15 GHz VLA observation, fails to detect any reliable indication of variability or a time delay. The other, an 82 epoch 8 GHz VLA observation allowed for a number of improvements reducing the observational errors but still fails to make a clear detection of variability. We have demonstrated that flux calibration using a model of the flux calibrator can greatly improve the stability of flux calibration at both 15 and 8 GHz yielding $< 1\%$ flux calibration errors for some VLA configurations at 8 GHz. Novel deconvolution techniques developed here and demonstrated on these data are able to make reliable measurements of flux densities when the resolution is low and tradititional techniques fail. Residual deconvolution errors are measured on simulated data and found to be $<0.6\%$ for the 8 GHz data. Application of these techniques to monitoring of other lensing systems will result in much lower noise and therefore much better determination of cosmological parameters.

In the final chapter, we show that microlensing time delays of order tens of μ-seconds should be detectable by phase coherent radio autocorrelation using large radio telescopes if there are high brightness temperature sources and compact masses in an intervening galaxy or galaxy halo. Detection of microlensing time delays would provide evidence for super-Compton brightness temperatures and compact masses in the lens as well as give limited information on the structure of the high-brightness temperature parts of the source.

Thesis Supervisor: Jacqueline N. Hewitt
Title: Associate Professor of Physics

Acknowledgments

This thesis is dedicated to my parents and is in no small measure a direct result of their unwavering care and support.

My advisor, Jackie Hewitt, introduced me graduate research by giving me the opportunity to explore a number of different projects before settling on this one. Her guiding hand is seen throughout this work. Ed Bertschinger, a member of my thesis committee, also made important contributions by pointing the way in directions which were very fruitful. John Negele, also a member of the committee, brought a view from outside astrophysics and made a number of important points that improved the thesis. My ideas on image deconvolution were shaped by fruitful discussions with Daniel Briggs and Rick Perley of NRAO.

My fellow graduate students have made graduate school more enjoyable, entertaining, and survivable. In particular, Edward Ajhar, Chris Becker, Grace Chen, Sam Conner, John Ellithorpe, Debbie Haarsma, Charlie Katz, and Bob Rutledge were invaluable resources, study partners, and friends.

My experience at M.I.T. would have been much less without the presence of John Corley and Bob Newman. John, the director of the M.I.T. Concert Band, introduced me to modern music which I will always love. He also provided an environment for enjoyable music making that extended well beyond the band. Bob is a great friend who showed me the art of photography and the joy of making photographs. He spent countless hours teaching me the art of fine printing and to him I owe a large measure of the continuing joy I receive from participating in and observing the visual arts.

I arrived at M.I.T. with the idea that blowing glass might be fun. The M.I.T. Glass Laboratory (started by Michael Cima) gave me the opportunity to develop this notion into a passion for glassblowing that will last a lifetime. I have spent many wonderful hours blowing glass with Page Hazelgrove, Peter Houk, and Mike Binnard. They have been my teachers as well as my friends.

I would also like to thank my Longfellow Park friends who accepted me and showed me that I belonged where I feared I did not.

Contents

List of Figures

List of Tables

Chapter 1

Gravitational Lensing

1.1 Introduction

The idea that path of light rays might be affected by gravitational fields was first proposed by Newton based on his "corpuscular" theory of light. By assuming that light is composed of material particles subject to Newtonian gravity, Soldner (1804) calculated the gravitational deflection of a beam of light passing near a massive body. This calculation was incorrect by only a factor of two. The magnitude of the effect was first correctly worked out by Einstein (1915) as a consequence of the theory of General Relativity. He found that in the weak field limit the bending angle, $\hat{\alpha}$, of a light ray passing a distance, b, from a point mass was

$$\hat{\alpha} = \frac{4GM}{c^2 b}. \tag{1.1}$$

This led to the prediction that a light ray grazing the surface of the Sun would be deflected by $1.7''$ and to an attempt to measure the apparent positions of stars near the limb of the Sun during a total solar eclipse. This measurement was carried out by Eddington in 1919. As predicted, the stars near the limb of the sun appeared radially displaced from their nominal positions by an amount that was too large to be consistent with the prediction of Soldner. Even though the errors in the original observation amounted to about 30%, this result was one of the great early successes of the general theory. Modern observations accomplished with radio interferometry have verified the general relativistic prediction to better than 0.1% (Lebach *et al.* 1995).

Since the image separations produced by stars acting as gravitational lenses are so small, gravitational lensing was something of a backwater until Zwicky (1937) pointed out that galaxies could also act as gravitational lenses and that the resulting images should be easily observable (see section 1.2). He also correctly predicted that lensing was common enough that it was likely to be found. The detection of the first multiple image gravitational lens candidate (Q0957+561) was announced by Walsh, Carswell & Weymann (1979) and today there are in excess of twenty well confirmed gravitational lens systems that exhibit multiple imaging (see Keeton & Kochanek (1995) for a short review).

In multiple image gravitational lens systems, the light travel times along the rays corresponding to each image are, in general, different. The measurement of the properties of the lensing potential and the difference in light travel times, the time delay, makes it possible to derive important information regarding the distance to the lens (see section 1.4). This measurement performed on several lenses at a variety of redshifts allows the extraction of important cosmological parameters.

This thesis describes two separate observational attempts to measure a time delay in the gravitational lens MG0414+0534 at 8 and 15 GHz. It also separately describes the feasibility of an experiment to detect the lensing effect of individual stars in a distant galaxy on a background quasar. The remainder of the present chapter describes gravitational lensing in general as well as the particular properties of MG0414+0534. Chapter 2 covers the theory of radio interferometry that is central to the operation of the Very Large Array(VLA[1]), the telescope that was used in the observational work reported in later chapters. Chapters 3 and 4 describe the experiment and data analysis of the 15 GHz observations of MG0414. Chapter 5 describes the 8 GHz data and chapter 6 covers the unique techniques that were used to correct for deconvolution errors in it. Chapter 7 discusses an experiment that can be performed to search for the effect of microlensing due to compact masses in a distant galaxy. In the final chapter we present a summary of the work described herein and suggestions for future work.

---

[1] The VLA is part of the National Radio Astronomy Observatory, which is operated by Associated Universities, Inc., under cooperative agreement with the National Science Foundation.

1.2 Gravitational Lensing

Consider a source of electromagnetic radiation, S, observed by an observer, O, through some intervening mass distribution (see figure 1.1). For simplicity, we will assume that the mass distribution exists in a single plane, the "lens plane," not an unreasonable assumption even for sources at cosmological distances when the lenses are galaxies or clusters of galaxies.

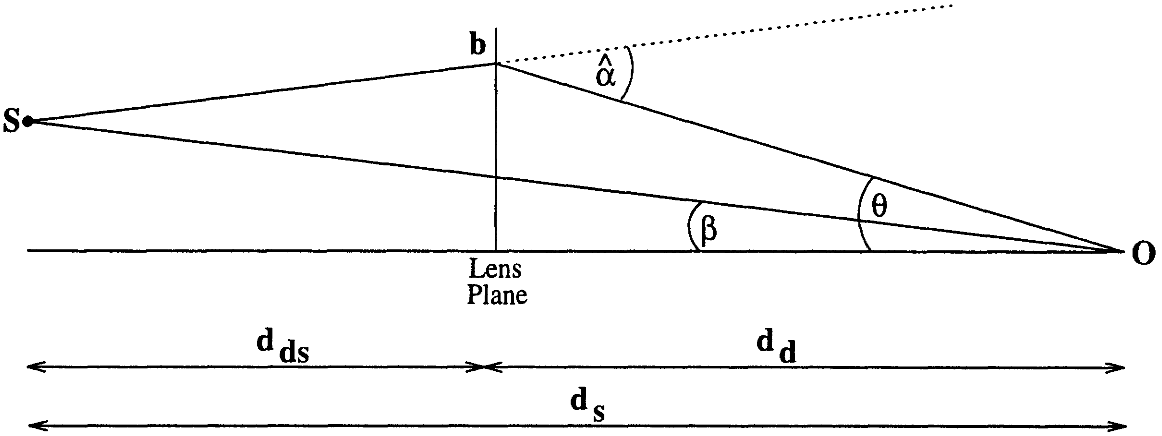

FIGURE 1.1: Lensing geometry

Taking the optical axis relative to the center of the lensing mass distribution, the source is located at an angle β relative to the optical axis but since a light ray passing the lens plane at impact parameter, b, is deflected by an angle $\hat{\alpha}(b)$, the source appears (to the observer) at angle θ. Assuming small angles, the geometrical condition for a light ray to reach the observer is then

$$\boldsymbol{\theta} d_s = \boldsymbol{\beta} d_s + d_{ds}\hat{\boldsymbol{\alpha}}(\mathbf{b}). \tag{1.2}$$

Here the distances d_s, d_d, and d_{ds} are taken to be such that the Euclidean relation between the angle enclosed by two lines and their separations holds (i.e. separation = angle × distance). When distances are *defined* in such a way that this relation holds, they are referred to as *angular-diameter distances.*

Equation 1.2 is more commonly written as

$$\boldsymbol{\beta} = \boldsymbol{\theta} - \frac{d_{ds}}{d_s}\hat{\boldsymbol{\alpha}}(\boldsymbol{\theta}), \tag{1.3}$$

where the relation $\boldsymbol{\theta} = \frac{\mathbf{b}}{d_d}$ has been used to eliminate $\mathbf{b}$ from the equation. Equation 1.3 is usually referred to as the "ray tracing" or "lensing" equation.

For a planar mass distribution, the effect of many lenses adds so using the weak field deflection angle from equation 1.1 we find that the total deflection is

$$\hat{\alpha}(\mathbf{b}) = \int_{\text{lens plane}} \frac{4G}{c^2}\Sigma(\mathbf{b}')\frac{\mathbf{b}-\mathbf{b}'}{|\mathbf{b}-\mathbf{b}'|^2}d^2\mathbf{b}', \tag{1.4}$$

where $\Sigma(\mathbf{b})$ is the two dimensional mass density that results when the lensing mass is projected onto the lens plane.

For a circularly symmetric lens, the lens equation (equation 1.3) transforms to

$$\beta(\theta) = \theta - \frac{d_{ds}}{d_d d_s}\frac{4GM(\theta)}{c^2\theta} \tag{1.5}$$

where $M(\theta)$ is the mass enclosed at some angular radius, θ. Due to the rotational symmetry of the lensing potential, a source which lies directly behind the center of the lens (on the optical axis at $\beta = 0$) is imaged into a ring. Setting $\beta = 0$ in equation 1.5 we find the radius of the ring is

$$\theta_E = \sqrt{\frac{d_{ds}}{d_d d_s}\frac{4GM(\theta_E)}{c^2}}. \tag{1.6}$$

θ_E is referred to as the Einstein radius and is a useful way of characterizing the angular scale in a lensing system since the typical image separation in a multiple image lens system is of order $2\theta_E$.

It is convenient to define the effective lensing potential which is the scaled two-dimensional Newtonian potential

$$\psi(\boldsymbol{\theta}) = \frac{d_{ds}}{d_d d_s}\frac{2}{c^2}\int \Phi(d_d\boldsymbol{\theta}, z)\mathrm{d}z \tag{1.7}$$

(Narayan & Bartelmann 1996). The total light travel time between the source and the observer for an image located at $\boldsymbol{\theta}$ is then written

$$t(\boldsymbol{\theta}) = \frac{1+z_d}{c}\frac{d_d d_s}{d_d s}\left[\frac{1}{2}(\boldsymbol{\theta}-\boldsymbol{\beta})^2 - \psi(\boldsymbol{\theta})\right]. \tag{1.8}$$

The term in square brackets separates the travel time into two convenient parts: the first is a geometric part which corresponds to the path length and the second is a gravitational part due to the passage through a gravitational potential (the Shapiro Delay). Since the intrinsic variations of the source are not accessible to observation, the only observable is the differential time delay between a pair of images.

Since surface brightness is conserved in gravitational lensing (by Liouville's theorem), the total flux of an image may change only if it is magnified by the lens. Consider a small source lensed by a circularly symmetric lens. The solid angle subtended by the source is $\Delta\beta \times \beta\Delta\varphi$ where $\beta\Delta\varphi$ is the size of the source perpendicular to direction to the center of the lens. The size of an image is $\Delta\theta \times \theta\Delta\varphi$ so the magnification factor, μ, is given by

$$\mu = \frac{\Delta\theta \times \theta\varphi}{\Delta\beta \times \beta\varphi} = \frac{\theta}{\beta}\frac{d\theta}{d\beta}. \tag{1.9}$$

1.2.1 The Schwarzschild Lens

The simplest lens is the point mass or Schwarzschild Lens. In this case,

$$\hat{\alpha}(b) = \frac{4GM}{c^2 b}. \tag{1.10}$$

and the lensing equation can be rewritten in the form

$$\beta(\theta) = \theta - \frac{\theta_E^2}{\theta}. \tag{1.11}$$

The images appear at the solutions to this equation, namely

$$\theta_\pm = \frac{1}{2}\left(\beta \pm \sqrt{\beta^2 + 4\theta_E^2}\right). \tag{1.12}$$

The magnification of the Schwarzschild lens can be found by using equation 1.11 to substitute for β in equation 1.9 obtaining,

$$\mu_\pm = \left[1 - \left(\frac{\theta_E}{\theta_\pm}\right)^4\right]^{-1}. \tag{1.13}$$

We see that all sources are imaged twice by the point mass lens. The two images are located on either side of the optical axis with one image located at $\theta < \theta_E$ and the other with $\theta > \theta_E$. When β is near zero, the two images appear highly magnified near $\theta = \theta_E$. As β increases, one of the images approaches $\theta = 0$ and becomes very faint ($\mu \rightarrow 0$) while the other approaches $\theta = \beta$ and tends toward the unlensed brightness of the source ($\mu \rightarrow 1$).

1.2.2 Lensing by Galaxies

Since the lenses in multiply imaged systems are typically galaxies or clusters of galaxies, the basic properties of simple galaxy lenses are of interest. The simplest models of galaxy potentials are based on the isothermal sphere. Here (following Narayan & Bartelmann (1996)) we assume that the stars (and other matter) in a galaxy act like an ideal gas of particles in a spherically symmetric gravitational potential. If this is the case, the "pressure" is

$$p = NkT \tag{1.14}$$

where N is the number density of stars and T is the "temperature" of the stars. If the system is in local thermal equilibrium, we can relate the line-of-sight velocity dispersion to the temperature of the stars by

$$\frac{1}{2}m\sigma_v^2 = \frac{1}{2}kT \tag{1.15}$$

where m is the particle mass. If one assumes that the temperature is uniform throughout the galaxy, the equation of hydrostatic equilibrium looks like

$$\mathrm{d}p = -\frac{GM(r)}{r^2}mN\mathrm{d}r \tag{1.16}$$

where $M(r)$ is the mass enclosed at a radius r and

$$\mathrm{d}M = 4\pi r^2 mN\mathrm{d}r. \tag{1.17}$$

A simple solution to the above set of equations for the case of the ideal gas is

$$N(r) = \frac{\sigma_v^2}{2\pi Gm}\frac{1}{r^2}. \tag{1.18}$$

This distribution has the advantage of arranging the total mass enclosed $M(r)$ to be proportional to r so that the Keplarian rotation speed is constant as is observed in galaxies. However, the number density (and therefore the mass density) is non-physically singular at $r = 0$. If we project the mass onto a plane, we obtain the surface mass density

$$\Sigma(b) = \frac{\sigma_v^2}{2G}\frac{1}{b}, \tag{1.19}$$

where b is the distance from the center of the mass distribution. By inserting this into equation 1.4, one can find that the deflection angle due to this mass distribution is independent of b. There can at most be two images of the source with the center of the lens lying on the line that connects them. The lens equation has a two-image solution only when $\beta < \theta_E$ and the images are located at

$$\theta_{\pm} = \beta \pm \theta_E. \tag{1.20}$$

There is a third image at $\theta = 0$, but it has $\mu = 0$ for the case of the singular isothermal sphere. If the potential is "softened" by replacement of the singularity at the center of the potential with a finite density core, then the third image appears with $\mu \neq 0$.

Given the range of galaxy shapes, it is clearly unlikely that the singular or softened isothermal sphere or any circularly symmetric potential will describe galaxy potentials. The existence of lensing galaxies which produce more than two images of a single source is strong observational evidence for this point. In order to produce the image configurations that are observed, we are forced to consider potentials which do not have circular symmetry. Popular choices for potential models include flattened isothermal spheres and circular isothermal spheres plus quadrupole terms which provide the symmetry breaking necessary to generate more than two images.

1.3 Microlensing

The term "microlensing" is usually applied to lensing by small compact masses (e.g. stars) either in isolation or as part of a larger lensing potential (e.g. a galaxy). Since the Einstein ring radius for a solar mass lens in the Galaxy is only ~1 mas, the typical image separations are of order 2 mas. Such separations are difficult to measure with present instruments so to date microlensing has been detected only by an increase in the total flux of the unresolved pair of images. This increase in flux is expected because the surface brightness of the images is conserved in lensing and the magnification of the lens can result in more total area (at constant surface brightness) being present in the unresolved lens images than in the unlensed source. In order to detect microlensing events in this way, one must observe a changing flux that is consistent with the expectation for a lens passing along the line of sight. Since lensing is achromatic, the changing flux should be the same even in different optical colors as long as the source structure is the same in different colors (true at least for approximate black body emitters like stars). The timescale for a microlensing event is just the time for the lens to cross its own Einstein ring. For stellar lenses in our own galaxy, the timescale is days but for stellar lenses in external galaxies, the timescale is tens to hundreds of years. This makes microlensing by extra-galactic lenses difficult to distinguish from intrinsic source variability.

Since detection of extra-galactic microlenses by flux variation is so difficult and the probability of galactic microlensing is so small, researchers have been forced to use large field optical lens searches that monitor the brightness of millions of stars in the galactic bulge or the Large Magellanic Cloud. Since Paczyński (1986b) suggested that detection of the intervening lensing masses can be used to characterize the number and distribution of lensing masses in the Galactic halo, four groups[2] have undertaken the task of measuring microlensing-induced stellar variability. Their results have been used to characterize the distribution of compact masses in the halo of the Galaxy. To date, these searches have detected ~100 microlensing events including a few that appear to be best explained by lenses which are binary star systems.

In chapter 7 of this work, we describe the design of an experiment to detect microlensing in external galaxies. Since the timescales for microlensing events in extragalactic microlenses are long, one must attempt to detect them by some means which avoids confusion with source variability. One such possibility is through the time delay associated with each of the lens images. For solar-mass lenses in external galaxies, the time delays are on the order of microseconds. By examining the coherent autocorrelation function of an unresolved distant source, one could can determine if there are time delays in the signal that are characteristic of some sort of multipath. This multipath might be due to interstellar scintillation or gravitational microlensing time delays. The distinction between scintillation and microlensing can be made by changing the observing frequency since gravitational lensing is achromatic and scintillation is not. Furthermore, the timescale for a change in a true microlensing signal can be made manageable by examining it at very high temporal resolution (and thus wide bandwidth) and there is no confusion with intrinsic source variability.

---

[2] OGLE (Udalski *et al.* 1992),MACHO (Alcock *et al.* 1993), EROS (Aubourg *et al.* 1993), and DUO (Alard *et al.* 1995).

1.4 Time Delays and Cosmography

Well before the first gravitational lens was discovered, Refsdal (1964a; 1964b) pointed out that, given a model of the lensing potential and the redshift of both the source and the lens, a measurement of the difference in optical path length between two images in a gravitational lens could be used to determine the Hubble parameter in the context of a particular cosmological model. More recently, Narayan (1991) has shown that a time delay measurement combined with a model of the lensing potential and the redshift of the lens provides a unique measure of the angular diameter distance to the lens that is independent of the redshift of the source and cosmological assumptions other than local isotropy and homogeneity transverse to the line of sight. Thus, lens models combined with time delay measurements measure the relationship between angular diameter distance and redshift. The measurement of the angular diameter distance—redshift relation at a variety of lens redshifts will allow the comparison of the measured relation to that predicted by cosmological models. Figure 1.2 shows the angular diameter distance—redshift relation for a variety of cosmological models. Large-scale structure contributes to the deflection and time delays in strong lensing (Seljak 1994; Bar-Kana 1996). This effect would introduce some scatter (of order 5% RMS) in the measured angular diameter distance–redshift relation that will require a large set of lenses to extract the cosmological parameters but also makes it possible to detect the effect of large-scale structure on lens time delays.

Given the evidence based on primordial nucleosynthesis that baryonic matter can account for at most $\frac{0.026}{h^2}$ of the critical density (Kolb & Turner 1990), it would be interesting if lensing time delay measurements could place $\Omega_0 > \frac{0.026}{h^2}$ in a convincing fashion. If we take $h = .5$, (as a worst case) then we want to show that $\Omega_0 > 0.10$. Such a result would require the difference between the measured value and 0.10 to be made up of non-baryonic matter. If $\Omega_0 = 0.25$, then to make a 3σ measurement of $\Omega_0 > 0.10$, we need to measure Ω_0 to 20%. If we measure $\Omega_0 = 1.0$, then a measurement with 30% error will suffice to demonstrate that $\Omega_0 > 0.10$.

In order to illustrate the precision necessary to do this with a time delay measurement in a single gravitational lens, we assume $H_0 = 100\,\mathrm{km\,s^{-1}\,Mpc^{-1}}$ and the lens redshift of the gravitational lens 2016+112, $z_l = 1.01$. Figure 1.3 shows the values of Ω_0 that would be implied by different measured angular-diameter distances to the lens. Since the

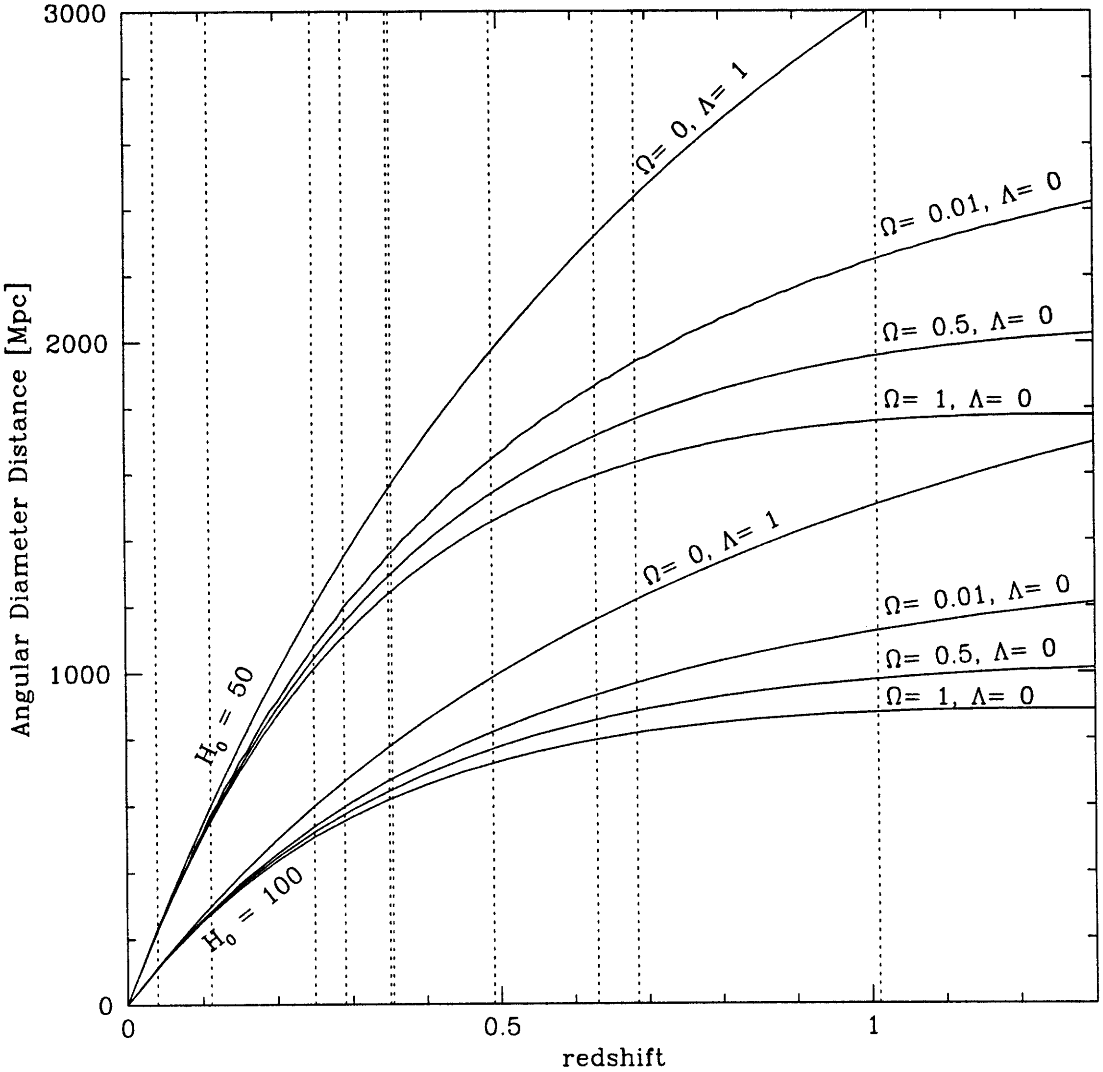

FIGURE 1.2: Angular Diameter Distance vs. Redshift for a variety of cosmological models. Vertical dotted lines mark the positions of known lens redshifts.

relationship between the time delay and measured angular diameter distance is linear and the relationship between angular-diameter distance and Ω_0 is nearly linear, errors in the measurement of a time delay contribute directly to errors in the derived value of Ω_0.

The total error in the conversion of a gravitational lens time delay to an angular-diameter distance comes from an unavoidable contribution of large-scale structure (5–10%), the errors in the model of the lensing potential (including the measurement of the velocity dispersion),

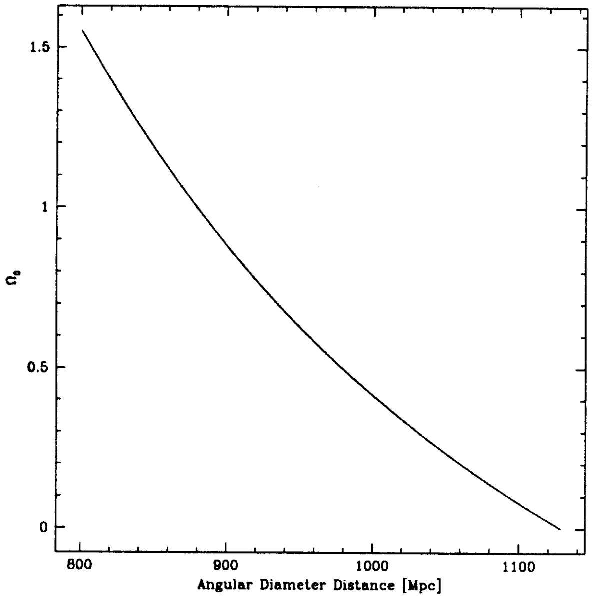

FIGURE 1.3: Values of Ω_0 that would be implied by different measured angular-diameter distances for $z_l = 1.01$, $H_0 = 100\,\mathrm{km\,s^{-1}\,Mpc^{-1}}$, and $\Lambda = 0$.

and the error in the determination of the time delay. The best studied system to date is Q0957+561 where the potential is complicated since it is a cluster lens and the modelling errors are presently thought to be about 9% including the uncertainty in the measurement of the velocity dispersion (Grogin & Narayan 1996). It is possible that high resolution structures, simpler lensing potentials, and extended structures will contribute to better models for this and other lenses. Since the errors add in quadrature, the 20% uncertainty required to separate $\Omega_0 = 0.25$ from $\Omega_0 = 0.10$ at 3σ requires a measurement of the time delay with 15–17% uncertainty depending on the contribution of large-scale structure. For a 5% measurement of a time delay then we could achive an error on Ω_0 of 11–14% depending on the contribution of large-scale structure. These uncertainties are clearly achievable for lenses with sufficient variability. If other lensing potentials prove easier to model than 0957+561, then the error might be reduced dramatically. The full picture is somewhat more complicated since the error due to large-scale structure increases with lens redshift and multiple time delays will be necessary in order to fit for H_0, Ω_0, and Λ.

1.5 MG 0414+0534

For a time delay measurement we have selected the gravitational lens MG 0414+0534 (hereafter MG0414), a source that was culled from the MIT–Greenbank survey (Bennett *et al.* 1986) in a gravitational lens search (Hewitt *et al.* 1988) and followed up with optical and radio observations. The object consists of four bright, highly reddened images with very similar radio spectra and optical colors. These characteristics, along with the striking morphology and relative brightnesses of the images, were taken as early evidence that the object is indeed a gravitational lens (Hewitt *et al.* 1992). A 15 GHz radio image of MG0414 is displayed in Figure 1.4.

Further observations have supported the conclusion that MG0414 is a gravitationally lensed system and MG0414 is now well established as such. Schechter & Moore (Schechter & Moore 1993) report optical (I-band) observations at the Michigan-Dartmouth-MIT observatory at Kitt Peak that detected the lensing galaxy at nearly the expected position and detected the presence of another object near component B (dubbed "X"). They also report the somewhat curious result that the A1:A2 flux ratio is very different in the optical ($\sim$2.2) than in the radio observations described below where the ratio is 1.1–1.3. Angonin-Willaime, *et al.* (1994) report confirmation of the optical results of Schechter & Moore (including the detection of component "X") as well as optical spectroscopy which shows that the spectra of A1+A2 and B are similar. Lawrence, *et al.* (1995b) suggest that the source is a fairly typical quasar that is highly reddened by dust in the lensing galaxy but other observers suggest that the reddening is intrinsic to the source (see for example, Vanderriest, *et al.* (1995) and Annis, *et al.* (1993)). Falco, Lehár & Shapiro (1996) (hereafter FLS96) detect an optical arc in Hubble Space Telescope images that is substantially bluer than the images of the core. They argue that the difference in color combined with the proximity of the arc and core sources argues in favor of intrinsic reddening.

The redshift of the source in MG0414 has been measured by Lawrence, *et al.* (1995b) at 2.639 ± 0.002. A number of attempts to measure the redshift of the lensing galaxy have been made but thus far but none has been successful (Lawrence *et al.* 1995a). The HST data of FLS96 confirm the flux ratios found by other optical observers and resolve component "X" thus identifying it as a galaxy which might contribute to the lensing potential in the system.

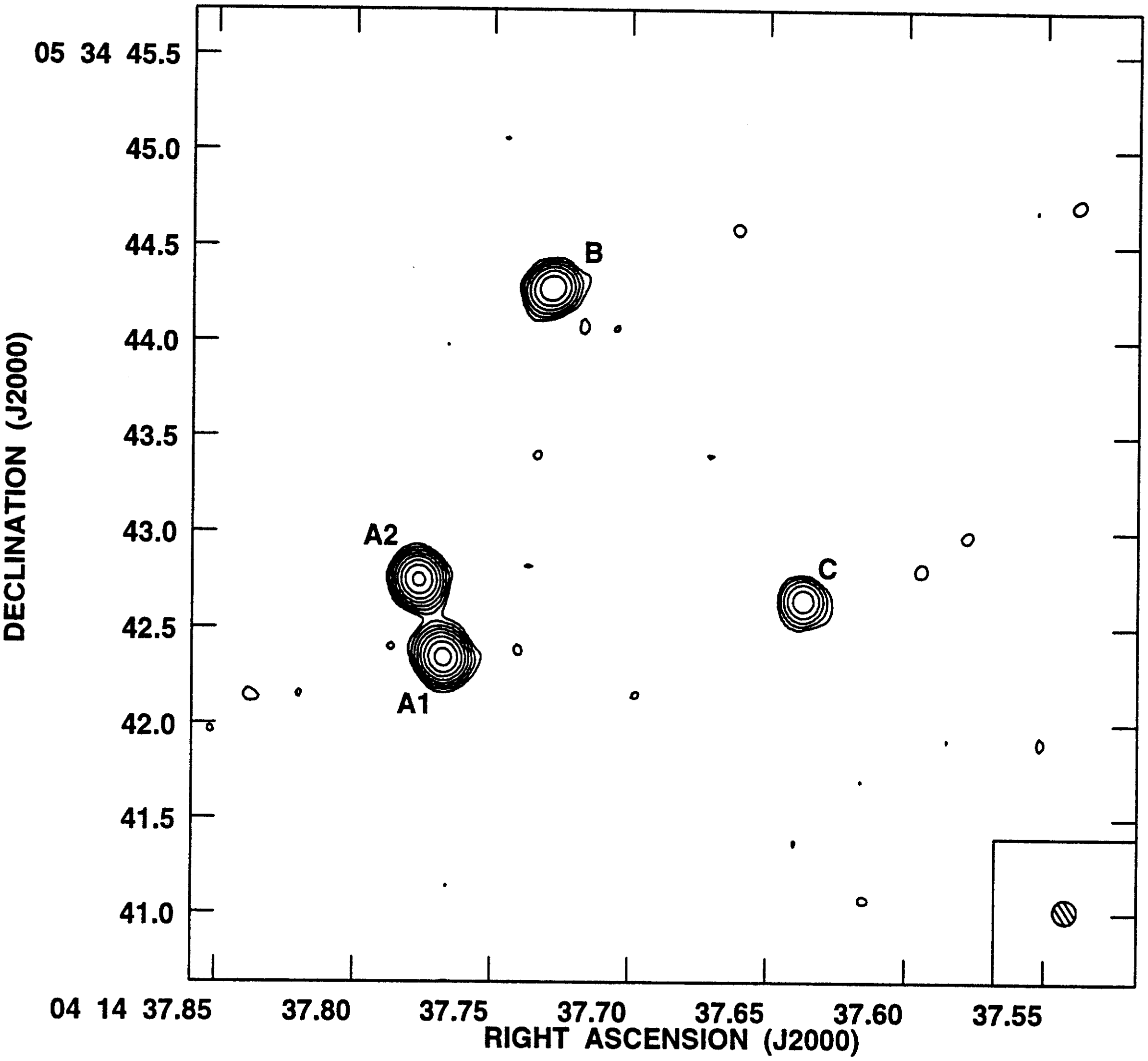

FIGURE 1.4: A 15 GHz (VLA A-array) map of MG0414 produced in the course of the present work (observation date 15 Dec 1992). The contours correspond to flux densities of 0.8, 1.6, 3.2, 6.4, 12.8, 25.6, 51.2, and 102.4 mJy. The circle in the lower right corner illustrates the size of the synthesized beam for this observation (.15″×.14″).

Radio observations by Katz & Hewitt (1993) were the first to confirm that the close double (components A1 and A2) is indeed a double as expected from lens models. Sensitive radio observations at 1.4, 5, 8, 15, and 22 GHz by Katz, Moore & Hewitt (1996) have failed to detect any large scale extended structure that might be useful for lens modelling but do find structure in the images that appears consistent with the optical arc detected in the HST images of FLS96. Katz, *et al.* also suggest that the source in MG0414 is a GHz-

Peaked Spectrum (GPS) source and that such an interpretation would be consistent with the reddening in the system being intrinsic.

MG0414 is well suited to relating time delay measurements to angular diameter distances since the morphology of the system argues for a relatively simple lensing potential (particularly compared to Q0957+561). Furthermore, VLBI studies of the object are underway which may reveal structure that would place constraints on models of the lensing potential (Ellithorpe 1995; Patnaik & Porcas 1995).

At the beginning of this project, there were few observations of MG0414 and it was difficult to tell from them if the object was indeed variable. We therefore based our expectation of variability on the statistical properties of similar sources. In a flux limited sample of extragalactic radio sources, Aller, *et al.* (1992) find greater than 10% variability at 14.5 GHz in 76% of the sample with the fraction dropping to 50% at 4.8 GHz. This is only part of the story since the optical classification of the sources is a very powerful indicator of variability. All eight of the BL Lacs and all but one of the 27 QSO's were variable at the 10% level. The initial classification of MG0414 as a BL Lac-like object gave further confidence that it would be variable. It shoud be noted, however that this was a long term monitoring project including 6.4–24 years of data on each object and that even variable objects are known to display short periods of stability. The later identification of MG0414 as a GPS source (Katz *et al.* 1996) reduces the likelihood of variability since GPS sources as a class are thought to have less variability than other QSO's (O'Dea *et al.* 1991).

1.5.1 Lens Models and Predicted Time Delays

The following material on simple models of the lens in MG0414 is derived from Moore & Hewitt (1996). Kochanek (1991) has fit five simple models of the lensing potential in MG0414 using *only* the positions of the images as constraints for reasons of computational speed and lack of reliable data on the flux ratios. The models fall into two classes: those in which image B is at a minimum of the time delay surface (models 2, 3, and 4) and those in which it is at a saddle point (models 1 and 5). In order to illustrate the difference between the two classes of models we show Kochanek's model 1 (Singular Isothermal Sphere + Internal Quadrupole) and model 3 (Singular Isothermal Sphere + External Quadrupole). Model 1 is the standard singular isothermal sphere (see section 1.2.2 with the symmetry broken by the addition of a quadrupole term due to matter located inside the Einstein ring.

In model 3, the symmetry is broken by a quadrupole due to matter located outside the Einstein ring. Since Kochanek does not publish the fitted source positions, we estimate the source position by computing the source position implied by each observed image. Images A1, A2, and B give consistent estimates of the source position and we take their average as our estimate (0.053″,−0.050″ from the lens center for model 1 and −0.13″,0.046″ for model 3). Figure 1.5 shows the lensing potentials for both models (from Kochanek's fits) and our estimated source position. Even though the position angles of the potentials differ by approximately 90°, the radial deflections and therefore the Einstein rings generated by these models are nearly aligned.

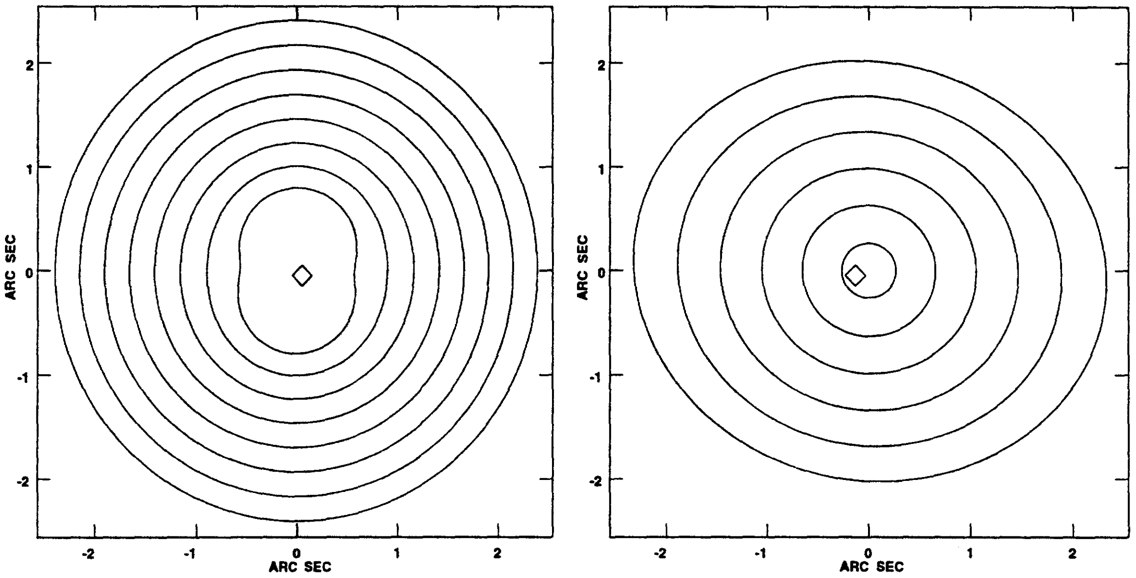

FIGURE 1.5: The gravitational potential for Kochanek's model 1 (left) and model 3 (right). The contours are equipotentials which are equivalent (in the weak field limit) to lines of constant index of refraction. The diamond signifies our estimated source position. The central detail in model 1 has been suppressed in order to make the source position visible.

Figure 1.6 displays the time delay surfaces corresponding to the Kochanek's models 1 and 3. By the Fermat principle, images are formed at the extrema (marked) of the time delay surface. Both models can reproduce the positions of the images, but they do so very differently: saddle points and minima are exchanged in the two time delay surfaces. The B:C flux ratio predicted by Kochanek's models 1 and 5 (.58 and .51 respectively) is inconsistent with our observations where the measured flux ratio is 2.53. Models 2, 3, and 4

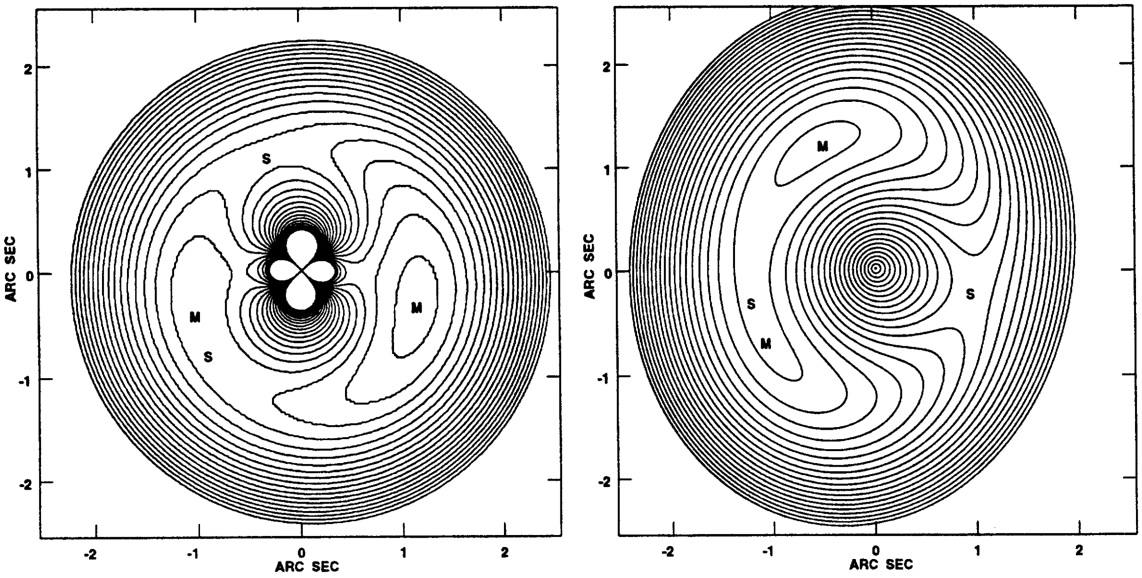

FIGURE 1.6: The time delay surface for Kochanek's model 1 (left) and model 3 (right) using the assumed source positions shown in Figure 1.5. Extrema (with the exception of the central maximum) are labelled "M" for minimum and "S" for saddle point.

come closer to the measured B:C flux ratio (2.2–3.2) but fail to correctly predict the A1:A2 flux ratio. The very large magnification gradient in the neighborhood of A1 and A2 should make the flux ratio of A1:A2 difficult to model.

The models which are consistent with the measured flux ratios predict that flux variations should be observed first in image B, followed next by images A1 & A2, and finally in image C. The model of the system by Hewitt, *et al.* (1992) predicts (for $H_0 = 80\,\mathrm{km\,s^{-1}Mpc^{-1}}$, $q_0 = 0.5$, empty beam) that images B and A2 lead A1 by 12 and 0.3 days respectively and that image C lags A1 by 19 days. It should be noted that the model upon which these estimates are based should be taken to be illustrative only since it assumes a lens redshift ($z_l = 0.47$) and does not exactly reproduce the observed geometry and flux ratios of the system.

Using a different set of 15 GHz VLA data Ellithorpe (1995) finds that his best model for the lensing potential gives a time delay between B and A1 of 10.3 ± 1.4 days (B leads) for the H_0, q_0, and z_l given above.

Chapter 2

Radio Interferometry

2.1 Introduction

The diffraction limited angular resolution of practical single radio antennas is at best a few tens of arcseconds–not adequate for many studies of astronomical sources. However, multiple radio telescopes combined in synthesis arrays (really an ensemble of different two element interferometers) have made possible sub-milliarcsecond observations radio sources. This resolution is unsurpassed at all other wavelengths. The preferential development of interferometric techniques in radio astronomy is due to the relative ease with which radio signals can be processed electronically. Shorter wavelengths (e.g. optical) present a problem since the corresponding frequencies are higher than present electronic systems can handle and because the atmospheric delays are much more significant at high frequencies. However, there have been recent advances in the application of optical interferometric techniques leading to the recent demonstration of a three element optical aperture synthesis array operating at 830 nm (Baldwin *et al.* 1996).

2.2 The Two-element Interferometer

Figure 2.1 shows a schematic diagram of a two element interferometer. The antennas are separated by $\mathbf{b}$ and a plane wave arrives from a direction denoted by a unit vector $\mathbf{s}$ from a nearly monochromatic point source. The wave reaches the antenna labeled "1" before the one labelled "2" because the geometric path length to antenna two is longer by $c\tau_{\mathrm{geom}}$

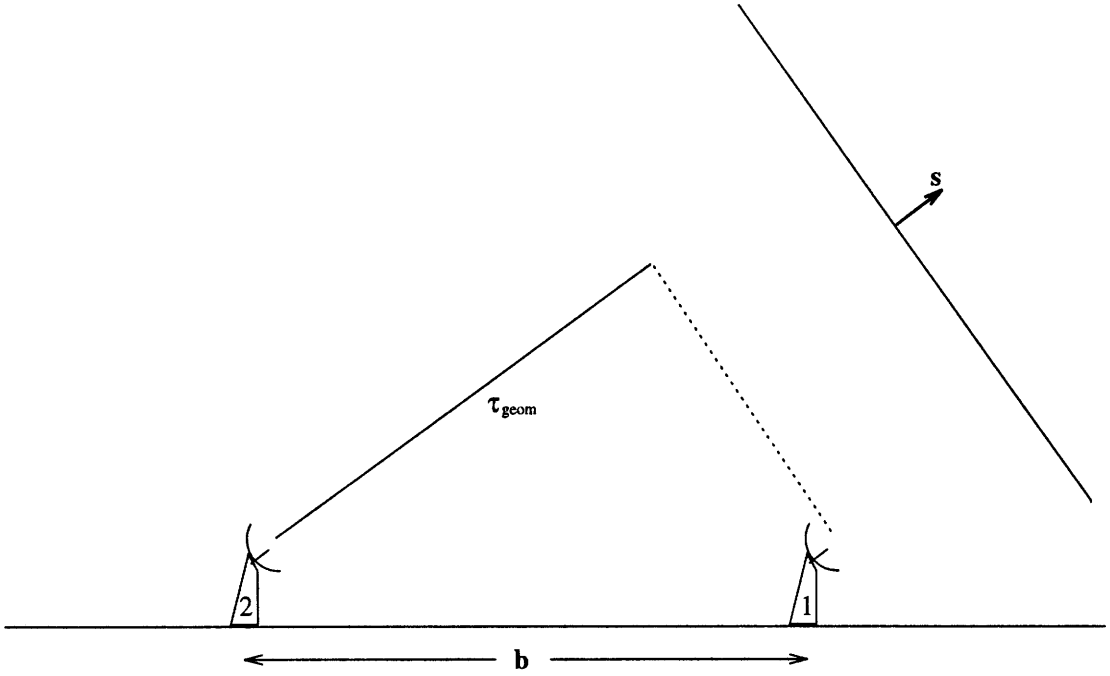

FIGURE 2.1: Schematic diagram of a two-element radio interferometer. A plane wave arrives from a source located in the **s** direction at two telescopes separated by **b**. The time delay between the arrival of the wave at the right and left telescopes is τ_{geom}.

where

$$\tau_{\text{geom}} = \frac{\boldsymbol{b} \cdot \boldsymbol{s}}{c}. \tag{2.1}$$

In order to cancel this delay, we introduce an artificial delay,

$$\tau_0 = \frac{\boldsymbol{b} \cdot \boldsymbol{s}_0}{c}, \tag{2.2}$$

into the signal from antenna 1 which has the effect of "pointing" the interferometer in the direction $\mathbf{s_0}$ independent of the mechanical pointing of the antennae (though the two are usually arranged to approximately coincide). If we observe a single polarization at angular frequency ω and the total flux received from the source in this polarization is S, then the electric fields at the antennae are

$$E_1(t) = \sqrt{S}\sin(\omega(t - \tau_0)) \tag{2.3}$$

$$E_2(t) = \sqrt{S}\sin(\omega(t - \tau_{\mathrm{geom}})) \tag{2.4}$$

If the two signals are multiplied together and averaged, we find

$$E_1(t)E_2(t) = \frac{S}{2}\left[\cos\left(\omega\left(\tau_{\mathrm{geom}} - \tau_0\right)\right) - \cos\left(\omega\left(2t - \tau_{\mathrm{geom}} - \tau_0\right)\right)\right] \tag{2.5}$$

If the arrangement is kept fixed as the earth rotates, $\tau_{\mathrm{geom}} - \tau_0$ changes as the earth rotates at the rate $\frac{|\mathbf{b}|}{c}\dot{\theta}$ where $\dot{\theta} \approx 10^{-4}\,\mathrm{rad\,s^{-1}}$. The argument of the second cosine term varies much more rapidly and thus it can be averaged out by a low-pass filter leaving only

$$\frac{S}{2}\cos(\omega(\tau_{\mathrm{geom}} - \tau_0)) = \frac{S}{2}\cos\left(\frac{2\pi}{\lambda}\mathbf{b}\cdot(\mathbf{s} - \mathbf{s_0})\right). \tag{2.6}$$

We define the visibility,

$$V_r = S\cos\left(\frac{2\pi}{\lambda}\mathbf{b}\cdot(\mathbf{s} - \mathbf{s_0})\right) \tag{2.7}$$

which is twice the filtered response since half of the response in equation 2.5 was removed by the low-pass filter. The response of V_r is limited to a sinusoidal pattern of stripes on the sky called "fringes" running parallel to the vector **b**. We can detect sources in the nulls of this fringe pattern by delaying the signal from one of the antenna in such a way as to introduce a 180° phase shift in the response function yielding,

$$V_i = S\sin\left(\frac{2\pi}{\lambda}\mathbf{b}\cdot(\mathbf{s} - \mathbf{s_0})\right). \tag{2.8}$$

We can define the total visibility to V_r and V_i as the real and imaginary parts of a complex quantity,

$$V = S\,e^{\frac{2\pi i}{\lambda}\mathbf{b}\cdot(\mathbf{s}-\mathbf{s_0})}. \tag{2.9}$$

If we restrict our consideration to points on the celestial sphere near $\mathbf{s_0}$, we may approximate the sphere by a plane tangent to the sphere at $\mathbf{s_0}$ called the tangent plane. We may then express positions on the tangent plane with a rectangular coordinate system aligned such that the positive x-axis points westward and the positive y-axis points northward. We also measure the projection of the baseline vector **b** on the plane perpendicular to $\mathbf{s_0}$ in units of λ and call the corresponding coodinates u and v.

If there is a brightness distribution, $I(x, y)$, on the tangent plane, then the visibility measured by the two element interferometer is the superposition of the response to each differential element of the source, $dxdy$, so the total response is

$$V(u,v) = \int I(x,y)e^{2\pi i(ux+vy)}\,dxdy, \tag{2.10}$$

which is the two-dimensional Fourier transform of $I(x,y)$.

2.3 Aperture Synthesis

Aperture synthesis arrays are cooperating groups of N telescopes forming $\frac{N(N-1)}{2}$ two-element interferometers. Each pair of telescopes forms an interferometer that measures $V(u,v)$ at some particular u and v determined by the geometry of the array. Since we would like to invert the Fourier transform of equation 2.10 to find $I(x,y)$, we want to measure $V(u,v)$ over the entire uv-plane. Since we only make a measurement of $V(u,v)$ where we have a baseline, we can measure it at only $\frac{N(N-1)}{2}$ points at any one time. If I(x,y) does not change rapidly, we may wait for the rotation of the Earth to move the baselines and therefore measure $V(u,v)$ over a larger area of the uv-plane. The part of the visibility that we actually measure is then picked out with a sampling function, $S(u,v)$, that contains one δ-function at every measured point in the uv-plane and is zero elsewhere. The measured visibility function is then

$$\tilde{V}(u,v) = S(u,v)V(u,v) \tag{2.11}$$

2.4 Image Deconvolution

If we attempt the inverse Fourier transform of $\tilde{V}(u,v)$ we recover the so called "dirty image,"

$$I_d = F^{-1}(\tilde{V}(u,v)) = F^{-1}\left[S(u,v)\right] * I(x,y), \tag{2.12}$$

which is the convolution of the desired function, I(x,y), with the Fourier transform of the sampling function which is called the "dirty beam." The structure of the dirty beam is quite complex and typically contains many points far from the central lobe which nevertheless have large amplitudes ("sidelobes"). In order to extract $I(x,y)$ from I_d, we are forced to resort to one of a family of deconvolution algorithms. These algorithms operate with the advantage that the convolving function is a mathematically generated by the uv-sampling and is therefore known precisely but they must also operate in the presence of noise in the observed visibilities. Two popular deconvolution algorithms are Cotton-Schwab CLEAN implemented in the AIPS task "MX" (Schwab 1984) and the Maximum Entropy Method ("MEM") discussed for example by Narayan and Nityananda (1986).

2.5 Calibration

The visibilities that we measure with a real instrument are affected by time-variable instrumental gains and delays so the measured visibilities are not quite what we expect of the source. To a good approximation, we may encapsulate the behavior of the individual antennae and their electronics as well as the physical environment in single time-variable complex gain for each antenna, $g_i(t)$. The measured visibilities are then

$$\tilde{V}_{ij} = g_i g_j^* V(u, v) \tag{2.13}$$

where $\tilde{V}_{ij}$ refers to a particular visibility measured on a baseline between two antennae, i and j. If we observe a point source (often called a "phase calibrator") at $\mathbf{s_0}$, we know that the visibility function should be constant since the Fourier transform of a δ-function in the xy-plane is a constant in the uv-plane. We may use this fact to establish a set of $\frac{N(N-1)}{2}$ equations in N unknowns which can then be solved to yield the g_i as long as $N > 2$. Since the gains change as a function of time, occasional observations of a phase calibrator are used to establish a set from which the g_i's for any visibility can be determined by interpolation.

2.5.1 Self-Calibration

The amplitude of the g_i's depends on factors which affect the total flux of the measured signal. These include atmospheric transparency, the aperture efficiency of the antenna, and the gain of the receiver system. In a properly designed interferometer operating in reasonable weather conditions, all of these factors are indeed slowly changing functions of time. The phases of the g_i's however are affected by atmospheric phase delays that may change on much shorter timescales.

Since it is desirable to spend as much of the observing time on source as possible, we may try to use the source itself as a calibrator for removing these variations in a process called "self-calibration" (Cornwell & Fomalont 1989). The idea is to use the observations of the phase calibrator (and interpolations therefrom) to make a preliminary calibration of the data. These preliminary data are then Fourier transformed and deconvolved to yield a rough estimate of $I(x, y)$ and therefore of $V(u, v)$. Using this estimate, we then modify the phases (or if we have much faith in the estimate, both the phases and amplitudes) of the g_i's to bring the observed visibilities closer to the model. We can then iterate on this process to create better estimates of $V(u, v)$ which can be used to create still better corrections to the g_i. If the estimate of $I(x, y)$ contains structures which are erroneous, the self-calibration procedure will find g_i's which support their existence and further iterations will reinforce them. There is therefore a substantial amount of art in choosing the estimates of $I(x, y)$ and the averaging intervals for the process. Sources which are dominated by compact emission are particularly good for self-calibration since the early estimates of $I(x, y)$ represent much of the flux.

2.6 Observing Bandwidth and Time Averaging Effects

Thus far, we have considered only the case of a monochromatic source observed without time averaging. Since the signal-to-noise ratio goes up with increasing bandwidth and the computational processing load goes down with time averaging, there is a temptation to observe at large bandwith with long time averaging. Unfortunately, such an approach can have detrimental effects on the images particularly for images of large fields of view and for observations utilizing long baselines.

Consider observations conducted at some finite bandwidth, $\Delta\nu$. Since the u and v coordinates of equation 2.10 are in units of λ, we choose the uv-coordinates using the wavelength corresponding to the central frequency of the bandpass, ν_0. If we consider emission at some frequency, v, in the bandpass then we assign the visibility we measure from that emission to (u_0, v_0) even though it corresponds to some other (u, v). The actual (u, v) is related to (u_0, v_0) by

$$u_0 = \frac{\nu_0}{\nu} u \tag{2.14}$$

and

$$v_0 = \frac{\nu_0}{\nu} v. \tag{2.15}$$

Because the correlation process and the Fourier transform are linear, we can consider the effect of each small part of the bandpass separately. When we take the Fourier transform of the measured visibilities to get the dirty image, we have

$$F^{-1}\left[\tilde{V}\left(\frac{\nu_0}{\nu}u, \frac{\nu_0}{\nu}v\right)\right] = \frac{\nu^2}{\nu_0^2} I_d\left(\frac{\nu}{\nu_0}x, \frac{\nu}{\nu_0}y\right) \tag{2.16}$$

by the similarity theorem of Fourier transforms (Thompson 1989). This effect, "bandwidth smearing," smears the image radially with respect to the phase tracking center ($\mathbf{s_0}$). The angular size of the smearing is approximately $\frac{\Delta\nu}{\nu_0}\sqrt{x^2+y^2}$ where the bandwidth is $\Delta\nu$. The effect becomes important when the smearing is comparable to the size of the synthesized beam. Therefore, we require that

$$\Delta\nu\sqrt{x^2+y^2} < \frac{c}{D} \tag{2.17}$$

where D is the size of the longest interferometric baseline (Thompson 1989). Since the effect increases with distance from the phase tracking center, it limits the useful field of view. One can reduce the problem by a factor of n by lowering the bandwidth by a factor of n and then increasing the number of correlators by the same factor to make the same total observed bandwith. For large arrays (large N), this increase in the number of correlators can be extremely costly.

The computational burden in the Fourier transform and deconvolution procedure can be reduced by reducing the number of visibilites by time averaging them. Since the point in the uv-plane that a particular pair of antennas is measuring changes as the earth rotates, the image will suffer some distortion. For the special case of a source near the north celestial pole, an averaging time Δt results in an annular smearing of the image with angular extent of about $\omega_e\Delta t\sqrt{x^2+y^2}$ where ω_e is the angular velocity of the Earth's rotation (Thompson 1989). Again, this effect limits the field of view, but this time the details depend on the position of the source on the sky and the orientation of the baselines. For the simple case of a polar source, we require that the smearing be smaller than the synthesized beam and find that

$$\omega_e\Delta t\sqrt{x^2+y^2} < \frac{c}{\nu_0 D}. \tag{2.18}$$

2.7 The Very Large Array

The Very Large Array (VLA) is a 27-element aperture synthesis array located outside of Socorro, New Mexico. The antennae are arranged in a "Y" shaped pattern that gives a good range of baselines for imaging even observations that are too short for rotation of the Earth to change the positions of the baselines in the uv-plane. The array is reconfigured over time through a series of four configurations called the A, B, C, and D arrays at approximately four month intervals. The scales these arrays vary by the ratios of 32:10:3.2:1. All antennae are capable of observing at wavelengths of 90, 20, 6, 3.6, 2.0, and 1.2 cm and a few are now equipped with 0.7 cm receiver systems.

For the observations reported here, the field of view is approximately $1''$, the maximum baseline (in A-array) is 35 km, the averaging is 10 seconds, the observing frequencies are 8 and 15 GHz, and the bandwidth per correlator is 50 MHz. Given these parameters and the information in the previous section, it is easy to show that the effect of bandwidth smearing is 35 times smaller than the synthesized beam. The smearing due to time averaging is even less significant, a factor of 300 smaller than the synthesized beam at 8 GHz.

Chapter 3

Observations of MG 0414+0534 at 15 GHz

3.1 Introduction

The 15 GHz monitoring observations of MG0414 were planned at a time when the VLA monitoring observations of 0957+561 had been successful in observing 5 GHz variability over a long temporal baseline (Lehár *et al.* 1992). Observed lightcurves (both optical (Vanderriest *et al.* 1989; Schild 1990) and radio) showed clear features indicative of the presence of a time delay and drove the development of several new time delay estimation techniques (Press *et al.* 1992b; Schild 1990; Hjorth *et al.* 1992).

Our monitoring observations were planned to utilize the VLA because the large number of antennae and their physical configuration allow deep images of simple sources to be obtained in short observations (30–60 minutes including calibration) and the size of the array makes it possible to resolve images with small separations. The choice of 15 GHz makes it possible to resolve the A1/A2 pair even when the array is reconfigured to B-array and seemed to be a good trade-off between expectation for variability (higher for higher frequencies) and instrumental difficulties (worse for higher frequencies).

3.2 Observations

The observations were planned without knowledge of the lens redshift and were therefore planned to be sensitive to time delays in the range 12–60 days. The total time spanned by the observing program and the sampling interval were chosen so that for a reasonable range of lens redshifts (z_l = 0.3–1.2), at least one pair of images would have a measurable time delay. Simulations indicated that these delays would be easily detectable if the structure function (see section 4.4) were similar to that observed in 0957+561.

We observed MG0414 at 15 GHz with the VLA starting on 1992 November 8 in its most extended (A-array) configuration, continuing through the second most extended (B-array) configuration, and ending on 1993 May 3. The central frequencies for the two observing bands were the standard VLA U-band values of 14.9649 and 14.9149 GHz, each with 50 MHz bandwidth. Each band was observed in both senses of circular polarization bringing the total observed bandwidth to 100 MHz in each polarization. There were a total of 63 individual observations each of 0.5 to 1.5 hours duration. This program was scheduled into small interstices in the VLA schedule resulting in observations occurring over a wide range of hour angle and with no particular sampling pattern (see Table 3.1). We have found that, in practice, an irregular sampling pattern is desirable because it minimizes windowing effects in the time delay analysis.

Date	Julian Date −244000	Source Elevation (degrees)	Synthesized Beam ($''$)	Date	Julian Date −244000	Source Elevation (degrees)	Synthesized Beam ($''$)
1992 NOV 02	8928.674	13–19	.35 × .23	1993 FEB 01	No Data		
NOV 03	No Data			FEB 03	9021.685	50–52	.48 × .24
NOV 04	8930.997	28–34	.27 × .25	FEB 06	9024.677	50–52	.50 × .30
NOV 07	No Data	60–62	.16 × .13	FEB 09	9027.690	40–44	.58 × .26
NOV 13	8939.772	47–50	.15 × .13	FEB 12	9030.533	50–52	.45 × .23
NOV 14	8940.894	53–55	.15 × .13	FEB 14	9032.665	40–48	.53 × .38
NOV 18	8944.738	50–52	.16 × .15	FEB 15	9033.673	40–44	.59 × .40
NOV 23	8949.744	47–50	.22 × .22	FEB 18	9036.707	29–34	.56 × .50
NOV 24	8950.971	22–26	.33 × .20	FEB 19	9037.522	50–54	.72 × .33
NOV 25	8951.864	53–55	.16 × .14	FEB 23	9041.704	23–33	.39 × .39
NOV 26	8952.692	37–41	.15 × .15	FEB 27	9045.661	35–39	.43 × .37
NOV 27	8953.963	25–28	.32 × .20	MAR 05	9052.473	50–52	.40 × .39
NOV 29	8955.707	50–52	.15 × .13	MAR 09	9056.357	29–34	.69 × .67
NOV 30	8956.850	53–55	.16 × .14	MAR 15	9062.474	52–55	.39 × .32
DEC 03	8959.754	52–54	.17 × .17	MAR 18	9065.501	54–55	.41 × .33
DEC 07	No Data			MAR 24	9070.575	40–44	.38 × .35
DEC 13	8969.814	48–50	.16 × .14	MAR 31	9077.535	44–48	.43 × .35
DEC 15	8971.845	43–48	.15 × .14	APR 01	9078.539	40–48	.45 × .35
DEC 16	8972.617	32–36	.14 × .14	APR 03	9081.334	34–41	.45 × .35
DEC 24	8980.533	20–24	.35 × .22	APR 05	9083.476	52–54	.38 × .33
DEC 27	8983.673	51–53	.17 × .14	APR 06	9084.494	49–52	.37 × .33
DEC 29	8985.602	37–41	.14 × .14	APR 11	9089.516	40–44	.44 × .35
1993 JAN 04	8991.671	53–54	.16 × .14	APR 12	9090.499	45–48	.37 × .34
JAN 06	8993.634	49–53	.17 × .14	APR 15	9093.491	45–48	.39 × .34
JAN 07	8994.699	54–55	.17 × .15	APR 19	9097.417	54–55	.38 × .34
JAN 11	8999.514	23–30	.27 × .22	APR 20	9098.498	44–48	.35 × .33
JAN 16	No Data			APR 22	9100.493	40–44	.38 × .34
JAN 19	No Data			APR 24	9102.343	58–59	.43 × .39
JAN 21	9008.704	49–51	.16 × .14	APR 27	9105.315	47–49	.38 × .34
JAN 24	9011.607	60–61	.17 × .16	APR 29	9107.286	48–52	.41 × .35
JAN 30	9017.614	54–55	.42 × .25	MAY 01	9109.247	29–40	.36 × .34
				MAY 03	9111.378	54–55	.41 × .32

TABLE 3.1: Journal of Observations

Some of the observations took place when the source was at very low elevation. These data are problematic since the projection of the baselines of the array and the resulting large synthesized beam makes deconvolution difficult, and because the atmospheric contribution to phase errors and flux calibration errors is much larger.

3.3 Data Reduction

The data were reduced using the National Radio Astronomy Observatory's Astronomical Image Processing System (AIPS). After the initial excision of raw data that were clearly corrupted by interference or hardware problems, all datasets were processed by AIPS with a "run file" (see Appendix A) that applied the same processing to each observation. Complex antenna gains were determined by observations of the compact source 0420–014. Refined estimates of the antenna phases were obtained by self-calibration (see section 2.5.1). Observations of 3C 48 were used to set the flux density scale but in order to use as many of the available baselines as possible, we used a model of 3C 48 based on four minutes of A-array observation kindly provided by C. Katz.

We used the CLEAN (Högbom 1974) algorithm implemented within the AIPS task MX (Clark 1980; Schwab 1984) to deconvolve each image. CLEAN is an iterative procedure that, for each iteration, selects the brightest pixel in the map and subtracts a fraction of it multiplied by the dirty beam. As a result, when two point sources are very close together, components tend to fall spuriously between them. This effect becomes particularly troublesome for the B-array data in which the A1–A2 doublet is barely resolved. Our initial attempts to clean these data resulted in a single bright source located between the two images with flux extending from the center towards the true image positions. When we instead used the knowledge of the relative positions of the components as measured from our A-array maps to constrain CLEAN so that it only attempted to place clean components in $0.12''$ square boxes centered on each component, we found that the quality of the deconvolution improved as evidenced by comparison of the B-array maps to the A-array maps.

When two point sources are barely resolved it is difficult to measure their flux densities independently. We attempted to use the AIPS task JMFIT to fit two gaussians to the A1–A2 double and found a strong covariance between the measured flux densities. Since we have already fit for the flux densities of each component in the image deconvolution step, we instead measure the flux density of each image by summing the flux density of the CLEAN components in the box centered at the image position. This CLEAN flux density does not reliably measure the total flux density when the clean components do not reliably represent the total flux distribution (e.g. for extended sources). Since all four images in MG0414 are nearly point-like, the CLEAN components contain essentially all of the flux and can be used directly to get the flux densities. In order to compare the CLEAN flux density to the results of JMFIT, we created artificial datasets with the same uv-sampling as typical data and four gaussian components with parameters measured from our A-array images. Gaussian white noise was added to all visibilities so that the noise in the image was comparable to the noise measured in the real images. The artificial datasets were deconvolved in exactly the same way as the real data and the resulting images then measured by both techniques. The results are comparable for the case when all images are well resolved (A-array) but in the B-array data, the A1–A2 pair is marginally resolved and the CLEAN flux densities had a variance smaller than those of JMFIT by a factor of ~50. This demonstrates that the method of summing CLEAN components can outperform JMFIT for measuring flux densities in the case of marginally resolved point-like images. The reliability of the technqiue in the face of changing uv-sampling and using noise estimates from the real data will be explored in section 4.2.

The variability of the column density of water in the atmosphere makes flux calibration difficult at 15 GHz because of the proximity to the water absorption line at 22 GHz. For example, we have measured variations of atmospheric opacity of a factor of ~1.5 over a period of 25 minutes at the beginning of a snow storm. (The data from that particular observation are omitted from our analysis.) Another source of flux calibration errors are pointing errors in the individual elements that make up the array. The primary beam for the VLA telescopes at 15 GHz is only ~3′ so pointing errors of this magnitude (which might be induced by strong winds) create serious amplitude errors. At low elevations, the atmospheric phase stability is poor and changes on timescales that are too short to self-calibrate with a source as bright as MG0414. This leads to an additional source of sysematic error since uncalibrated phase errors tend to disperse the measured flux density on the sky.

Since flux calibration errors can substantially affect the results of time delay analyses, these analyses are carried out using only those observations made when the wind speed was less than 10 m/s, the object was above 30° elevation, there was no precipitation, and the phase stability of the atmosphere allowed reliable calibration of the complex antenna gains. Of the original 63 observations, three were lost to equipment failures at the VLA site, calibrations for two were lost to human error at operations, and one was lost to snow filling the dishes. Of the the remaining 57 observations, we exclude from analysis five for high wind, eight for precipitation, two for short timescale atmospheric phase instabilities, and seven for low elevation, leaving 35 observations. Table 3.2 lists the measured flux densities for all components for each of the 35 observations.

Julian Date	Flux Densities (mJy)				Julian Date	Flux Densities (mJy)			
- 2440000	A1	A2	B	C	- 2440000	A1	A2	B	C
8930.9968	153.8	134.6	59.8	22.6	9021.6846	154.0	137.0	59.0	22.9
8939.7717	163.7	146.0	66.1	22.9	9024.6766	151.4	134.6	58.4	22.1
8940.8936	153.2	135.8	59.2	22.6	9030.5334	156.7	139.1	59.0	22.4
8944.7380	161.7	142.2	63.7	23.1	9032.6650	151.8	136.5	57.7	22.6
8951.8637	148.4	131.3	58.3	21.7	9036.7067	155.1	137.1	58.8	22.6
8952.6917	158.0	139.7	60.5	23.4	9045.6612	157.7	138.8	59.6	23.1
8955.7073	160.8	140.8	62.7	23.3	9052.4733	154.1	133.8	58.9	20.9
8956.8501	152.7	136.6	60.0	22.9	9070.5746	159.6	140.0	59.6	23.4
8959.7535	147.6	130.5	58.2	21.4	9077.5345	162.4	145.0	61.0	23.7
8971.8451	150.8	132.7	58.3	22.5	9078.5392	160.3	143.0	61.3	22.9
8983.6726	150.8	133.9	59.4	22.0	9081.3337	149.4	129.9	55.1	21.4
8991.6712	149.6	133.0	57.3	22.3	9083.4761	144.5	127.0	54.2	20.7
8993.6338	163.8	145.5	62.8	24.4	9093.4906	152.1	132.8	56.9	21.5
8994.6986	148.8	131.7	57.7	22.2	9098.4980	152.5	133.3	56.8	21.9
9008.7038	148.1	132.9	57.0	21.1	9100.4928	158.8	139.4	59.2	23.5
9011.6065	146.9	130.4	58.8	22.0	9105.3149	155.1	139.2	60.5	22.7
9017.6137	151.5	133.8	57.6	22.0	9107.2857	156.1	137.2	59.7	22.8
					9111.3782	149.2	131.7	56.8	22.1

TABLE 3.2: Measured 15 GHz flux densities (in mJy) for the four components of MG0414. Observations before JD 2449008 were made with the A-array and those after JD 2449035 were made with the B-array. Observations between JD 2449008 and JD2449035 were performed while telescopes where being moved from A to the B configuration.

Figure 3.1 displays the measured light curves for all four images in MG0414. The light curves are clearly dominated by the flux calibration errors caused by variable atmospheric water content, low elevation observing, flux calibrator modelling errors, and poor weather conditions. Even with these effects, the RMS variation of the resulting light curves (without any adjustment for possible source variability) is only 3.3–3.9%. Since this includes both source variability and flux calibration errors, the relative flux calibration is at least this good over the whole dataset.

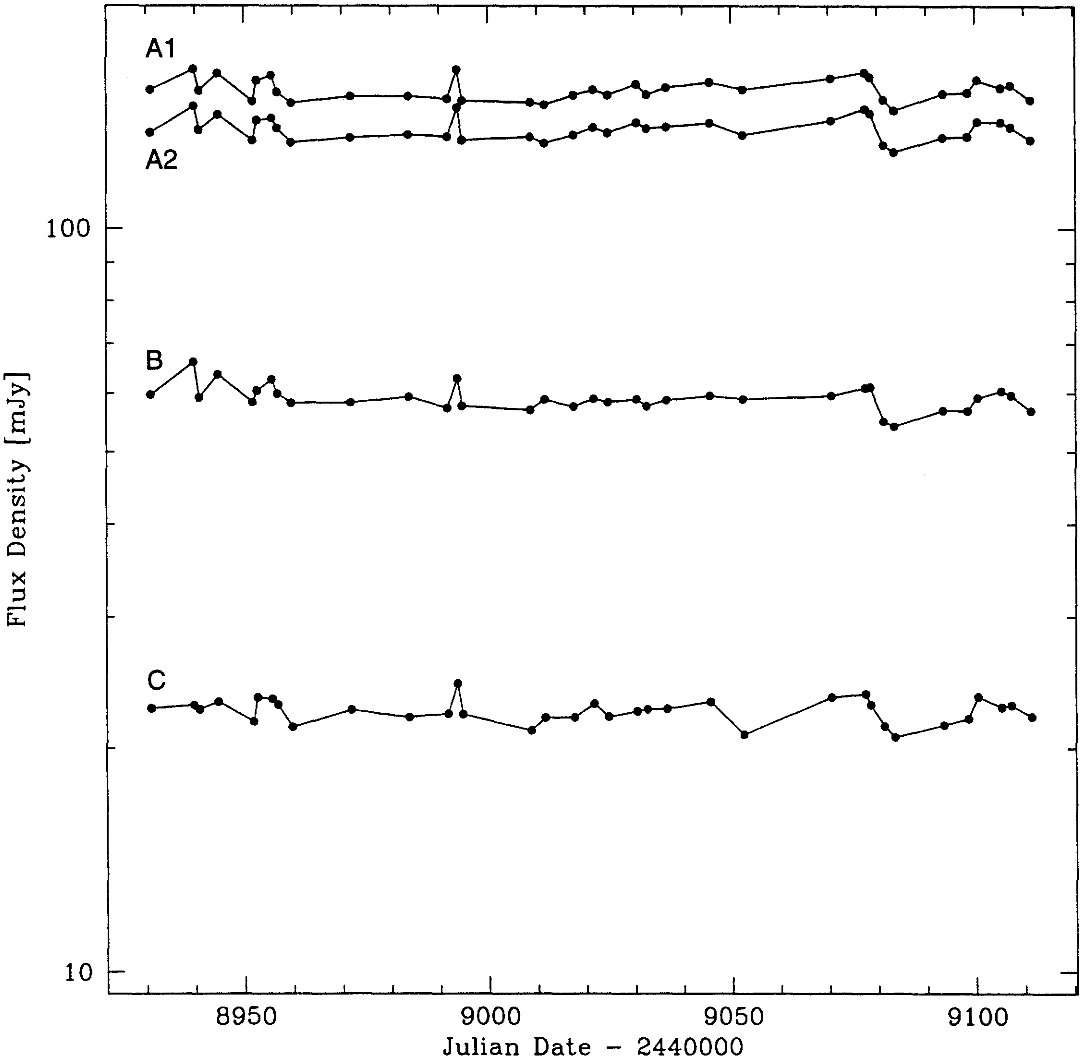

FIGURE 3.1: 15 GHz Light curves for all components shown on a log scale so that shifting on the vertical axis is equivalent to scaling.

Chapter 4

Analysis of the 15 GHz Data

4.1 Variability in the Source

Intrinsic source variability is a prerequisite for the determination of a time delay but the uncertainties in the flux calibration obscure any evidence for source variability in the light curves of Figure 3.1. In order to distinguish instrumental and deconvolution effects from intrinsic variability, we created a "null test" artificial data set.

4.2 Creation of the "null test" data

The "null test" data assume a static model of MG0414. The component shapes (which are nearly point like) were derived from a high-quality A-array observation made during this work and the component flux densities were set at the average flux densities over the whole dataset (see Table 4.1).

Image	Flux Density (mJy)
A1	154.02
A2	136.21
B	59.15
C	22.45

TABLE 4.1: Simulated image flux densities for the 15 GHz "null test" data.

The RMS noise (per visibility) for each observation was estimated from the RMS in the visibility amplitude of the phase calibrator. Since the phase calibrator is known to be point-like to the VLA (Perley 1990), we know that the measured visibilities should have constant amplitude and phase. Many sources of noise including, for example, receiver noise, ground spillover, and atmospheric absorption affect both the real and imaginary parts of the visibility equally. Changing atmospheric phase delays contaminate the visibility phases but not the visibility amplitudes. In the strong signal case, it can be shown that the visibility amplitude is gaussian distributed with a variance that is the same as the variance per visibility due to noise (Thompson *et al.* 1994). The measured RMS noise per ten-second integration is displayed in table 4.2.

Date	Noise (Jy)	Date	Noise (Jy)
1992 NOV 04	0.0754	FEB 03	0.0700
NOV 13	0.0857	FEB 06	0.0669
NOV 14	0.0759	FEB 12	0.0810
NOV 18	0.0829	FEB 14	0.0649
NOV 25	0.0766	FEB 18	0.0697
NOV 26	0.0787	FEB 27	0.0676
NOV 29	0.0851	MAR 05	0.0861
NOV 30	0.0783	MAR 24	0.0672
DEC 03	0.0729	MAR 31	0.0817
DEC 15	0.0735	APR 01	0.0697
DEC 27	0.0743	APR 03	0.1380
1993 JAN 04	0.0829	APR 05	0.0913
JAN 06	0.0781	APR 15	0.0692
JAN 07	0.0940	APR 20	0.0798
JAN 21	0.0715	APR 22	0.0870
JAN 24	0.0677	APR 27	0.0795
JAN 30	0.0725	APR 29	0.0927
		MAY03	0.0649

TABLE 4.2: The measured RMS noise per visibility (10 sec averaging) for each 15 GHz observation. It should be noted that the expected noise per visibility (based on the nominal system temperature (at zenith) and correlator efficiency) is 0.052 Jy (Crane & Napier 1989).

Each observation in the "null test" data was generated by simulating an observation of the model of MG0414 described above using the same uv-sampling as the real data (created with the AIPS task UVMOD). Gaussian noise with RMS amplitude equal to the estimate derived from the phase calibrator was then added to the real and imaginary parts of the visibilities using custom software. Each day was treated separately and the entire process was repeated five times to yield five independent simulations of the entire monitoring program.

These artifical data were then processed in the same way as the actual data to yield five different synthetic time series for which deconvolution and noise effects (but not flux calibration errors) are the same as in the real data. The results of process are displayed in figures 4.1–4.4. There are changing biases in the deconvolution process that are particularly evident in images A1 and B which appear to be anticorrelated in the latter half of the dataset. Unfortunately, the variance in the simulations is nearly the same order as the bias so attempting to correct for these biases is both difficult and not likely to be profitable. Figure 4.5 displays the RMS in a non-signal region in maps made from the real 15 GHz data compared to the RMS noise in maps made from the simulated data. We take the fact that the noise in maps of both real and simulated data are simmilar to indicate that the simulated data have captured the dominant sources of noise.

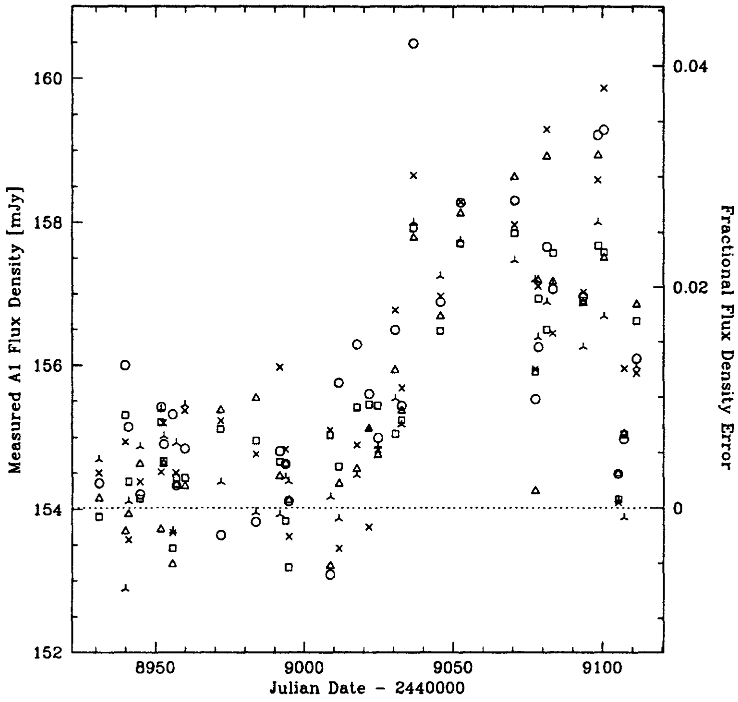

FIGURE 4.1: Results of the reduction of the "null test" data for image A1. Each of the five datasets is represented by a different plot symbol. They are are identical in all respects except that each represents a different instantiation of the noise

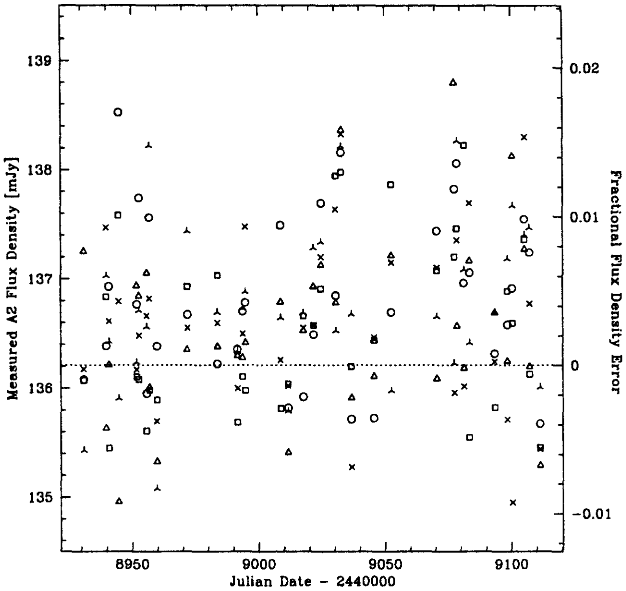

FIGURE 4.2: Results of the reduction of the "null test" data for image A2. Each of the five datasets is represented by a different plot symbol.

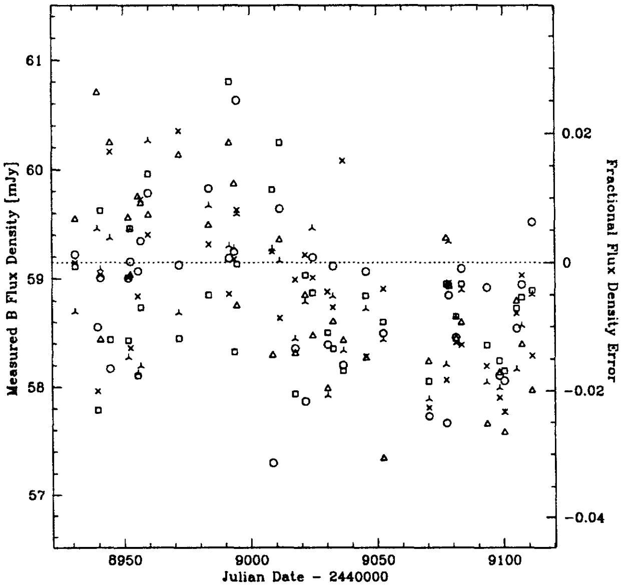

FIGURE 4.3: Results of the reduction of the "null test" data for image B. Each of the five datasets is represented by a different plot symbol.

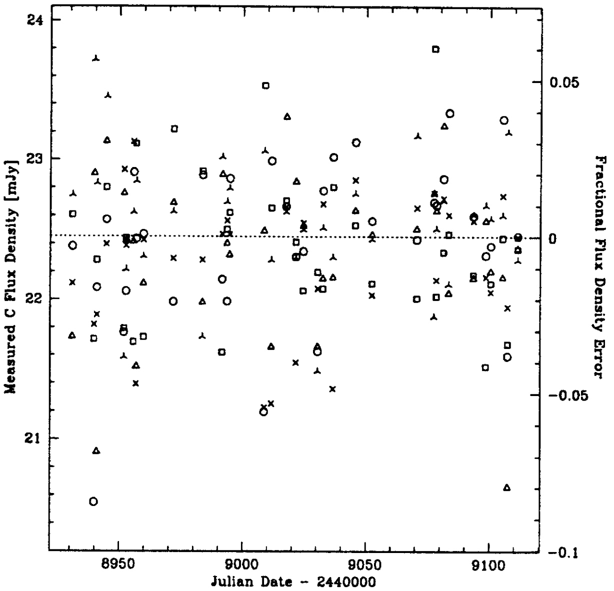

FIGURE 4.4: Results of the reduction of the "null test" data for image C. Each of the five datasets is represented by a different plot symbol.

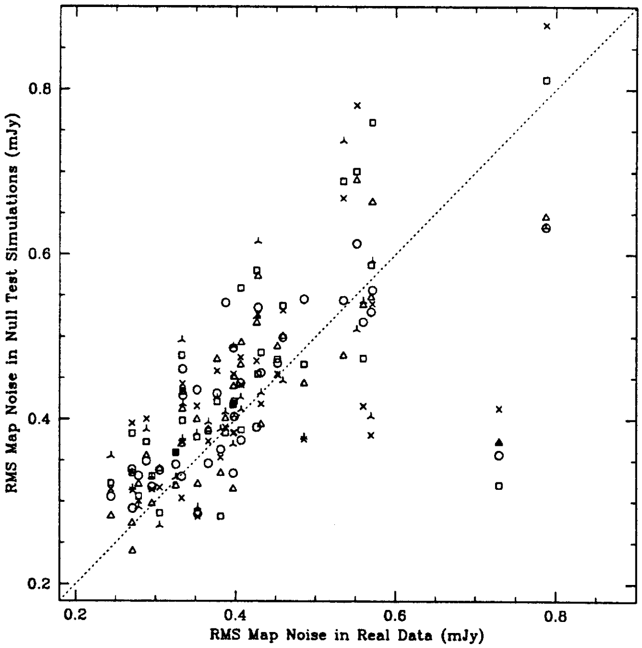

FIGURE 4.5: Comparison of the RMS map noise for "null test" and real data. Each of the five datasets is represented by a different plot symbol.

4.3 Variability in the Flux Density Ratios

In order to examine the posibility of source variability without the confusion of flux calibration errors, we compare the variations in the ratios of various images. Figure 4.6 displays "ratio light curves" in which the flux density of each component is normalized to that of component B.

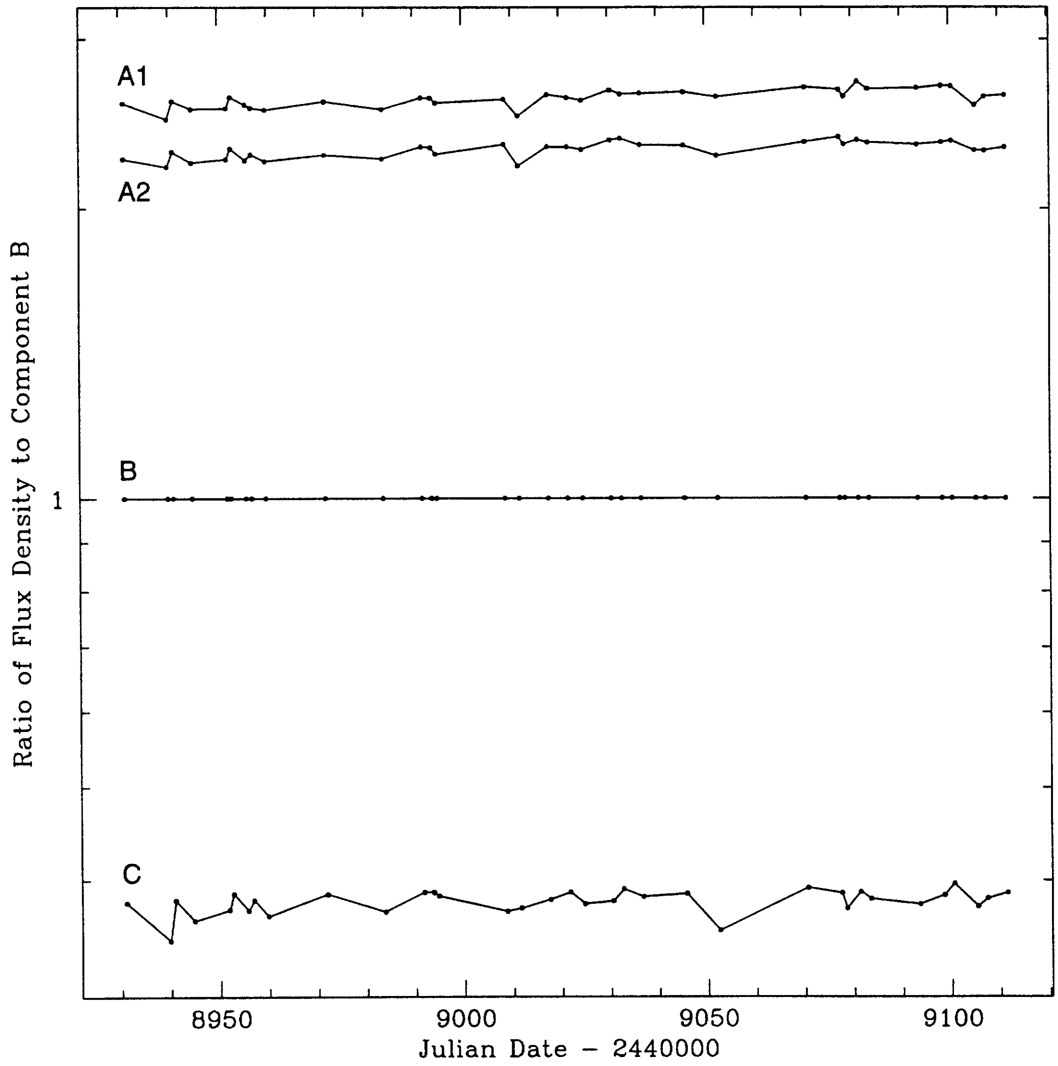

FIGURE 4.6: Time history of the ratio of the flux density of each image to image B. Shown on a log scale so that shifting on the vertical axis is equivalent to scaling.

Table 4.3 displays the RMS variability in each flux ratio for both the real data and the artificial data described above (all five "null tests" taken together). These results demonstrate that uncertainties in the map computation and flux estimation procedures are comparable to the uncertainties in the calibration of the overall flux density scale. Thus, there is no evidence here that any source variability has been detected.

Ratio	Real Data	Artificial Data
A1:A2	0.9%	1.2%
A1:B	2.1%	1.9%
A2:B	1.9%	1.4%
A1:C	2.2%	2.6%
A2:C	2.1%	2.5%
B:C	2.9%	2.6%

TABLE 4.3: Measured RMS variability in image flux density ratios for the data reported here and a set of five "null test" artificial datasets with similar instrumental properties.

4.4 Structure Function Analysis

Another measure of variability is the first order structure function (Simonetti *et al.* 1985),

$$V(\tau) = \frac{1}{2}\left\langle [s(t) - s(t+\tau)]^2 \right\rangle \tag{4.1}$$

where $s(t)$ is the image flux density at time t, τ is the difference in time between two observations, and $\langle\,\rangle$ indicates the average.) The structure function can be estimated from data with arbitrary sampling by simply calculating a single point estimate of the structure function from each pair of data points and binning in lag space (Press *et al.* 1992c). We fit the structure function of the log of the radio data in decibels (referenced to 1 Jy), adopting a structure function of the form

$$V(\tau) = C\tau^{1.0} \tag{4.2}$$

because a power-law of unit index has been found to be a good fit to the structure function of other sources at small lags (Hughes *et al.* 1992). At lags larger than about one year, the structure function typically turns over and then remains constant for larger lags. We expect that the structure function of instrumental errors will be that of white noise (i.e. a constant independent of lag), so we take the power law part of the structure function as an estimate of the maximum possible variability in the source and find

$$V(\tau) = (0.000139\frac{\mathrm{dB}^2}{\mathrm{day}})\tau.$$

The fit to the (binned) measurements of the structure function is displayed in Figure 4.7. The quality of the fit is poor and it is likely that the structure function estimates for large lags are larger than they should be since the end of the lightcurve (and thus many of the large lags) is affected by poor observing conditions. The fit structure function should therefore be taken as an upper limit on the variability. The expected RMS flux density on the timescales of interest (~20 days) is at most

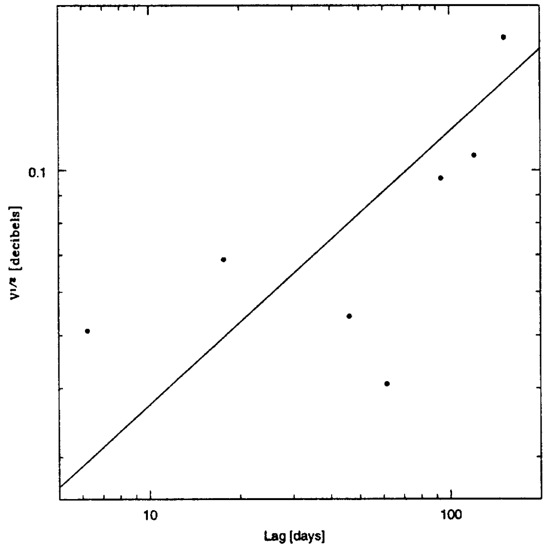

FIGURE 4.7: Structure function fit to temporally binned structure function estimates from the 15 GHz data.

$$2V(\tau = 20) = 0.00556\,\mathrm{dB}^2 = 0.074565\,\mathrm{dB} = 1.7\%. \tag{4.3}$$

The structure function analysis finds a zero lag correlated noise of about 3.4% which we assign to flux density scale calibration error. The fit implies that the signal-to-noise ratio for a single measurement of the change in flux density on time scales of interest is at most

$\frac{1.7}{3.4} = 0.5$.

4.5 Time Delays and Correlated Variability

The data presented above provide no evidence that we have detected variability in MG0414. However, it is possible that some of the variability in the data is due to the quasar and that such "real" variability would manifest itself as itself in the form of a correlation between flux density measurements separated by the lens time delay. To investigate this, we computed discrete correlation functions (Edelson & Krolik 1988) for pairs of our light curves. No evidence for correlations was found in this analysis.

A time delay detection technique with greater statistical efficiency than cross-correlation techniques has been developed by Press, Rybicki, and Hewitt (1992b; 1992c); see also (Rybicki & Press 1992). Here we examine their χ^2 statistic (hereafter PRH–χ^2). To apply their method, one assumes (or better, fits for) a flux ratio between two images and then for each trial delay, creates a combined light curve that consists of the union of the two light curves with one of the shifted and scaled relative to the other. For each trial delay, we ask how likely (in a χ^2 sense) the combined light curve is to have originated from a process whose variability is described by the assumed structure function. We have performed Monte Carlo simulations by generating 500 trials using the temporal sampling of the data from this work, the delays predicted by the Hewitt, *et al.* (1992) models, the noise measured from the data (assumed to be white gaussian), and assuming the source variability to be generated by a gaussian process with the same structure function as that estimated from the data. For comparison, we also performed the same Monte Carlo simulation assuming no gravitational lens (i.e. every image is an independent source of gaussian noise again with the same structure function as that estimated from the data but uncorrelated with the other images). Figure 4.8 displays a histogram of the lag at the absolute minimum of the PRH–χ^2 curve on the interval [-45,45] for every image pair in the presence of the modelled gravitational lens. For comparison, Figure 4.9 displays the same histograms for the simulation without a gravitational lens. The simulations show that given the quality and quantity of the available data and the small (if present) variability of the source, extraction of a time delay is not possible by this technique. Only 22–31% of the measurements are within ±5 d of the simulated delay. However, it is clear that the technique is capable of

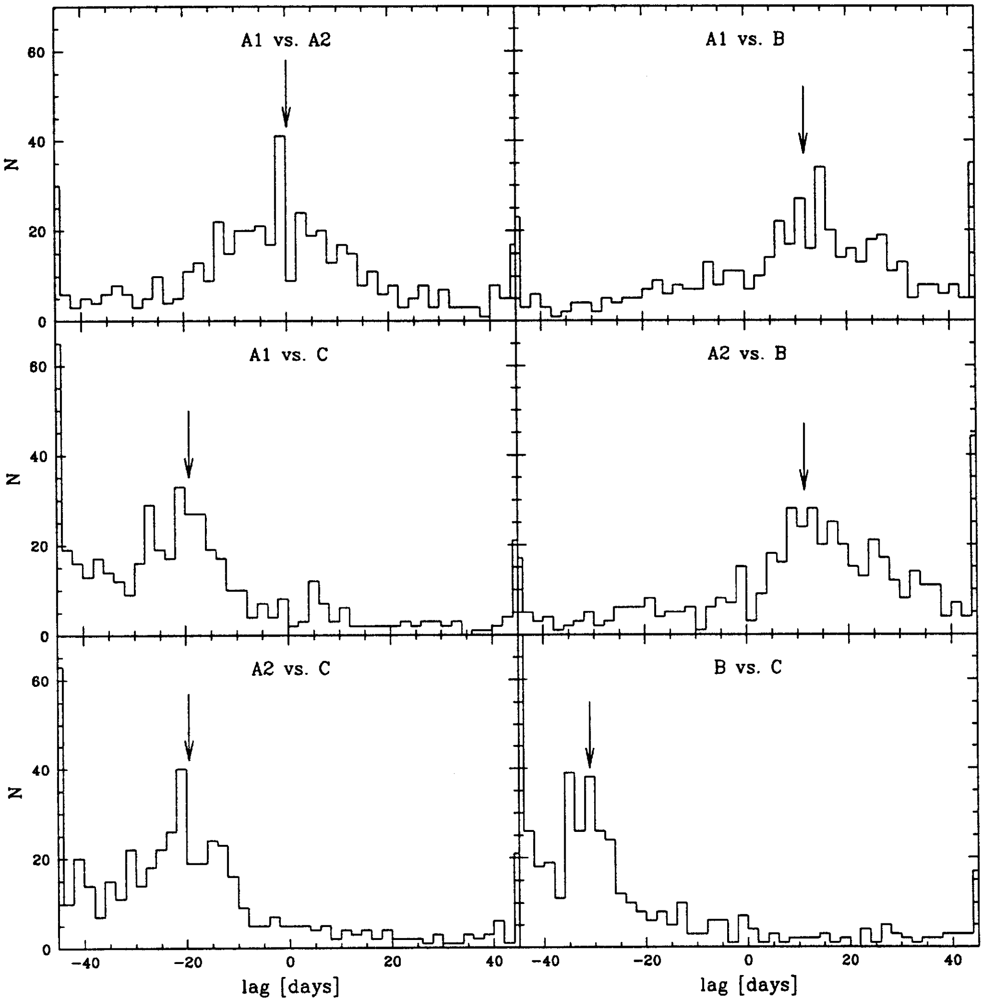

FIGURE 4.8: Histograms of the absolute minimum of the PRH-χ^2 on the interval [-45,45] for 500 Monte Carlo trials assuming the presence of a gravitational lens. The model delay is marked with an arrow in each case. The bin on the left edge of the B vs. C plot is off-scale, its true value is 121.

detecting the presence of correlated variability since the correlated simulations show 3–6 times more measurements within 5 d of the simulated delay than the uncorrelated (no gravitational lens) simulations.

Even given the low signal to noise ratio of the present data, the PRH-χ^2 method is interesting since it uses all available lag pairs and is thus a very sensitive way to measure correlated variability. Given large datasets, one can expect to detect correlated variability

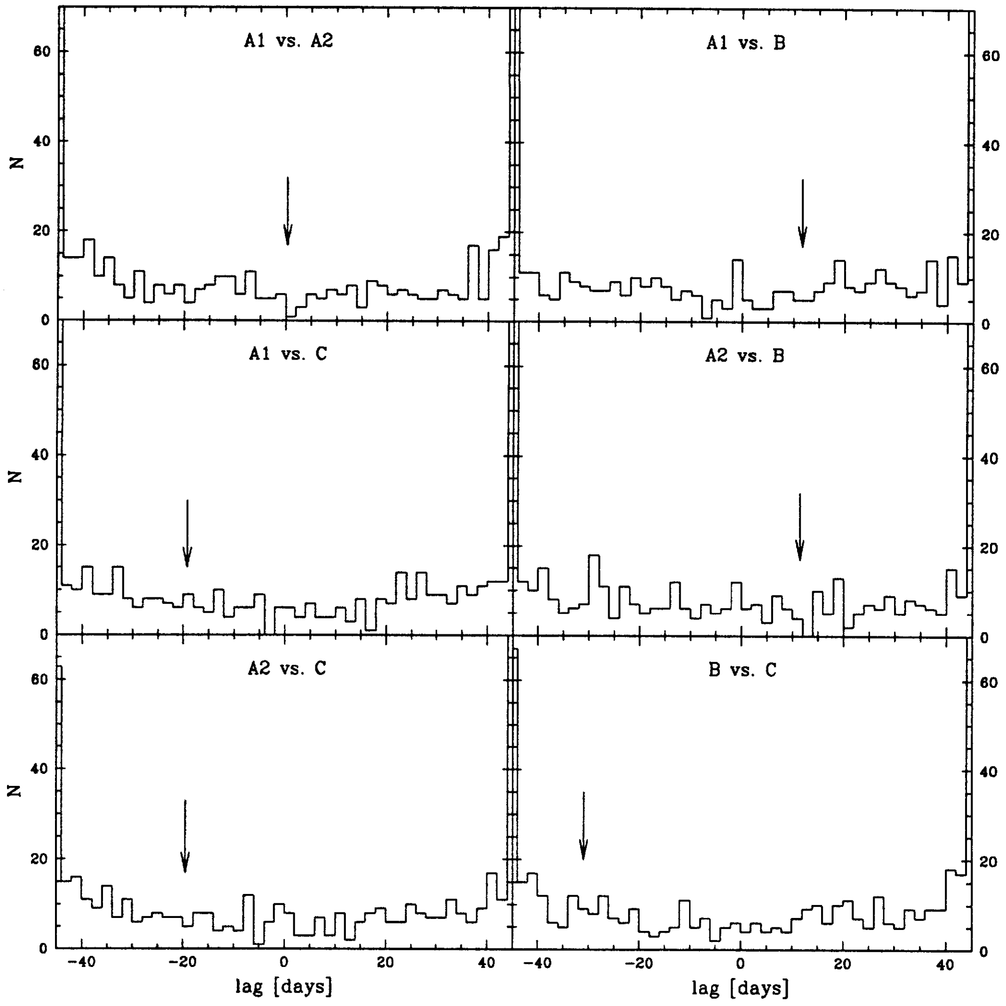

FIGURE 4.9: Histograms of the absolute minimum of the PRH-χ^2 on the interval [-45,45] for 500 Monte Carlo trials assuming no gravitational lens. For convenience the model delay from the lensing assumed in Figure 4.8 is marked with an arrow in each case. Note that many of the minima fall in the edge bins which are off scale in most cases.

even when the signal to noise ratio is less than unity (Hewitt *et al.* 1995).

From the measured MG0414 data, one can compute a distinct PRH-χ^2 curve for every pair of images using the average flux ratio as an estimate of the true flux ratio. The six curves computed from the present data are displayed in Figure 4.10. It is clear from examining the PRH-χ^2 curves that there is a strong correlation between the light curves at zero lag due to unmodelled errors in the absolute flux calibration and that none of them

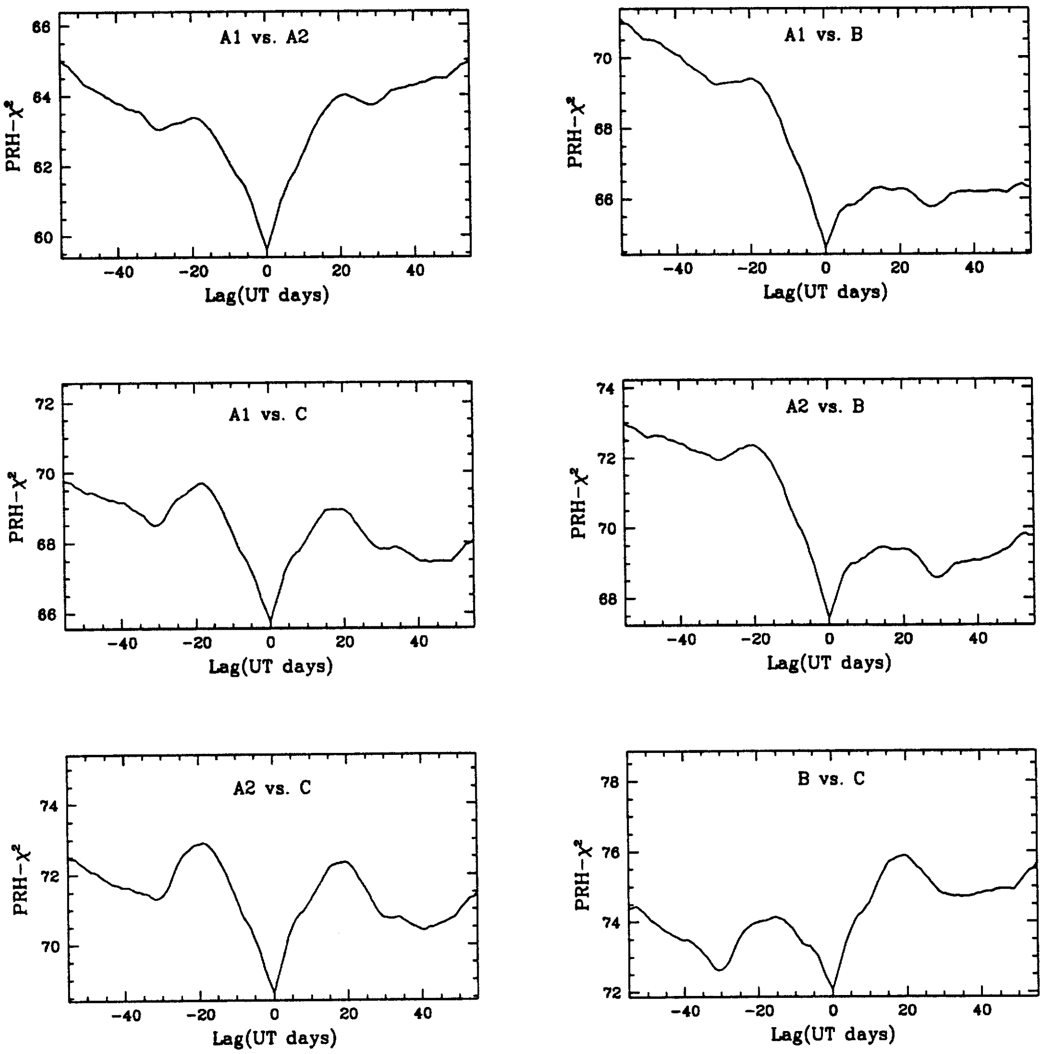

FIGURE 4.10: PRH-χ^2 curves for all pairs of components (69 degrees of freedom). Note the prominent feature at zero lag due to flux calibration errors. Also note that some of the curves, particularly those in the right column exhibit a strong preference for a particular *sign* of the delay. For ease of comparison, the curves are all plotted with the same vertical scale.

presents a convincing argument for any particular time delay. This is not surprising. The signal-to-noise ratio of 0.5 for the variability as measured in a single lag pair (see Section 4.1 above) can be compared to the case of MG1131+0456 for which the same ratio is 0.7. Simulations of time delay observations in MG1131 show that 50 to 100 flux measurements are required for a measurement of the time delay (Hewitt *et al.* 1995). Clearly this study of

MG0414 suffers because there are too few measured points, given the small signal-to-noise ratio.

For comparison, we have computed the PRH-χ^2 curves for the "null test" simulated

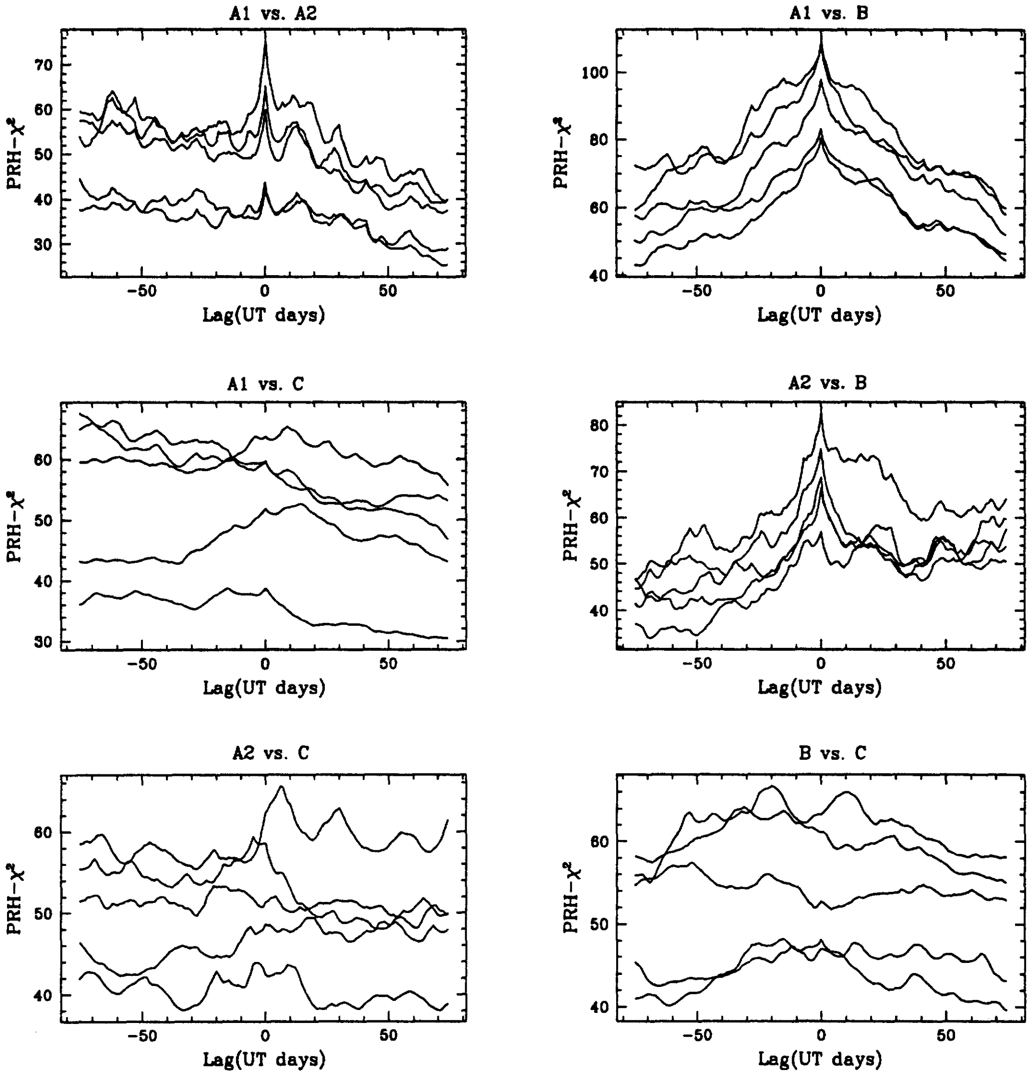

FIGURE 4.11: PRH-χ^2 curves for all pairs of components (69 degrees of freedom) calculated from the five "null test" simulated datasets. Note the difference in scale between this and Figure 4.10

datasets using in the analysis same structure function as that used for the real data and the setting the noise equal to the RMS over all of the "null test" data for each image. The five PRH-χ^2 curves for each pair of images are displayed in Figure 4.11. It is interesting to note that in the cases where the PRH-χ^2 curves of the real data (Figure 4.10) show a particular preference for the *sign* of the delay, it is consistent with the predictions of Kochanek's models 2, 3, and 4 (Kochanek 1991) and the Hewitt *et al.* (1992) model. Unfortunately, the magnitude and variety of the structures in the PRH–χ^2 curves of the synthetic data make it very unlikely that the structure in the real PRH–χ^2 curves is significant.

4.6 Conclusions

The 15 GHz data is dominated by flux density calibration errors of order 3.4% which appear to dominate any intrinsic variability which on the timescales of interest (~20 days) is at most 1.7%. Measurement of a time delay from these data is difficult at best because the variability is very small, the small size of the dataset gives few lag pairs, and the zero lag correlation caused by errors in flux calibration dominates the signal. One could, in principle, modify the statistical model of the data assumed in the PRH–χ^2 analysis to account for the flux density calibration errors but it us unlikely that such work will yield a time delay using these data. These 15 GHz data do not provide a convincing case for source variability nor for any particular value of a time delay in MG0414.

Another approach to extraction of a time delay from these data would be to develop a time delay estimator that depends only on the flux density ratios and tolerates the imperfect sampling characteristic of the data. If such a technique were developed, one could use more of the present data since the flux density ratios are independent of the flux calibration.

Chapter 5

Observations of MG0414+0534 at 8 GHz

5.1 Introduction

New monitoring observations of MG0414 at 8 GHz were planned with the intention of improving on the flux calibration, duration, and number of samples relative to the 15 GHz dataset. In order to reduce the sensitivity to atmospheric absorption, wind-induced pointing errors, and receiver noise, we moved the observing frequency to 8 GHz (X-band). The change in frequency moves further away from the water absorption line at 22 GHz, increases the size of the primary beam by a factor of two, and lowers the system noise temperature from 116 K to 30 K all while the flux density of the source increases by a factor of ~1.5.

These advantages come at the expense of resolution and expectation for variability. The change in resolution makes the A1 and A2 flux densities difficult to measure independently but the 15 GHz data suggest that the delay between A1 and A2 may be short (since A1 and A2 track each other very well in those data). One also expects the A1–A2 time delay to be short on the basis of lens modelling. The change in resolution also makes the problem of flux density calibration easier since the calibrator is less resolved. However, one would expect a compact radio source to be more variable at higher frequencies so the change in freqency may reduce the observed variability.

In order to get a large temporal baseline on which to do time delay analysis, the program was planned to go from the beginning of A-array all the way to the end of C-array thus obtaining the maximal temporal baseline (~300 days) available given the VLA's reconfiguration schedule.

5.2 Observations

We observed MG0414 with the VLA starting on 1994 March 1 in the A-array, continuing through the B and C-arrays, and ending on 1995 Jan 1. The central frequencies for the two observing bands were the the standard VLA X-band values of 8.4149 and 8.4649 GHz each with a bandwidth of 50 MHz. Each band was observed in both right-circular and left-circular polarization so the total observed bandwith came to 100 MHz for each polarization. There were a total of 82 observations each of duration 0.5 to 1.0 hours spanning a total of 306 days (see Table 5.1). The observations for this program were scheduled into small interstices in the VLA schedule but rarely at times when the source was at very low elevation. During each observation we planned to observe the flux density calibrator twice, once at the beginning and once at the end of the scheduled observing time. This insured that calibration data would be obtained for every observation even during adverse observing conditions and allowed comparison of the two separate calibrations determined from the two independent visits to the flux calibrator.

5.3 Data Reduction

The data were processed using the National Radio Astronomy Observatory's Astronomical Image Processing System (AIPS) in much the same was as described for the 15 GHz data (see section 3.3). Notable differences include the substitution of a new compact phase calibration source (0421+019) because the previous phase calibrator (0420-014) is classified as an optically violent variable source and might have short timescale variability. Most of the changes in the "run file" were made in order to accomodate a change in the underlying AIPS software (see Appendix B). Flux calibration was accomplished by comparison to a model of 3C 48 obtained from a carefully calibrated full synthesis observation and kindly provided by R.C. Walker and D.S. Briggs. The CLEAN deconcolution algorithm was again constrained to place clean components only in small boxes near the positions of the images but the boxes were enlarged to $0.18''$ square.

It should be noted that the technique of using small CLEAN boxes at the known positions of the images continues to work even though the source (particularly in C-array) is very poorly resolved. Figures 5.1 and 5.2 display A, B, and C-array maps made during the course of this work.

	Julian Date	Synthesized Beam			Julian Date	Synthesized Beam	
IAT Date	−244000	Size (″)	PA	Date	−244000	Size (″)	PA
1994 MAR 01	9412.560	0.23 × 0.20	5.7	AUG 08	9573.141	0.72 × 0.57	13.2
MAR 06	9418.481	0.25 × 0.21	-15.0	AUG 11	9576.029	0.74 × 0.58	-20.3
MAR 09	9420.517	0.23 × 0.21	0.9	AUG 14	9579.085	0.71 × 0.59	-5.3
MAR 13	9425.317	0.57 × 0.21	-51.9	AUG 17	9581.992	0.78 × 0.58	-30.4
MAR 17	9429.325	0.36 × 0.21	-50.5	AUG 20	9584.964	0.82 × 0.58	-36.2
MAR 19	9431.540	0.22 × 0.20	-4.8	AUG 22	9587.052	0.67 × 0.56	-6.9
MAR 20	9432.300	No data – see text		AUG 25	9590.180	0.93 × 0.60	47.0
MAR 28	9439.592	0.32 × 0.22	52.9	AUG 29	9593.899	1.07 × 0.60	-47.3
MAR 30	9441.524	0.28 × 0.22	12.1	SEP 01	9597.098	0.74 × 0.60	28.4
APR 06	9448.544	0.27 × 0.22	43.0	SEP 03	9599.124	0.77 × 0.59	35.0
APR 07		No data – see text		SEP 05	9600.951	0.70 × 0.68	-10.4
APR 11	9454.342	0.30 × 0.23	-40.9	SEP 08	9604.016	0.73 × 0.63	10.0
APR 19	9462.467	0.26 × 0.22	19.7	SEP 13	9609.002	0.80 × 0.66	12.9
APR 25	9468.386	0.26 × 0.21	-2.6	SEP 15	9610.997	2.44 × 0.88	79.6
APR 28	9471.473	0.24 × 0.21	31.7	SEP 18	9613.947	2.17 × 0.93	-84.6
APR 29	9472.209	0.37 × 0.24	-46.0	SEP 22	9617.874	2.60 × 0.85	-70.4
MAY 02	9475.388	0.22 × 0.20	4.7	SEP 25	9620.991	2.10 × 0.89	76.9
MAY 09	9482.388	0.37 × 0.22	-70.1	SEP 27	9622.985	2.21 × 0.88	77.9
MAY 12	9485.466	0.96 × 0.29	58.9	OCT 01	9626.912	2.24 × 0.89	-83.9
MAY 14	9487.377	0.67 × 0.28	72.1	OCT 05	9630.984	2.22 × 0.88	73.8
MAY 16	9489.362	0.69 × 0.25	76.1	OCT 12	9637.986	2.26 × 0.89	67.4
MAY 18	9491.281	0.70 × 0.28	-80.8	OCT 18	9643.844	2.33 × 1.83	-28.4
MAY 23	9496.329	No data – see text		OCT 22	9647.853	2.39 × 1.81	-19.9
MAY 26	9499.280	0.62 × 0.29	-89.9	OCT 30	9655.995	2.86 × 1.96	45.6
MAY 30	9503.372	0.82 × 0.25	64.4	NOV 03	9659.925	2.36 × 1.81	29.7
JUN 01	9505.381	No data – see text		NOV 07	9663.894	2.37 × 1.81	16.2
JUN 02	9506.284	0.78 × 0.63	-13.7	NOV 10	9666.907	2.37 × 1.82	26.5
JUN 11	9515.301	0.73 × 0.58	8.4	NOV 14	9670.760	2.27 × 1.86	-16.9
JUN 17	9521.304	0.75 × 0.60	22.9	NOV 17	9673.678	No data – see text	
JUN 21	9525.086	1.06 × 0.63	-46.0	NOV 21	9677.813	2.29 × 1.78	3.2
JUN 25	9529.274	0.71 × 0.58	16.9	NOV 24	9680.681	2.85 × 1.84	-46.6
JUN 28	9532.232	0.71 × 0.58	3.6	DEC 01	9687.681	2.59 × 1.94	-31.7
JUL 02	9536.296	0.77 × 0.59	36.6	DEC 04	9690.821	2.37 × 1.80	15.2
JUL 05	9539.172	0.70 × 0.58	-8.9	DEC 07	9693.645	2.83 × 1.84	-47.6
JUL 10	9544.220	0.72 × 0.57	10.7	DEC 11	9697.654	2.59 × 1.93	-31.2
JUL 14	9548.147	0.77 × 0.59	-35.5	DEC 14	9700.584	3.57 × 1.88	-53.8
JUL 19	9553.239	0.80 × 0.59	30.8	DEC 17	9703.636	2.55 × 1.93	-31.1
JUL 23	9557.164	0.71 × 0.58	7.4	DEC 20	9706.713	2.33 × 1.84	-1.6
JUL 28	9562.170	0.72 × 0.57	10.7	DEC 24	9710.723	2.29 × 1.79	2.4
JUL 31	9565.162	0.72 × 0.57	10.9	DEC 28	9714.609	2.47 × 1.95	-33.6
AUG 04	9569.193	0.77 × 0.60	31.9	1995 JAN 01	9718.682	2.33 × 1.85	8.4

TABLE 5.1: Journal of 8 GHz observations.

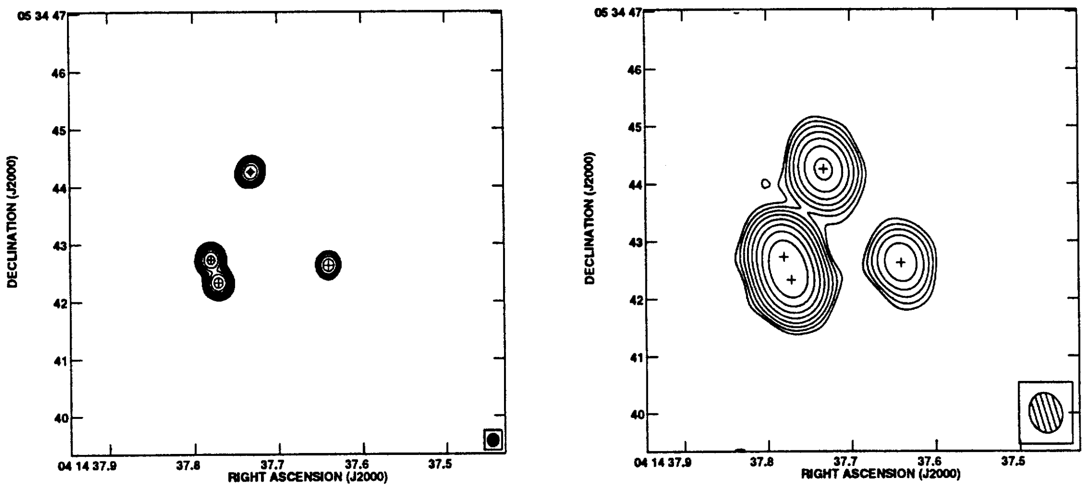

FIGURE 5.1: 8 GHz A-array (left) and B-array (right) maps made during the course of the present work. Observation dates are 1994 Mar 19 and 1994 Jun 25 respectively. The positions of the images are marked and the ellipse in the lower right corner illustrates the size of the synthesized beam for each observation.

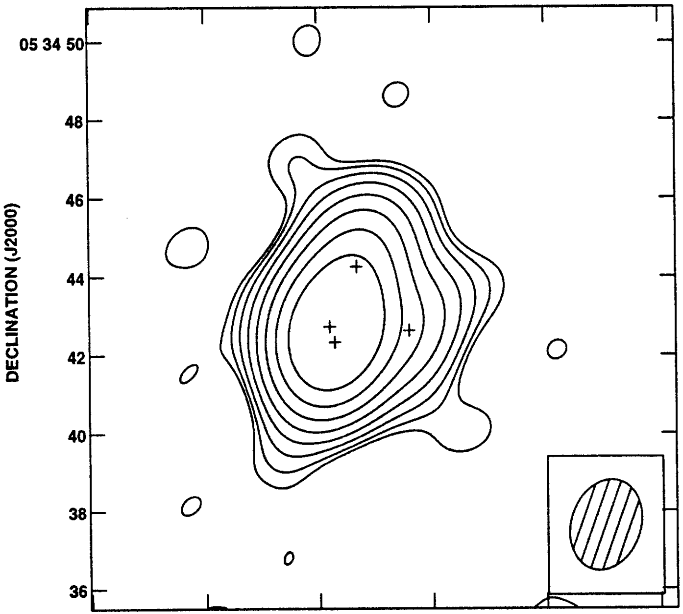

FIGURE 5.2: C-array map of MG0414 (observation date 1994 Oct 22). The positions of the images are marked and the ellipse in the lower right corner illustrates the size of the synthesized beam. Note the change in scale from Figure 5.1

From the original 82 observations, one was lost to equipment failure at the VLA, two were lost to low elevation observing and resulting poor phase stability, and two were excluded from the analysis because the two observations of the flux density calibrator gave inconsistent results. Table 5.2 lists the flux densitites measured by the technique of summing the clean components that appear in each CLEAN box. The A1 and A2 flux densitites are measured separately, but reported together since they are not well resolved in the C-array data.

Julian Date	Flux Density (mJy)			RMS Map Noise
-2440000	Image A	Image B	Image C	(mJy/beam)
9412.560	461.523	93.312	36.246	0.2346
9418.481	461.850	93.824	35.938	0.1273
9420.517	465.062	94.738	35.459	0.1206
9425.317	451.965	92.497	35.431	0.2526
9429.325	442.812	90.017	35.267	0.3699
9431.540	461.001	94.697	36.224	0.0964
9439.592	472.889	96.455	36.799	0.2086
9441.524	469.022	96.170	36.815	0.1785
9448.544	468.794	95.547	36.390	0.1665
9454.342	457.359	93.446	35.253	0.1771
9462.467	468.571	95.117	36.445	0.1333
9468.386	438.550	89.566	33.291	0.2965
9471.473	480.449	98.990	37.294	0.1180
9472.209	453.747	93.262	35.186	0.1815
9475.388	459.999	94.563	36.284	0.1978
9482.388	471.028	97.785	36.594	0.1553
9485.466	475.246	97.768	37.152	0.3022
9487.377	460.841	94.833	35.388	0.2816
9489.362	475.743	96.207	36.958	0.3690
9491.281	462.063	93.479	35.781	0.3159
9499.280	461.849	94.009	36.410	0.2138
9503.372	467.549	95.487	36.175	0.1720
9506.284	447.884	92.909	35.395	0.5039
9515.301	460.405	95.008	35.868	0.2729
9521.304	465.547	96.080	36.130	0.2386
9525.086	465.722	94.919	36.543	0.8151
9529.274	463.593	94.530	36.340	0.1877
9532.232	461.951	93.632	36.261	0.3205
9536.296	463.616	94.618	36.234	0.2490
9539.172	461.054	93.958	35.597	0.3591
9544.220	461.771	94.922	36.602	0.2469
9548.147	462.434	94.128	35.993	0.4708
9553.239	468.437	94.933	36.498	0.2677
9557.164	466.564	94.912	36.584	0.2790
9562.170	470.673	95.358	36.767	0.2663
9565.162	469.862	95.806	36.394	0.2869
9569.193	468.343	95.394	36.128	0.2759
9573.141	464.077	95.034	36.316	0.2752
9576.029	461.529	94.542	35.766	0.4101
9579.085	459.510	93.860	36.459	0.3409
9581.992	461.095	94.824	35.986	0.4073
9584.964	462.609	94.972	36.015	0.3826
9587.052	461.409	94.631	36.345	0.3323
9590.180	470.177	95.382	36.891	0.3851

continued on next page.

Julian Date	Flux Density (mJy)			RMS Map Noise
-2440000	Image A	Image B	Image C	(mJy/beam)
9593.899	454.799	92.408	35.802	0.7415
9597.098	464.380	94.370	36.975	0.2804
9599.124	473.818	94.984	36.649	0.2343
9600.951	459.580	94.035	35.950	0.3705
9604.016	463.632	94.573	35.471	0.5158
9609.002	467.993	94.597	36.605	0.4639
9610.997	466.691	94.724	38.003	0.4971
9613.947	464.437	94.004	36.046	0.4663
9617.874	463.509	94.719	36.492	0.5518
9620.991	465.853	94.736	36.601	0.5643
9622.985	465.688	94.253	36.609	0.5134
9626.912	464.598	94.293	35.512	0.4791
9630.984	464.428	94.364	36.397	0.5535
9637.986	466.416	95.590	36.076	0.7065
9643.844	461.724	92.570	35.660	0.5141
9647.853	463.925	93.583	36.188	0.3750
9655.995	471.528	93.928	36.407	0.4139
9659.925	468.903	96.038	36.463	0.5374
9663.894	464.267	94.541	36.995	0.4534
9666.907	464.837	96.617	36.528	0.5052
9670.760	463.967	93.385	36.565	0.7377
9677.813	464.300	95.046	36.640	0.3545
9680.681	460.877	93.978	36.397	0.6378
9687.681	466.697	94.453	36.481	0.6108
9690.821	465.438	94.397	36.667	0.4458
9693.645	461.442	93.487	35.810	0.6471
9697.654	465.998	94.853	35.662	0.5844
9700.584	456.258	92.956	35.574	0.4945
9703.636	467.393	93.229	35.612	0.6221
9706.713	464.618	94.525	35.807	0.6581
9710.723	466.013	94.472	36.532	0.3495
9714.609	466.454	95.023	36.101	0.6129
9718.682	467.458	96.552	35.508	0.3904

Table 5.2: Measured 8 GHz flux densitites uncorrected for deconvolution effects (see section 6.2).

The 8 GHz uncorrected lightcurves for image A1+A2, B, and C are shown in Figure 5.3. As in the 15 GHz data, there are many obvious features that are correlated between components at zero lag and are thus probably due to errors in the calibration of the flux scale. Also striking are the features in the B and C images that appear near the end of B-array and continue through C-array. Note a large decrement in the flux density of the C image that appears coincident with the shift to C-array. Given the nearly unresolved appearance of the source in Figure 5.2, the reader might be particularly suspect of any flux densities measured from C-array data. This suspicion is quite justified and will be addressed with a correction technique discussed in section 6.2.

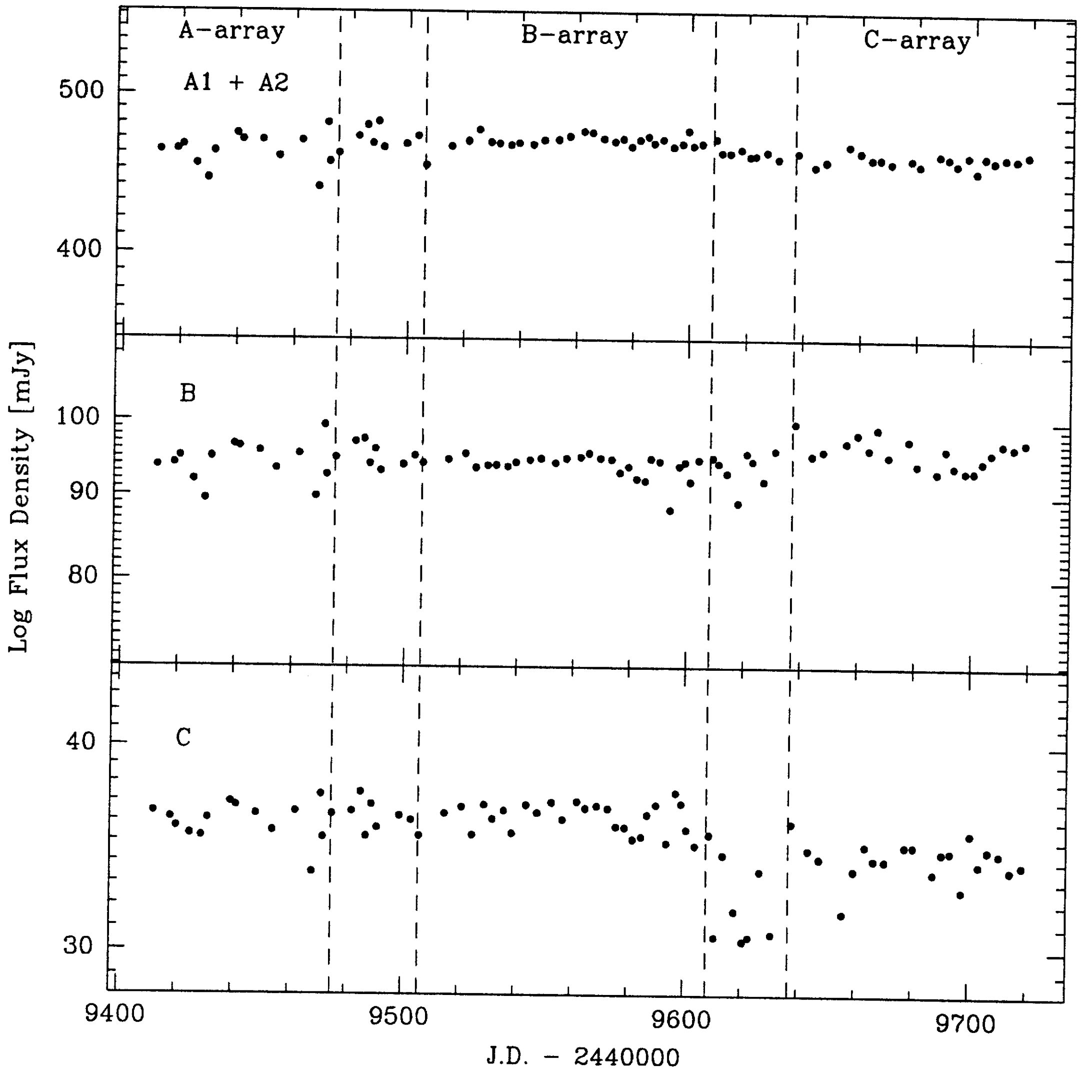

FIGURE 5.3: 8 GHz lightcurves for images A1+A2, B, and C shown on a log scale so that shifting is the same as scaling. These data do not include the deconvolution correction that is developed in section 6.2.

Chapter 6

Analysis of the 8 GHz Data

6.1 Introduction

Proceding as we did with the 15 GHz data, we created a "null test" data set to help understand the effects of noise and deconvolution errors on the measured flux densities. The "null test" data were created exactly as described in section 4.2. The static model of MG0414 used in the generation of the synthetic data was again based on the component shapes measured from the real data (A-array) with the flux densities set to their average values over the whole dataset (see Table 6.1). Gaussian noise was again added to the simulated visibility data with the RMS amplitude of the noise (see Table 6.2) derived from the RMS variability of the visibility amplitudes in observations of an unresolved calibration source.

Image	Flux Density (mJy)
A1	244.623
A2	219.074
B	94.61
C	35.17

TABLE 6.1: Simulated image flux densities for 8 GHz "null test" data

The "null test" data were again processed by the same "run file" that was used to process the real data and the results are displayed in Figures 6.1–6.3. Note that, in contrast with the 15 GHz "null test" data, the variance in the flux densities measured from the five synthetic datasets is quite small in comparison to the error relative to the simulated flux density. This suggests the possiblity of using the "null test" data to *measure*

Date	Noise (Jy)	Date	Noise (Jy)	Date	Noise (Jy)
1994 MAR 01	0.02243	JUN 25	0.01555	SEP 22	0.01454
MAR 06	0.01432	JUN 28	0.01548	SEP 25	0.01579
MAR 09	0.01477	JUL 02	0.01713	SEP 27	0.01494
MAR 13	0.01662	JUL 05	0.01451	OCT 01	0.01462
MAR 17	0.01763	JUL 10	0.01455	OCT 05	0.01575
MAR 19	0.01503	JUL 14	0.01481	OCT 12	0.01530
MAR 28	0.01611	JUL 19	0.01524	OCT 18	0.01487
MAR 30	0.01745	JUL 23	0.01472	OCT 22	0.01464
APR 06	0.01570	JUL 28	0.01539	OCT 30	0.01548
APR 11	0.01581	JUL 31	0.01486	NOV 03	0.02059
APR 19	0.01473	AUG 04	0.01571	NOV 07	0.01472
APR 25	0.01811	AUG 08	0.01496	NOV 10	0.01453
APR 28	0.01626	AUG 11	0.01489	NOV 14	0.01504
APR 29	0.01557	AUG 14	0.01513	NOV 21	0.01453
MAY 02	0.01797	AUG 17	0.01665	NOV 24	0.01562
MAY 09	0.01427	AUG 20	0.01421	DEC 01	0.01440
MAY 12	0.01587	AUG 22	0.01435	DEC 04	0.01482
MAY 14	0.01587	AUG 25	0.01658	DEC 07	0.01514
MAY 16	0.01774	AUG 29	0.01745	DEC 11	0.01433
MAY 18	0.01711	SEP 01	0.02957	DEC 14	0.01554
MAY 26	0.01568	SEP 03	0.01549	DEC 17	0.01498
MAY 30	0.01560	SEP 05	0.02119	DEC 20	0.01451
JUN 02	0.01453	SEP 08	0.02149	DEC 24	0.01513
JUN 11	0.01861	SEP 13	0.02660	DEC 28	0.01495
JUN 17	0.01439	SEP 15	0.01507	1995 JAN 01	0.01440
JUN 21	0.02080	SEP 18	0.01518		

TABLE 6.2: The measured RMS noise per visibility (10 sec averaging) for each 8 GHz observation. It should be noted that the expected noise per visibility (based on the nominal system temperature and correlator efficiency) is 0.011 Jy (Crane & Napier 1989).

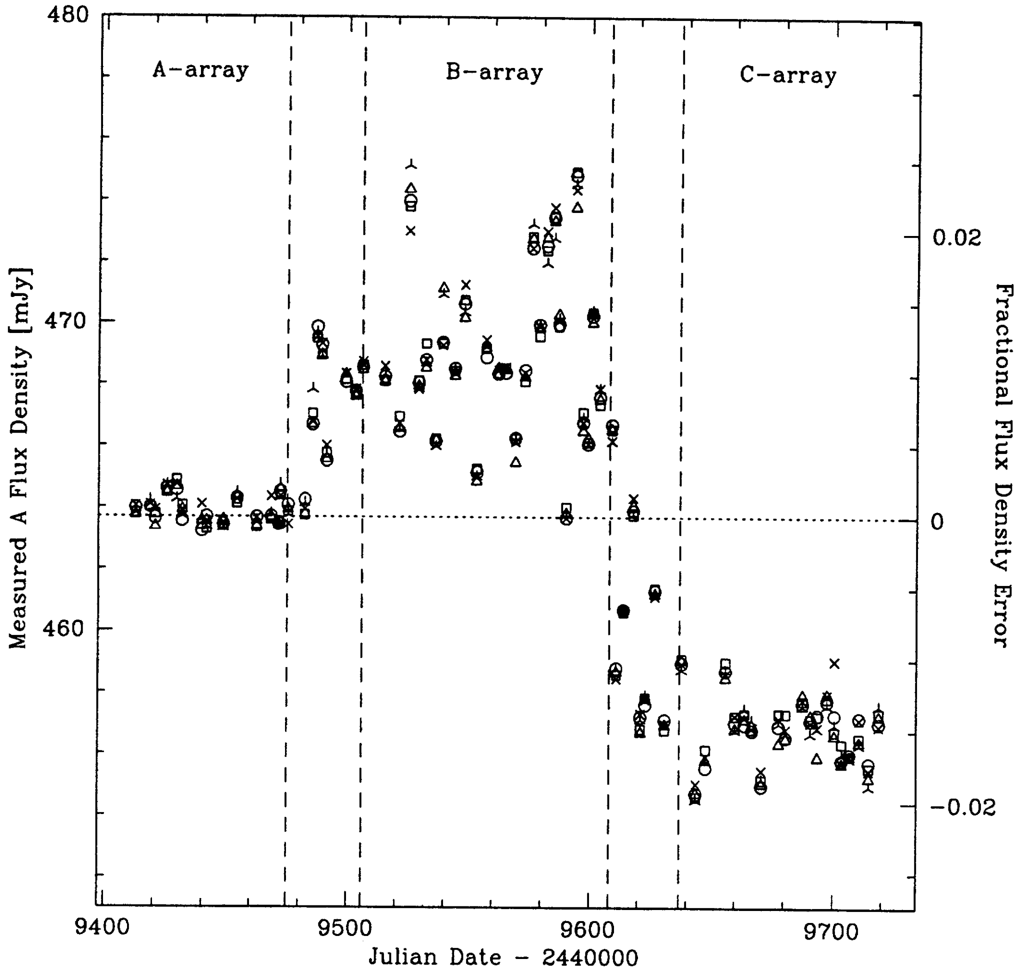

FIGURE 6.1: Results of the reduction of the 8 GHz "null test" data for A1+A2. Each of the five datasets is represented by a different plot symbol. They are identical in all respects except that each represents a different instantiation of the noise.

the flux density errors introduced by the deconvolution process for the particular source, uv-sampling, and noise present in a particular observation. It is important to note that the "null test" data include only gaussian noise that is assumed to be independent and identically distributed for different visibilities. Atmospheric phase delays cause changes in the visibility phase and are correlated both in time and space and change on timescales of minutes. The self-calibration process employed during the data reduction should remove most of these phase errors, but the residuals are not modelled in the "null test" data. The errors incurred in the measurement of the complex antenna gains on the phase calibrator

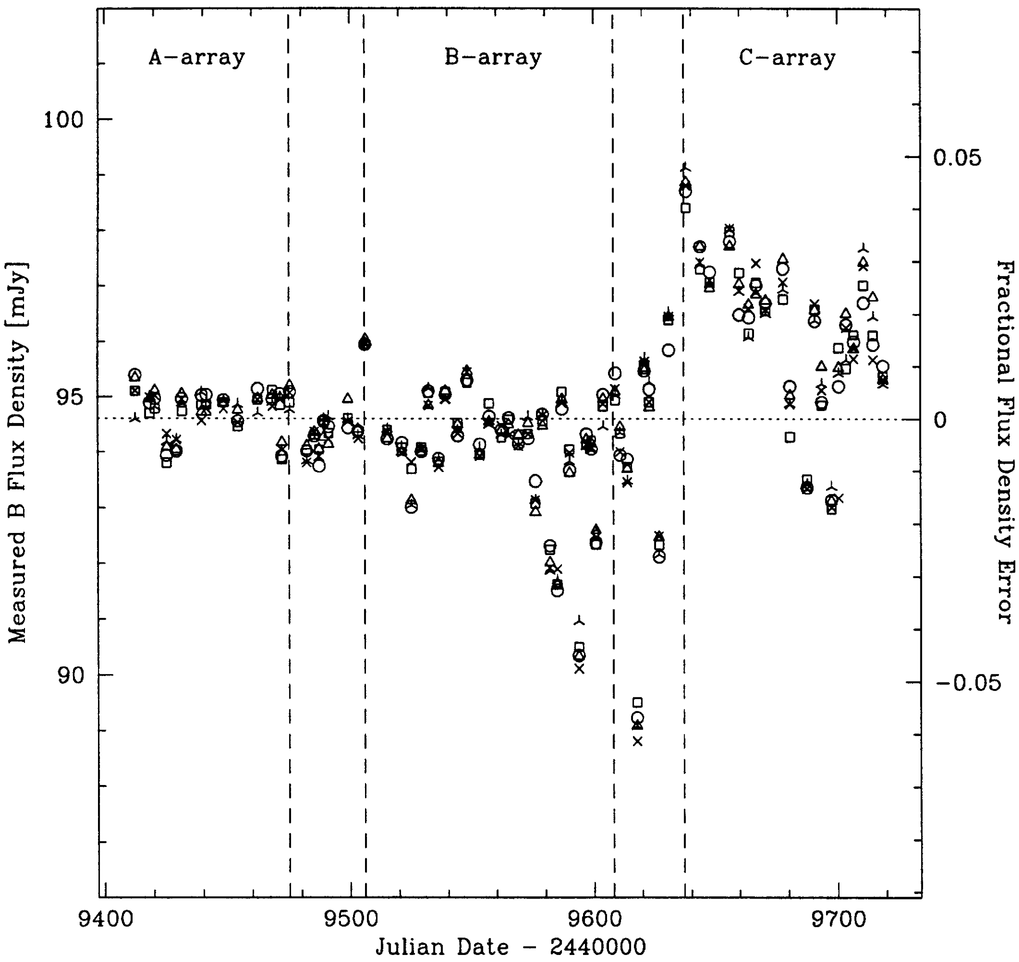

FIGURE 6.2: Results of the reduction of the 8 GHz "null test" data for image B. Each of the five datasets is represented by a different plot symbol.

are also not included in the "null test" data but should be very small since the signal-to-noise ratio in the phase calibrator observations is very large. The effect of flux density scale calibration errors is also unmodeled in the "null test" data, but such errors do not affect the deconvolution process.

In order to gain some confidence that the noise amplitude measured from the phase calibrator observation and then added to the synthetic data really charaterizes the noise in the data, we plot (in Figure 6.4) a comparison of the noise in maps of the simulated data to the noise in maps of the real data. Note that the relationship between the two has much less scatter than was present at 15 GHz (Figure 4.5). The noise in the map made from the

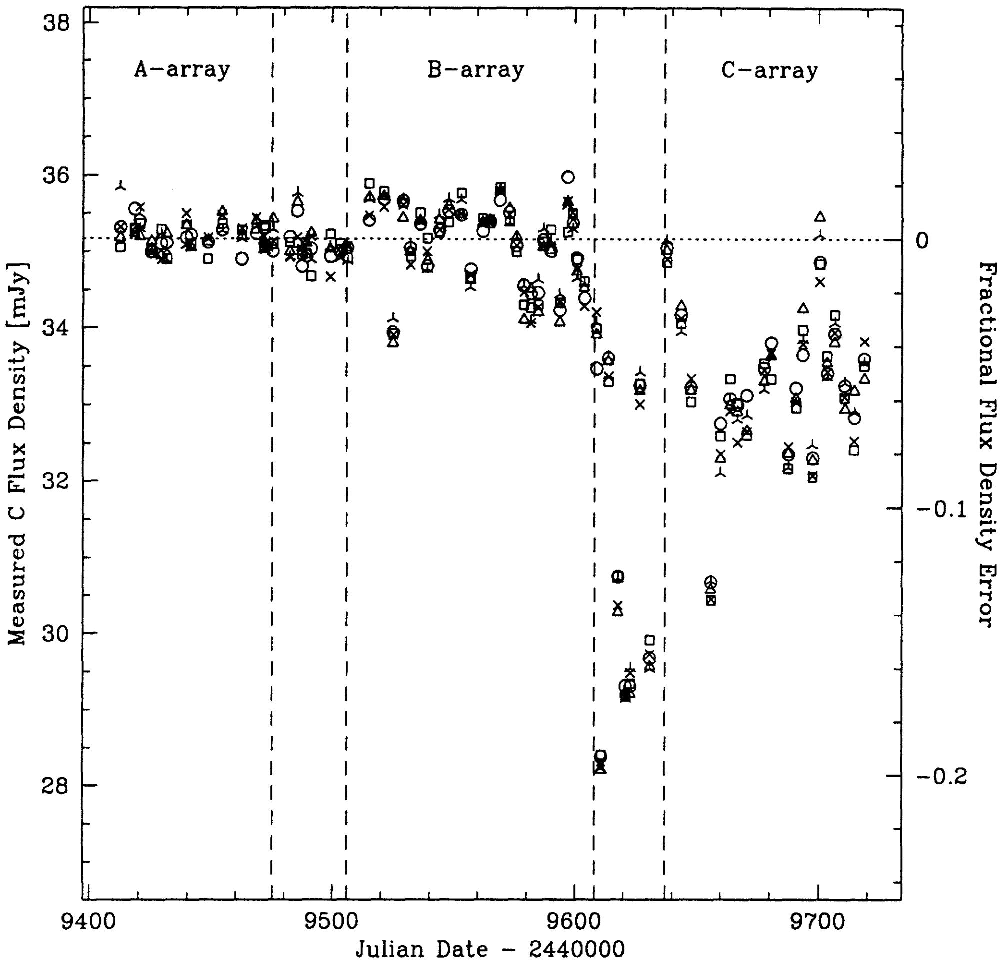

FIGURE 6.3: Results of the reduction of the 8 GHz "null test" data for image C. Each of the five datasets is represented by a different plot symbol.

real data is typically slightly higher than the noise in maps from simulated data indicating that there are some unmodelled errors (e.g. residual phase or amplitude calibration errors) that are not present in the "null test" data. There are also a few observations for which the map noise in the real data is larger than in the "null test" data by a factor of >2. Those particular observations of MG0414 are probably affected by some source of noise that was not present in the observations of the phase calibrator.

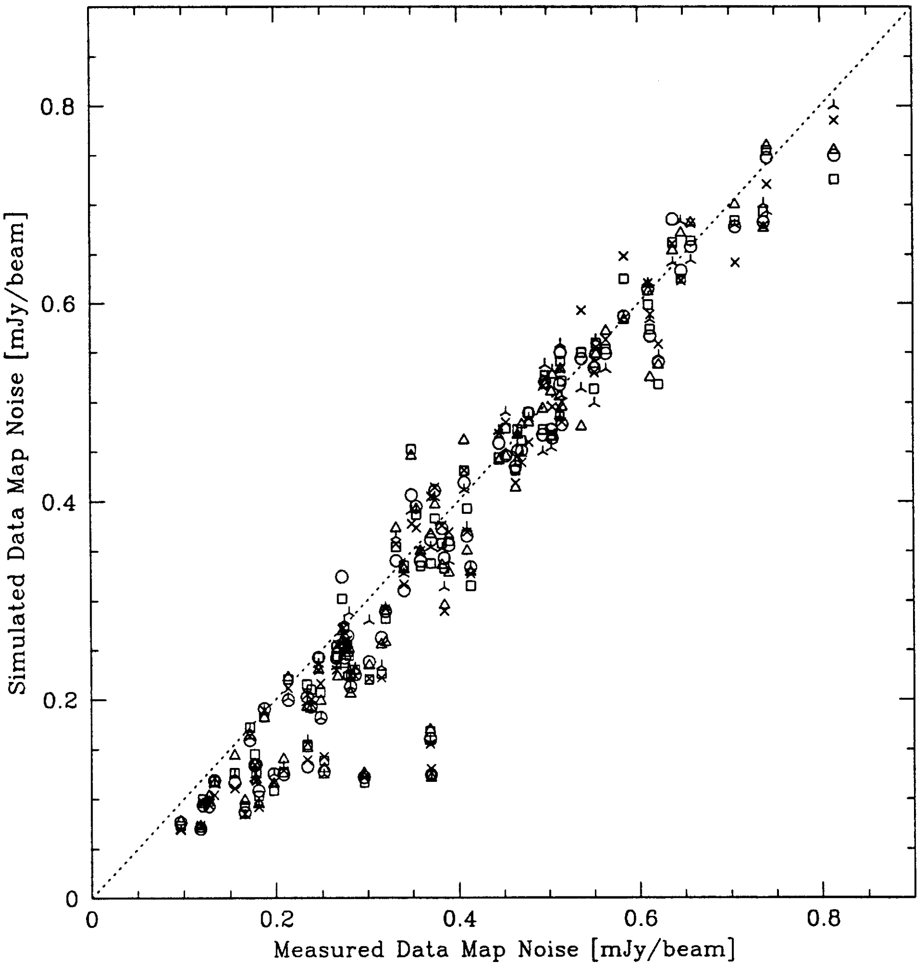

FIGURE 6.4: Comparison of the RMS noise in maps of the 8 GHz "null test" data to the RMS noise in maps of the real data.

6.2 Correcting for Deconvolution Errors

Given that the errors introduced by the deconvolution process appear to be reproducible and well measured by the reduction of the "null test" data, one can create a correction factor for each component in each observation. We calculate this correction for each component by averaging the flux density obtained from the five "null test" synthetic observations and finding a multiplicative factor which corrects this to the simulated flux from Table 6.1. The real data corrected by those factors is displayed in Figure 6.5. Note that the anomalous features in the lightcurves that began at the transition to C-array have been almost completely corrected. There are still many zero-lag correlations between the lightcurves but

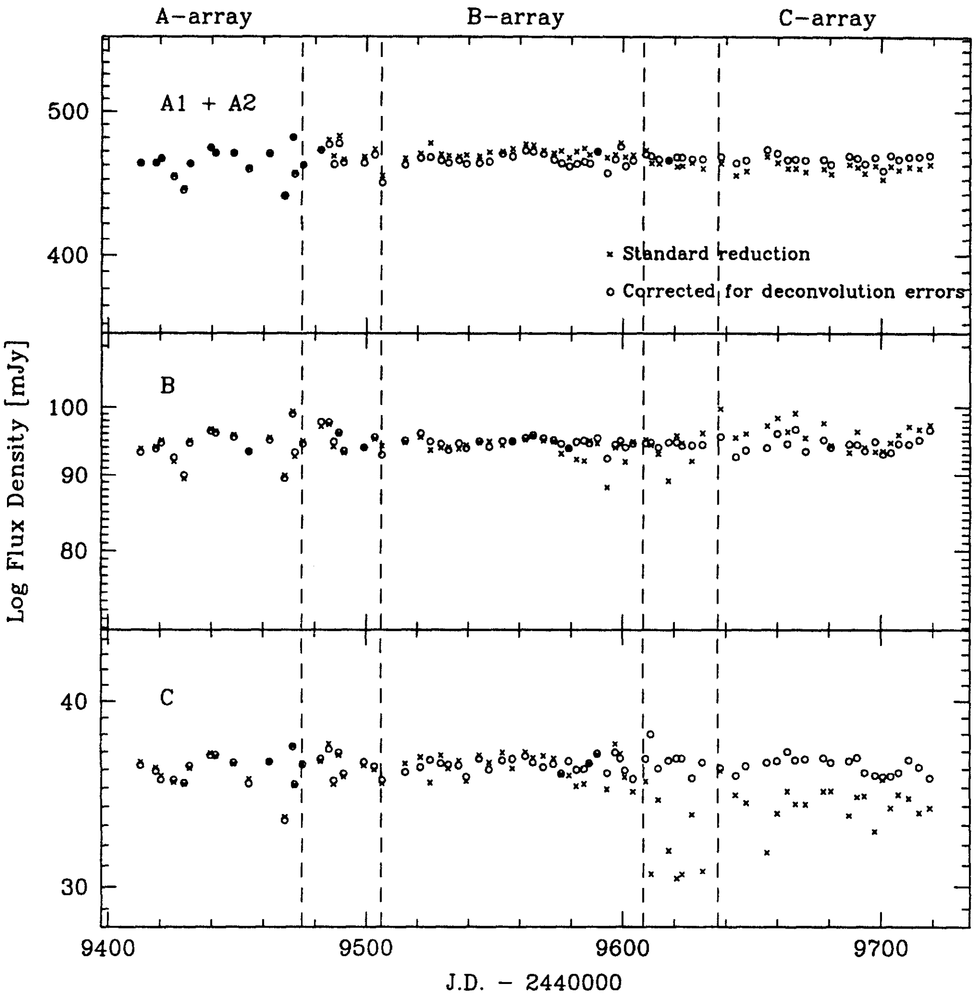

FIGURE 6.5: Comparison of the 8 GHz lightcurves before and after application of a correction for deconvolution errors. They are plotted on a log scale so that shifting is the same as scaling.

this is to be expected since the correction factor does not contain information about the flux calibration errors.

The RMS in the flux density measured before application of the correction factors is 1.7%, 2.2%, and 4.7% for images A, B, and C respectively. After correction the RMS in flux densities has decreased to 1.4%, 1.5%, and 1.7% respectively. It is important to note at this point that the correction factors perform extremely well and were calculated without reference to the flux densities measured in the real observations of MG0414. The only ingredients are the model of MG0414, the noise measured from the phase calibrator observations, and the uv-sampling of the real observation of MG0414.

6.3 Error Estimates

In order to test the quality of the correction obtained in this way, we test it by taking each of the "null test" datasets in turn and using the other four of the "null test" datasets to find a correction factor for it. The resulting corrected synthetic data are displayed in Figure 6.6. Note that the fractional scatter in the data corrected for deconvolution error is greatest in image C and (for all images) in the C-array data. Tables 6.3 and 6.4 display the RMS error in the flux density of the images measured from maps of the synthetic data before and after correction. Since the deconvolution errors might be correlated in the deconvolution

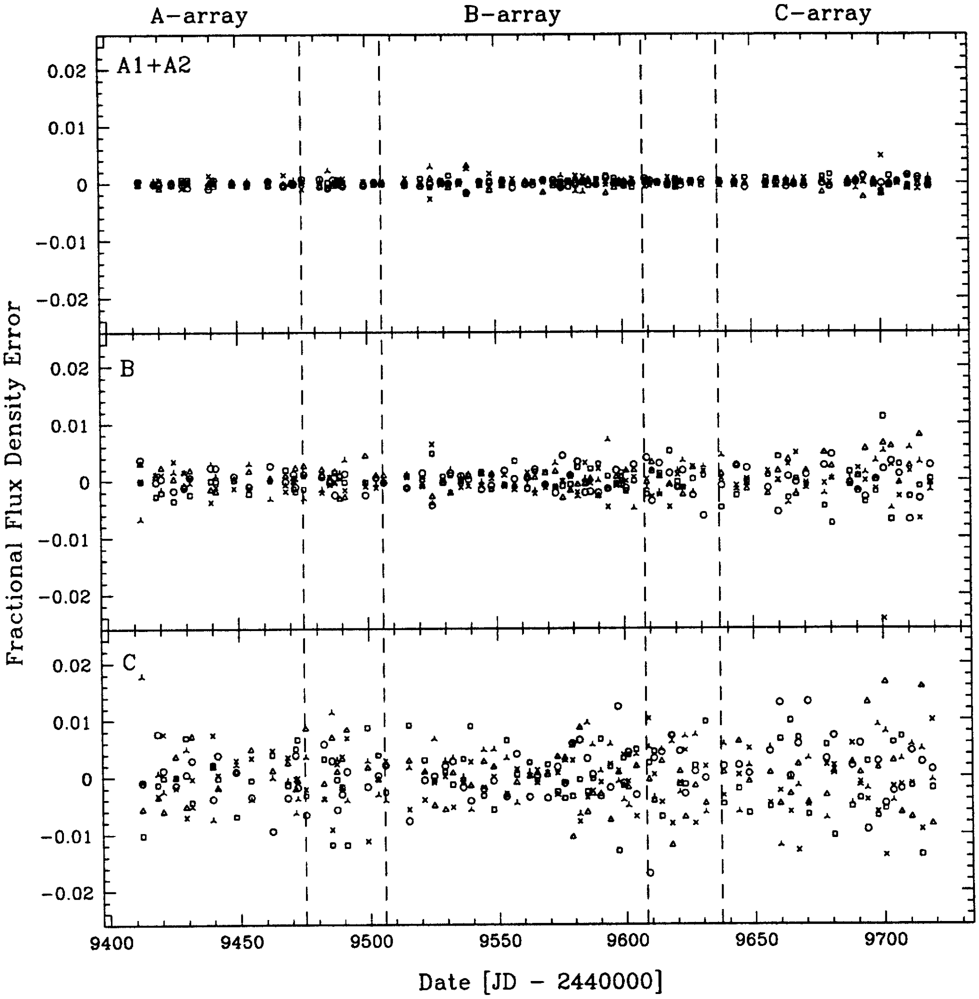

FIGURE 6.6: Fractional flux density errors after correcting each of the 8 GHz "null test" datasets using a correction factor derived from the other four. Each of the five datasets is represeted with a different plot symbol.

	Image A1+A2		Image B		Image C	
	Bias(%)	RMS(%)	Bias(%)	RMS(%)	Bias(%)	RMS(%)
A-array	0.049	0.096	0.125	0.413	0.111	0.522
B-array	1.142	0.581	−0.648	1.240	−0.221	1.496
C-array	−1.487	0.238	1.693	1.499	−5.531	2.798
mix-array	−0.017	0.924	−0.481	1.658	−6.080	7.253

TABLE 6.3: RMS error and bias in recovery of simulated flux densities before correction.

	Image A1+A2		Image B		Image C	
	Bias(%)	RMS(%)	Bias(%)	RMS(%)	Bias(%)	RMS(%)
A-array	0.000	0.045	0.000	0.188	0.001	0.467
B-array	0.000	0.078	0.000	0.187	0.000	0.409
C-array	0.000	0.084	0.000	0.404	0.001	0.624
mix-array	0.000	0.051	0.000	0.212	0.001	0.578

TABLE 6.4: RMS error and bias in recovery of simulated flux densities after correction.

process, we also include (in Table 6.5) the RMS error in the flux density ratios in the same corrected synthetic data. The bias in the recovery of both flux densities and flux density ratios is always consistent with zero.

The other important part of the error budget for the real data is due to flux calibration errors. Since these are not present in the "null test" simulations, we return to the real data (after application of the correction factors) to estimate their magnitude. We proceed by measuring the zero lag correlated variability and assuming that it comes primarily from

	(A1+A2):B		(A1+A2):C		B:C	
	Bias(%)	RMS(%)	Bias(%)	RMS(%)	Bias(%)	RMS(%)
A-array	0.000	0.199	0.002	0.464	0.002	0.563
B-array	0.000	0.215	0.001	0.422	0.001	0.421
C-array	0.002	0.476	0.003	0.656	0.003	0.637
mix-array	0.000	0.223	0.003	0.587	0.003	0.627

TABLE 6.5: RMS error and bias in recovery of simulated flux ratios after correction.

flux calibration errors. In order to turn the flux calibration error, which is multiplicative, into an additive error, we work in log units. Consider two signals,

$$\tilde{a}_i = a + C_i + N_{ai}$$

and

$$\tilde{b}_i = b + C_i + N_{bi},$$

where a and b are the (constant) source fluxes, and there is a zero-mean correlated noise C_i added to both $\tilde{a}_i$ and $\tilde{b}_i$. Each also is also affected by independent zero-mean noise N_{ai} or N_{bi}. In order to extract the statistics of the C_i, we start with the expected value of the square of the difference between two images in a single observation:

$$\begin{aligned} \left\langle (\tilde{a}_i - \tilde{b}_i)^2 \right\rangle &= \left\langle \tilde{a_i}^2 \right\rangle + \left\langle \tilde{b_i}^2 \right\rangle - \left\langle 2\tilde{a}_i\tilde{b}_i \right\rangle & (6.1) \\ &= \left\langle \tilde{a_i}^2 \right\rangle + \left\langle \tilde{b_i}^2 \right\rangle - 2ab - 2\left\langle C_i^2 \right\rangle . & (6.2) \end{aligned}$$

Note that $(a - b)^2$ is not known but that it can be estimated from the data. Given the above, it can be shown that the variance of the correlated noise is given by

$$\left\langle C^2 \right\rangle = \frac{1}{2}\left[\mathrm{Var}(\tilde{a}) + \mathrm{Var}(\tilde{b}) - \left\langle (\tilde{a}_i - \tilde{b}_i)^2 \right\rangle + (a - b)^2\right]. \tag{6.3}$$

Equation 6.3 may be applied to any pair of images in order to estimate the zero-lag correlated noise in the signal. Applying it to images A and B in the real data after application of the correction for deconvolution errors and calculating separately for each array gives correlated noise estimates of 2.6%, 0.87%, and 0.67% for the A, B, and C arrays respectively. We take these correlated noise estimates as estimates of the flux calibration error. The 2.6% error in A-array is consistent with standard VLA calibration techniques. The <1% calibration errors achieved by this technique in B and C arrays are far better than previously achieved with the VLA.

6.4 Minimum Dispersion Analysis

Pelt, *et al.* (1994; 1996) have proposed a non-parametric time delay estimator that is based on the assumption that nearby points on the lightcurve should have small dispersion. This has an advantage over the technique of Press, Rybicki, and Hewitt (1992c; 1992b) in that it does not require estimation of the structure function of the source nor does it assume that it is stationary. The cost of this advantage is that the minimum dispersion technique can only compare nearby points and therefore gives up many of the lag pairs that are available to the technique of Press, *et al.*.

Consider the problem of finding the time delay between two image lightcurves each with N observations. Pelt, *et al.* define a combined lightcurve, C_k, which is the union of the two image lightcurves after shifting in time by an assumed lag, τ, and scaling by a flux ratio, r. Their dispersion $D^2_{4,2}$ is defined as

$$D^2_{4,2} = \frac{\sum_{n=1}^{2N-1} \sum_{m=n+1}^{2N} S^{(2)}_{n,m} W_{n,m} G_{n,m} (C_n - C_m)^2}{\sum_{n=1}^{2N-1} \sum_{m=n+1}^{2N} S^{(2)}_{n,m} W_{n,m} G_{n,m}}, \tag{6.4}$$

where $G_{n,m}$ is defined to be unity if observations C_n and C_m come from different images and is zero otherwise, $W_{n,m}$ is a statistical weight equal to $\frac{W_n W_m}{W_n + W_m}$ where W_n and W_m are the statistical weights of observations n and m, and $S^{(2)}_{n,m}$ is a weighting depending on the temporal distance (at the source) between observations n and m,

$$S^{(2)}_{n,m} = \begin{cases} 1 - \frac{|t_n - t_m|}{\delta} & \text{if } |t_n - t_m| \leq \delta \\ 0 & \text{if } |t_n - t_m| > \delta \end{cases}, \tag{6.5}$$

where t_n is the time (at the source) of C_n. One then constructs a "dispersion spectrum" by assuming a variety of delays and for each, taking

$$D^2_{4,2}(\tau) = \min_r D^2_{4,2}(\tau, r). \tag{6.6}$$

We take the value of δ to be 10 days, a value somewhat more conservative than Pelt, *et al.* use in their analysis of the 0957+561 data but appropriate to the magnitude of the time delays that we hope to measure in MG0414.

Performing the above analysis for the corrected data on the real A and B lightcurves and on the five synthetic lightcurves from the "null test" yields the dispersion spectra shown in Figure 6.7. Note first that dispersion spectra from the real and synthetic data seem quite different from each other. This is not unexpected since the synthetic data do not contain flux scale calibration errors. The real data appear to favor $\tau < 0$ which implies

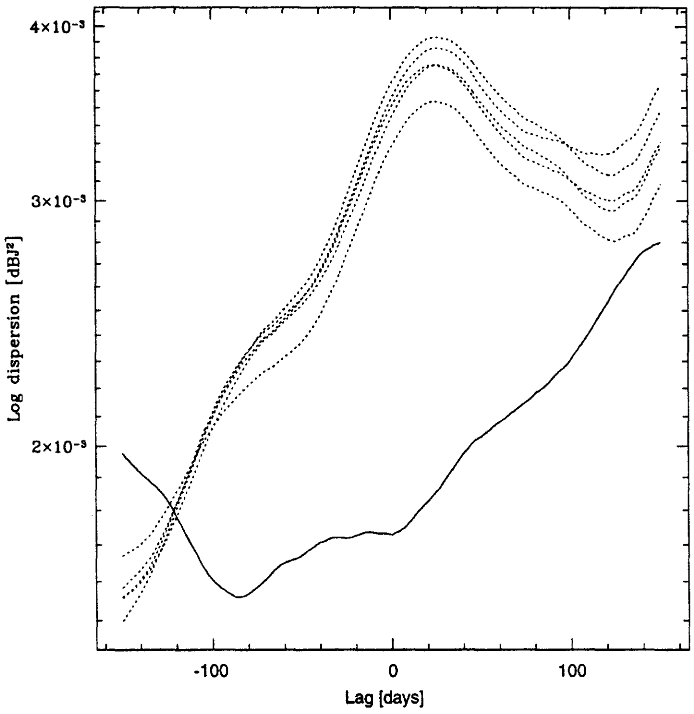

FIGURE 6.7: Pelt, *et al.* dispersion spectra for images A and B from the real 8 GHz data (solid line) and the five "null test" datasets (dotted lines). The units on the vertical axis are dBJ, decibels referenced to 1 Jy.

that image B leads A consistent with expectations from lens modelling. However, the synthetic data (where there is no delay at all) do the exactly the same thing. There is also a tempting minimum in the dispersion spectrum of the real data at $\tau = -87$ days but there are structures in the synthetic data at the same amplitude making it difficult to believe that this is a signature of a real delay.

6.5 Changes in the Flux Ratios

In order to consider the data in a regime where the errors are best quantified, we examine the behavior of the flux density ratios. Here, we are unaffected by errors in the flux density calibration and have the benefit of the "null test" data to estimate the amplitude of the errors introduced in the deconvolution process. Figure 6.8 displays the flux density ratios relative to image B. Also shown are linear fits to the flux density ratio as a function of time.

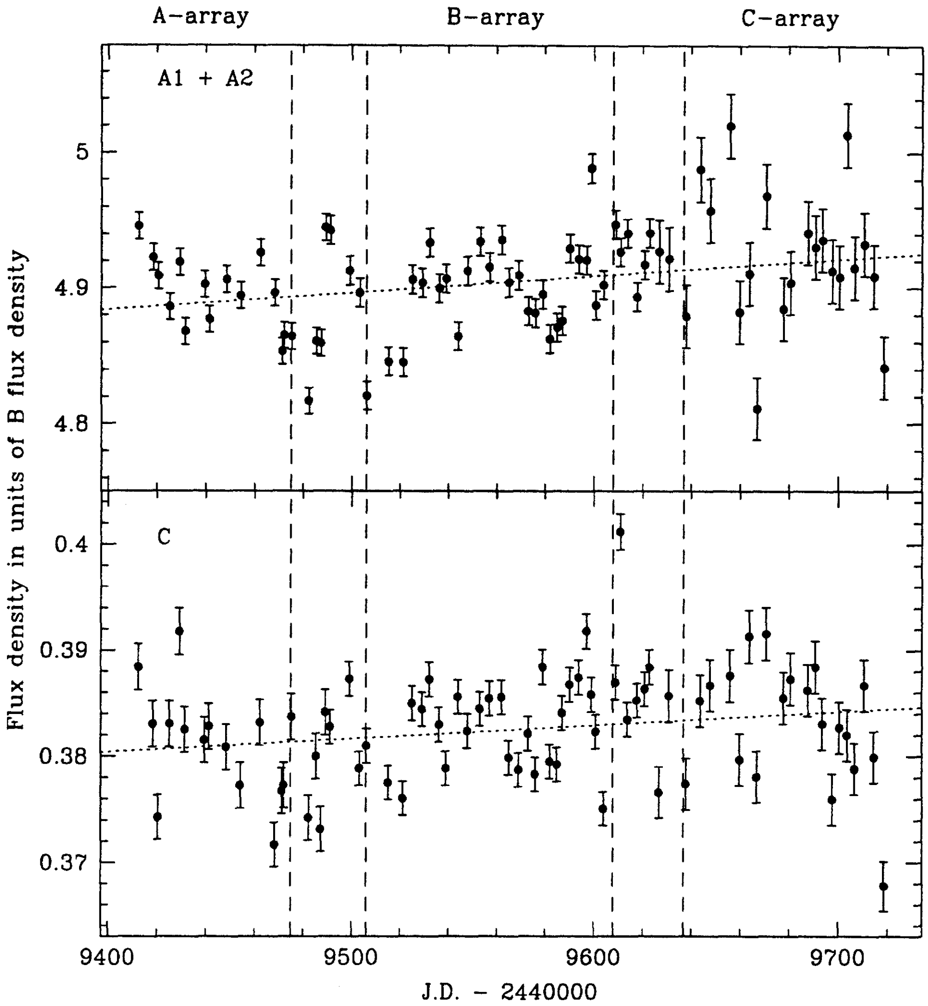

FIGURE 6.8: 8 GHz flux density ratios of A1+A2 and C relative to B. Also shown are linear fits to the data. However, the linear fits are not significantly better than fitting by a constant.

The χ^2 per degree of freedom for the two fits is 9.3 and 7.6 for the A1+A2 and C data respectively. Using the "F-test" we find that these linear fits are better than fitting by a constant at only the 23% and 12% confidence levels respectively. The large χ^2 associated with these fits is a clear indication of some variability that is not described by the error model derived from the "null test" data.

Image	mJy	Change (%) from initial model
A1	244.756	+0.05
A2	219.193	+0.05
B	94.564	-0.05
C	36.191	+2.90

TABLE 6.6: Average 8 GHz flux densities for the images after application of the correction for deconvolution errors. Also listed is the change (in percent) with respect to the initial "null test" model (see Table 6.1).

6.6 Effect of Changing the "null test" Model

The corrections for deconvolution errors found from the "null test" data include a large correction for image C particularly for the C-array observations. After the correction is made, the average flux density for image C (over the whole dataset) is increased by 2.9%. Table 6.6 lists the average flux densities after application of the correction for deconvolution errors. Since the "null test" data depend on the MG0414 model in a complicated way, the large change in the average flux density for image C suggests the construction of a "second null test" dataset using a model based on the average flux densities in Table 6.6. We have constructed such a dataset and again performed the data reduction as described in section 4.2. The results look much like those discussed in relation to the original "null test" data so we will focus on the differences between the corrections for deconvolution error derived from the two.

Figure 6.9 displays the difference between multiplicative deconvolution error correction factors derived from the "second null test" and "null test" data. Note that changes between the two sets of correction factors can amount to as much as one percent and seem concentrated in the C-array and in image C. The average fluxes of the images after application of the "second null test" correction factors is consistent with the "second null test" model to better than 0.02% for images A and B and to better than 0.07% for image C. It appears that iterative use of this technique is convergent in this case. The error after correction by factors derived from the "second null test" is characterized in the same way as before (see section 6.3) yielding the biases and error estimates listed in Tables 6.7 and 6.8.

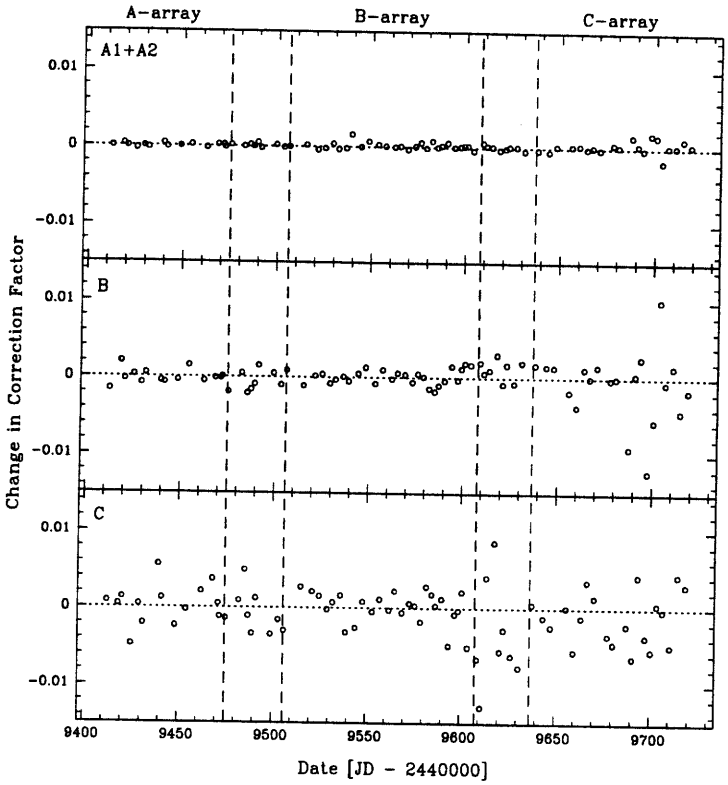

FIGURE 6.9: The difference between multiplicative deconvolution error correction factors derived from the "second null test" and the "null test" data.

	Image A1+A2		Image B		Image C	
	Bias(%)	RMS(%)	Bias(%)	RMS(%)	Bias(%)	RMS(%)
A-array	0.000	0.053	0.000	0.164	0.000	0.389
B-array	0.000	0.053	0.000	0.196	0.000	0.423
C-array	0.000	0.093	0.001	0.553	0.001	0.545

TABLE 6.7: Bias and RMS error in recovery of simulated flux densities after correction by the factors calculated from the "second null test" data.

6.6.1 Testing for Variability After "Second Null Test" Correction

After application of the correction factors derived from the "second null test" data, we find total RMS variability (over the whole dataset) of 1.4%, 1.5%, and 1.7% for the A1+A2, B, and C images respectively. The RMS for each array is shown in Table 6.9.

	(A1+A2):B		(A1+A2):C		B:C	
	Bias(%)	RMS(%)	Bias(%)	RMS(%)	Bias(%)	RMS(%)
A-array	0.000	0.175	0.001	0.398	0.001	0.423
B-array	0.000	0.203	0.002	0.436	0.001	0.398
C-array	0.003	0.639	0.003	0.568	0.003	0.734

TABLE 6.8: Bias and RMS error in recovery of simulated flux density ratios after correction by the factors calculated from the "second null test" data.

	Number of Observations	RMS Variability (%)		
		A1+A2	B	C
A-array	14	2.5	2.6	2.8
B-array	27	1.1	0.78	1.2
C-array	20	0.69	1.2	1.2
Mixed-array	16	1.0	1.3	1.7
All Observations	77	1.4	1.5	1.7

TABLE 6.9: RMS variability in image flux densitites for various parts of the data after application of the "second null test" correction factors.

	(A1+A2):B RMS(%)	(A1+A2):C RMS(%)	cB:C RMS(%)
A-array	0.56	1.19	1.41
B-array	0.69	0.95	1.08
C-array	1.03	1.20	1.37

TABLE 6.10: RMS variability in flux density ratios of the 8 GHz observations after correction by the factors calculated from the "second null test" data.

Examining the final corrected lightcurves displayed in Figure 6.11 shows that there is still signal that is correlated with itself at short timescales and is correlated between images at nearly zero-lag. Since nearby observations are often observed at similar sidereal times, the UV-sampling is also similar. This could lead to flux calibration errors with timescales of $\sim$ 20 days such as those that are present in the data.

Going back to the flux density ratios where the situation is clearer, we first compare the RMS variations in the flux ratios of the corrected real data to the same quantity in the simulated data (shown in Table 6.8). Since that RMS variations in the corrected real data (see Table 6.10) are a factor of 1.6–3.4 larger than those observed in the synthetic data, we conclude that either the synthetic data are generated by an incomplete model of the observation (see below) or that there is some real variability in the image flux ratios. In order to characterize the variations, we use the non-parametric Kendall-τ test to find correlations in the flux density ratios (see Press, *et al.* 1992). We find that the ratios A:B and C:B are correlated in the simulated data (all five "second null test" datasets taken together) at >99.99999% confidence. The measured value of Kendall's τ is 0.2425 ± 0.0049. The same two ratios are correlated in the real data after correction by the "second null test" correction factors (at 99.99999% confidence) with $\tau = 0.351 \pm 0.023$. Taking the two measured τ's, we find that the A:B and C:B ratios are more correlated in the real data than in the simulated data since $\tau_{\rm real} - \tau_{\rm sim} = 0.109 \pm 0.023$ but the significance of this result is difficult to gauge without further simulations. As a check to see that the correlations in the corrected data were not somehow induced by the correlations in the simulations and therefore the correction factors, we checked the raw data and found that A:B and C:B are more correlated there than in the corrected data.

A correlation in flux density ratios at zero lag (as we have calculated it) might come about if image B varies or if images A and C are varying with a time delay that is short compared to the time scale for the variability. It is also possible that the error model, which is derived from the "second null test" simulations, is deficient in some important way. This could be due to residual phase errors resulting from atmospheric phase delays that are not completely corrected by phase self-calibration. These are present in the real data but not in the simulations. Also in the data but not in the simulations are errors from use of the phase calibration source to set the complex gains of the antennae. These errors could also be included in the simulations but should be quite small. Addition of these two effects is postponed for now since the implementation of a model atmosphere for computation of the phase delay errors is complicated and exploration of its effect would require a large number of simulated datasets.

For completeness, we have duplicated the minimum dispersion analysis of section 6.4 using the "second null test" corrections. Figure 6.7 is now reproduced with the "second null test" corrected data and simulations in Figure 6.10. As before, the structure in the dispersion curves of the simulated data makes it unlikely that the structure in the dispersion curve of the real data is significant.

6.7 Conclusion

By using a model of MG0414 to simulate the uv-data for each observation (with noise) and then reducing the data as usual, we have measured the errors introduced by the deconvolution process. Since the deconvolution errors are reproducible, we can use the errors in the simulated ("null test") data to correct the real observations. Doing so changes the average flux densities of the images (particularly image C) and therefore prompts a change in the model and a new set of simulated data. After application of correction factors obtained from the "second null test" data, the average flux densities in the data are consistent with the model, giving confidence that the process is convergent. The measured flux densities of the images of MG0414 after application of the correction factors from the "second null test" data are listed in Table 6.11 and displayed in Figure 6.11.

After application of the flux density correction from the "second null test" data, the RMS in the lightcurves is 1.4%, 1.5%, and 1.7% for the A1+A2, B, and C images respectively.

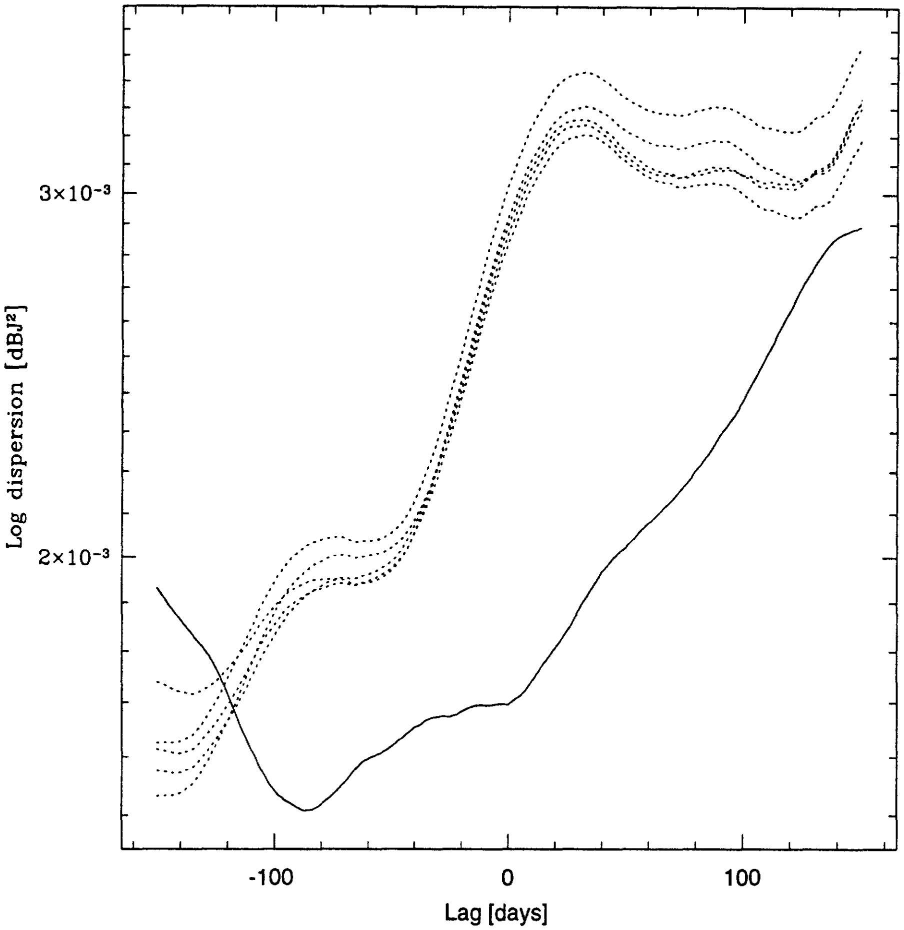

FIGURE 6.10: Pelt, *et al.* dispersion spectra for images A and B from the real 8 GHz corrected data (solid line) and the five "second null test" datasets (dotted lines). The units on the vertical axis are dBJ, decibels referenced to 1 Jy.

This is a factor of 1.2–2.8 smaller than the RMS before application of the correction. The flux density ratios (displayed in Figure 6.12) are inconsistent with both constant and linearly changing fits and show a statistically significant correlation between the A:B and C:B ratios. The source of this correlation could be variability but may be errors that are unmodelled in the "second null test" data. Effects that may be important here include errors in the complex antenna gains set by observation of the phase calibrator and residuals from self-calibration of atmospheric phase delays.

The deconvolution error correction technique described here is applicable to any source

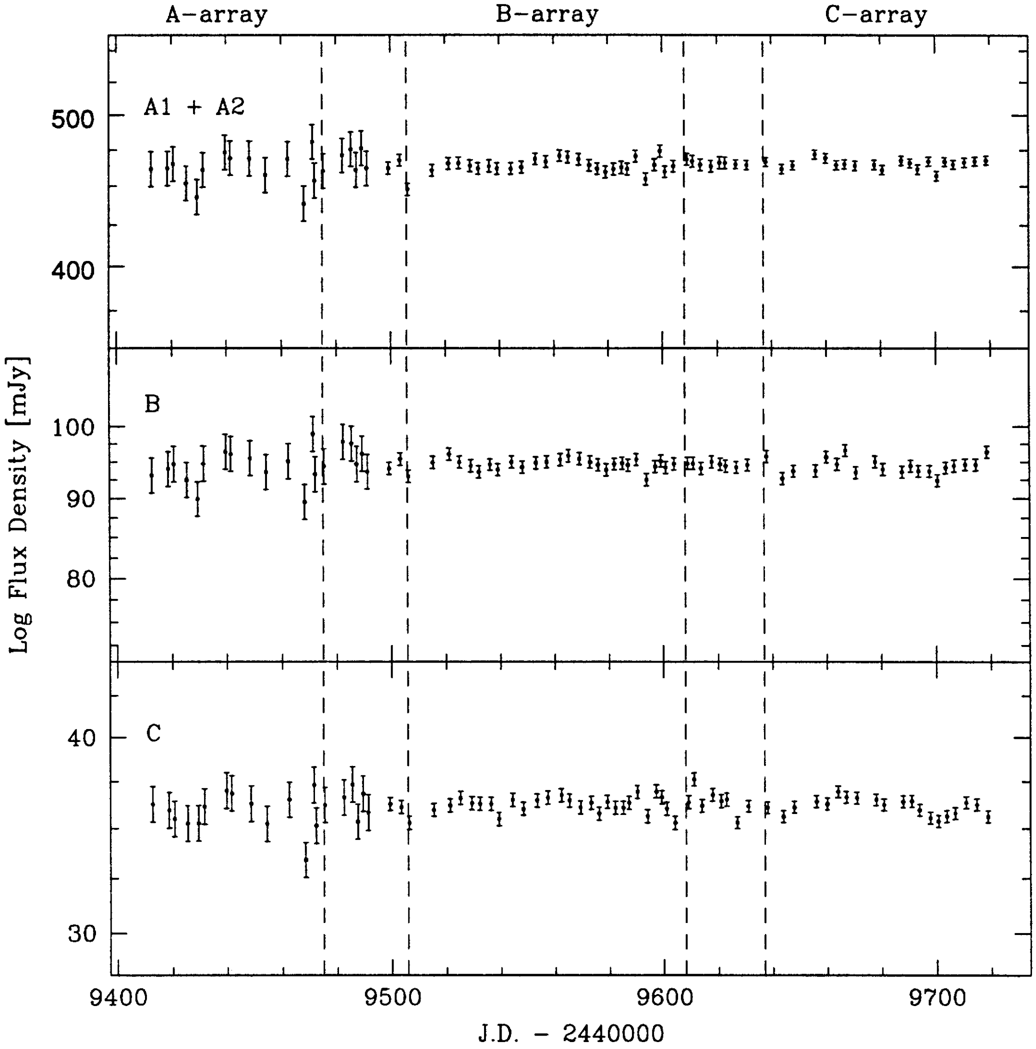

FIGURE 6.11: 8 GHz lightcurves for all images after application of correction factors derived from the "second null test" data. They are shown on a log scale so that shifting is the same as scaling. Error bars come from adding the estimates of the flux calibration error (see section 6.3) and the residual deconvolution error (see table 6.7) in quadrature.

which is simple enough to be well modelled. However, the technique did not work as well on the 15 GHz data and it is unclear if the problem lies in the interaction of the beam with the morphology of the source or if the lower signal to noise is to blame.

In the final corrected data, the flux calibration error is estimated to be 2.6%, 0.87%, and 0.67% for the A, B, and C arrays respectively. Estimates of residual deconvolution errors are less than 0.09%, 0.55%, and 0.55% for the A1+A2, B, and C images respectively (see

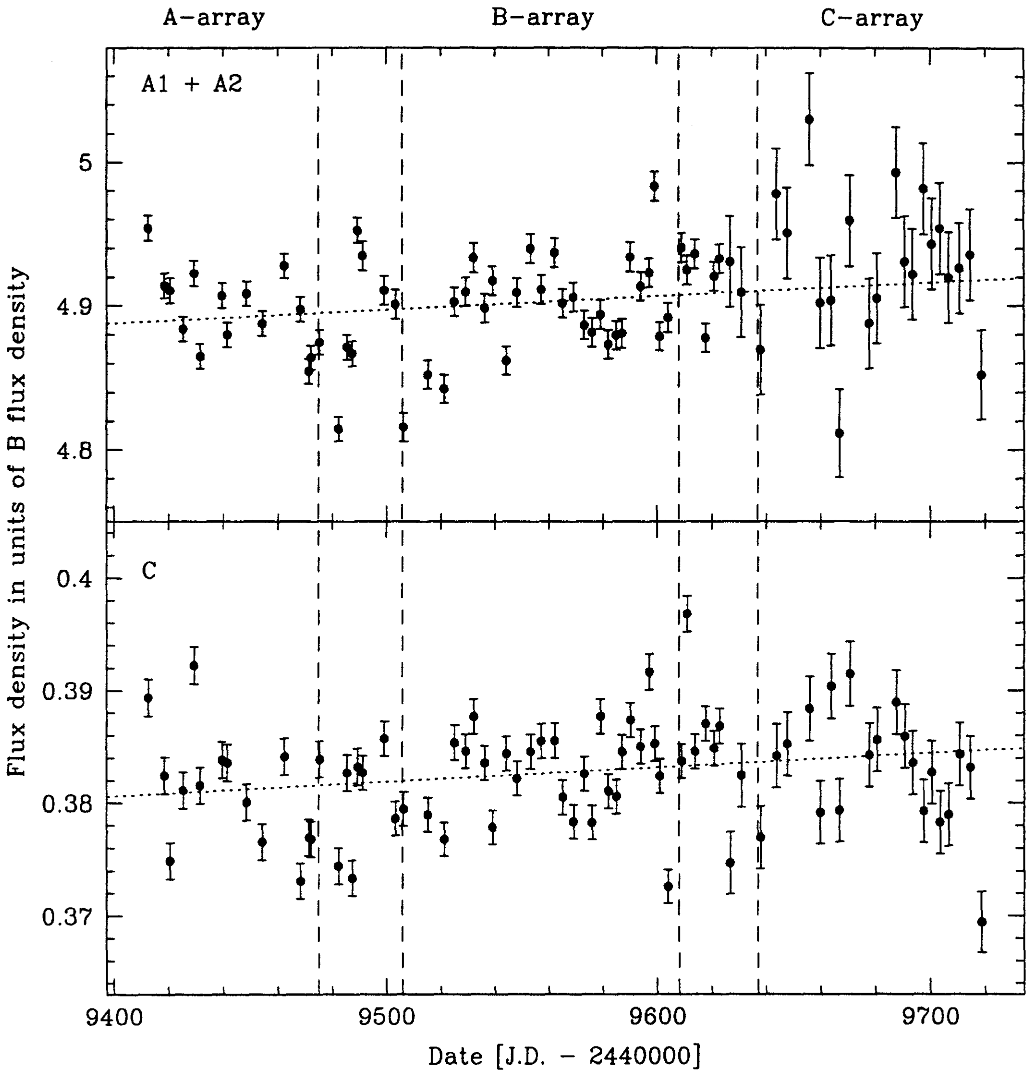

FIGURE 6.12: 8 GHz flux density ratios of A1+A2 and C relative to B after application of corrections derived from the "second null test" simulations. Also shown are linear fits to the data. However, the linear fits are not significantly better than fitting by a constant. Error bars come from adding the estimates of the flux calibration error (see section 6.3) and the residual deconvolution error (see table 6.7) in quadrature.

Table 6.7 for more detail).

Julian Date	Flux Density (mJy)		
-2440000	Image A	Image B	Image C
9412.560	461.5 ± 12.0	93.16 ± 2.43	36.27 ± 0.95
9418.481	462.0 ± 12.0	94.01 ± 2.45	35.95 ± 0.95
9420.517	465.1 ± 12.1	94.71 ± 2.47	35.50 ± 0.93
9425.317	451.9 ± 11.7	92.52 ± 2.41	35.26 ± 0.93
9429.325	442.8 ± 11.5	89.95 ± 2.35	35.28 ± 0.93
9431.540	460.9 ± 12.0	94.74 ± 2.47	36.15 ± 0.95
9439.592	473.1 ± 12.3	96.41 ± 2.52	37.00 ± 0.97
9441.524	469.0 ± 12.2	96.10 ± 2.51	36.86 ± 0.97
9448.544	468.8 ± 12.2	95.51 ± 2.49	36.30 ± 0.95
9454.342	457.4 ± 11.9	93.58 ± 2.44	35.24 ± 0.93
9462.467	468.5 ± 12.2	95.07 ± 2.48	36.52 ± 0.96
9468.386	438.6 ± 11.4	89.55 ± 2.34	33.41 ± 0.88
9471.473	480.5 ± 12.5	98.98 ± 2.58	37.31 ± 0.98
9472.209	453.7 ± 11.8	93.27 ± 2.43	35.14 ± 0.92
9475.388	460.1 ± 12.0	94.38 ± 2.46	36.23 ± 0.95
9482.388	471.0 ± 12.2	97.83 ± 2.55	36.63 ± 0.96
9485.466	475.3 ± 12.4	97.57 ± 2.55	37.34 ± 0.98
9487.377	460.8 ± 12.0	94.68 ± 2.47	35.35 ± 0.93
9489.362	476.0 ± 12.4	96.12 ± 2.51	36.83 ± 0.97
9491.281	462.0 ± 12.0	93.62 ± 2.44	35.83 ± 0.94
9499.280	462.0 ± 4.0	94.06 ± 0.84	36.28 ± 0.35
9503.372	467.5 ± 4.1	95.39 ± 0.85	36.12 ± 0.35
9506.284	447.9 ± 3.9	93.00 ± 0.83	35.29 ± 0.34
9515.301	460.5 ± 4.0	94.90 ± 0.85	35.96 ± 0.35
9521.304	465.4 ± 4.1	96.10 ± 0.86	36.21 ± 0.35
9525.086	465.6 ± 4.1	94.96 ± 0.85	36.59 ± 0.35
9529.274	463.8 ± 4.0	94.46 ± 0.84	36.33 ± 0.35
9532.232	461.8 ± 4.0	93.60 ± 0.83	36.29 ± 0.35
9536.296	463.5 ± 4.0	94.62 ± 0.84	36.29 ± 0.35
9539.172	461.8 ± 4.0	93.91 ± 0.84	35.48 ± 0.34
9544.220	461.8 ± 4.0	94.97 ± 0.85	36.51 ± 0.35
9548.147	462.7 ± 4.0	94.25 ± 0.84	36.02 ± 0.35
9553.239	468.6 ± 4.1	94.86 ± 0.85	36.48 ± 0.35
9557.164	466.6 ± 4.1	95.00 ± 0.85	36.62 ± 0.35
9562.170	470.7 ± 4.1	95.34 ± 0.85	36.76 ± 0.36
9565.162	469.9 ± 4.1	95.86 ± 0.86	36.47 ± 0.35
9569.193	468.2 ± 4.1	95.43 ± 0.85	36.10 ± 0.35
9573.141	464.1 ± 4.0	94.98 ± 0.85	36.34 ± 0.35
9576.029	461.8 ± 4.0	94.59 ± 0.84	35.78 ± 0.35
9579.085	459.4 ± 4.0	93.87 ± 0.84	36.39 ± 0.35
9581.992	461.5 ± 4.0	94.69 ± 0.84	36.08 ± 0.35
9584.964	462.6 ± 4.0	94.80 ± 0.85	36.08 ± 0.35
9587.052	461.5 ± 4.0	94.54 ± 0.84	36.35 ± 0.35
9590.180	470.5 ± 4.1	95.35 ± 0.85	36.93 ± 0.36
9593.899	454.8 ± 4.0	92.54 ± 0.83	35.63 ± 0.34
9597.098	464.4 ± 4.0	94.33 ± 0.84	36.94 ± 0.36
9599.124	473.9 ± 4.1	95.10 ± 0.85	36.64 ± 0.35
9600.951	459.7 ± 4.0	94.21 ± 0.84	36.02 ± 0.35
9604.016	463.4 ± 4.0	94.73 ± 0.85	35.30 ± 0.34
9609.002	468.3 ± 4.1	94.78 ± 0.85	36.37 ± 0.35

continued on next page.

Julian Date	Flux Density (mJy)		
-2440000	Image A	Image B	Image C
9610.997	466.8 ± 4.1	94.78 ± 0.85	37.61 ± 0.36
9613.947	464.5 ± 4.1	94.09 ± 0.84	36.19 ± 0.35
9617.874	463.4 ± 4.0	94.99 ± 0.85	36.76 ± 0.36
9620.991	465.8 ± 4.1	94.66 ± 0.84	36.43 ± 0.35
9622.985	465.7 ± 4.1	94.41 ± 0.84	36.52 ± 0.35
9626.912	464.6 ± 3.1	94.23 ± 0.82	35.30 ± 0.31
9630.984	464.2 ± 3.1	94.56 ± 0.82	36.16 ± 0.31
9637.986	466.3 ± 3.2	95.76 ± 0.83	36.10 ± 0.31
9643.844	461.5 ± 3.1	92.71 ± 0.81	35.62 ± 0.31
9647.853	464.0 ± 3.1	93.72 ± 0.81	36.10 ± 0.31
9655.995	471.6 ± 3.2	93.75 ± 0.81	36.41 ± 0.31
9659.925	469.0 ± 3.2	95.68 ± 0.83	36.27 ± 0.31
9663.894	464.2 ± 3.1	94.66 ± 0.82	36.95 ± 0.32
9666.907	464.9 ± 3.1	96.61 ± 0.84	36.65 ± 0.32
9670.760	463.8 ± 3.1	93.53 ± 0.81	36.61 ± 0.32
9677.813	464.5 ± 3.1	95.03 ± 0.83	36.52 ± 0.32
9680.681	461.0 ± 3.1	93.97 ± 0.82	36.24 ± 0.31
9687.681	467.4 ± 3.2	93.61 ± 0.81	36.41 ± 0.31
9690.821	465.6 ± 3.1	94.44 ± 0.82	36.45 ± 0.31
9693.645	461.4 ± 3.1	93.74 ± 0.81	35.95 ± 0.31
9697.654	466.8 ± 3.2	93.71 ± 0.81	35.54 ± 0.31
9700.584	456.9 ± 3.1	92.44 ± 0.80	35.38 ± 0.31
9703.636	466.6 ± 3.2	94.19 ± 0.82	35.63 ± 0.31
9706.713	464.7 ± 3.1	94.46 ± 0.82	35.80 ± 0.31
9710.723	466.1 ± 3.2	94.62 ± 0.82	36.36 ± 0.31
9714.609	466.9 ± 3.2	94.60 ± 0.82	36.25 ± 0.31
9718.682	467.6 ± 3.2	96.38 ± 0.84	35.61 ± 0.31

Table 6.11: Measured 8 GHz flux densitites now corrected for deconvolution effects

Chapter 7

An Experiment to Measure Microlensing Time Delays

7.1 Introduction

The gravitational lens time delays discussed in section 1.4 are usually thought of in the context of delays produced by large scale lenses (e.g. galaxies or clusters of galaxies) where the differential delay between images is hours to years. In the microlensing regime (see section 1.3), the differential time delays are of order microseconds. The detection of time delays resulting from galactic microlenses is difficult because the probability of lensing is small and the expected length of the microlensing event so short that one must monitor millions of sources simultaneously. For the extragalactic case, the density of lenses along the line of sight can increase (if there is a galaxy along the line of sight) but the density of bright background sources decreases and it can be difficult to distinguish lensing from intrinsic source variability. Detection of microlensing time delays would confirm the existence of compact masses in other galaxies or galaxy halos ("MACHOs") and would directly demonstrate the existence of high apparent brightness temperature sources that have thus far only been inferred from variability arguments (see section 7.2). Since a measurable change in the autocorrelation spectrum can occur in a period of a year, one can also use microlensing time delays to measure transverse velocities of the lensing masses much as is done in galactic microlensing experiments. Furthermore, the shape of the autocorrelation spectrum gives some information on source structure though it is complicated by the fact that annuli centered at the lens position all appear at the same location in the autocorrelation spectrum.

The idea that gravitational microlensing introduces time delays that might be observable was first mentioned by Canizares (1981). It has since been discussed in the literature from different perspectives. Schneider & Schmid-Burgk (1985) describe the coherent correlation between two microlensed images in terms of an equivalent VLBI experiment with a baseline of $\sim 10^{16}$ cm and work out analytic expectations of the signal for a few specific geometries. Peterson & Falk (1991) independently proposed that a difference in path lengths due to lensing would create a ripple in the power spectrum corresponding to the changing constructive and destructive interference as a function of frequency. They note that the drift in flux density calibration over the integration times necessary to detect lensing time delays make their experiment difficult in practice. Spillar (1993) suggested that a time delay might be detected as a feature in the autocorrelation function of a (radio frequency) signal. These are really the same manifestation of the effect since the autocorrelation is related to the power spectrum by a Fourier transform. Spillar also considered the possibility of detection of such features in the autocorrelation of a radio spectrum and concluded (by assuming that the Compton limit holds) that there is very little hope of observing the effect. Krauss & Small (1991) also discuss the idea but considered detection of variations in the total power (which requires a variable source, e.g. a pulsar) and concentrate on Galactic microlensing.

This chapter discusses a complete consideration of the problem of detection of microlensing time delays by radio autocorrelation in the context of current (but not yet completed) telescope and analysis technology with a detailed derivation of the expected noise properties of the autocorrelated signal.

7.2 The Compton Limit and Evidence for $T_b > 10^{12}$

One of the key questions in the study of gravitational microlensing by time delays is that of how much flux density one can expect to see from a very compact part of the sky. This is important because the differential time delay changes very rapidly across the sky thus smears the source over many lags.

The usual way to characterize the brightness of radio sources is using the brightness temperature which is the temperature (in the Rayleigh-Jeans limit) of a blackbody of equivalent brightness at a given frequency,

$$T_b = \frac{c^2}{2k\nu^2} I_\nu, \tag{7.1}$$

where I_ν is the specific intensity. For an isotropic emitter, we find

$$T_b = \frac{c^2}{2k\nu^2} \frac{S_\nu}{d\Omega}, \tag{7.2}$$

where S_ν is the total flux density and $d\Omega$ is the solid angle subtended by the source.

When a source emitting synchrotron radiation is very compact, the synchrotron photons can be inverse-Compton scattered by the same population of relativistic electrons that gives rise to the synchrotron radiation in the first place. The inverse-Compton scattering extracts energy from the electrons and shifts the photons to higher energies. If the energy density in the scattered photons is high enough, multiple inverse-Compton scattering will promote photons all the way up to gamma-ray energies thereby reducing the radio brightness temperature. The radio brightness temperature at which the multiple inverse-Compton scattered photons become the dominant emission mechanism is known as the Compton limit because a source which attempts to exceed it shifts most of its photons to higher energies. While the exact value of the Compton limit depends on the geometry of the source and the distribution of electron energies in the source, it is typically about $T_b \sim 10^{12}\,\mathrm{K}$ (Shu 1991). It is important to note that the intrinsic T_b may be Compton limited but other effects such as Doppler boosting can create an apparent $T_b > 10^{12}\,\mathrm{K}$. It is the apparent T_b (which is a measure of surface brightness on the sky) that is important for detection of microlensing time delays.

The Compton limit is subject to a strong observational challenge in recent observations of sources that exhibit intra-day variability. Wagner *et al.* (1996) report observations of a one such source, a BL Lac object, S5 0716+714, on which they performed simultaneous monitoring with radio, optical, UV, and X-ray telescopes. They find that the radio flux density changes on timescales of two hours at 5 and 8.4 GHz. These variations are correlated with changes in the optical flux leading to the conclusion that the mechanism that creates the variability is not an extrinsic effect like scintillation. Using the variability timescale to estimate the intrinsic size of the source, T_b at 5 GHz is estimated to be $10^{17\pm1}$ depending on assumptions about the unknown redshift to the source and H_0. The lower limit is given as $T_b \geq 1.4 \times 10^{16}$ ($H_0 = 50\,\mathrm{kms^{-1}Mpc^{-1}}$) in violation of the Compton limit by several orders of magnitude. The source might not be super-Compton if the explanation for this high apparent T_b lies (for example) in Doppler boosting. However, for the intrinsic T_b to be less than 10^{12} we require a doppler boosting factor of >100, larger than those observed by VLBI by a factor of ten but not outside the realm of possibility for the base of a sub-VLBI scale jet. Quirrenbach, *et al.* (1992) find that one-quarter of their flux limited sample of flat-spectrum sources exhibit intra-day variability at any given epoch with an amplitude ranging from ~2.5% to >20% with the variability implying T_b as high as 10^{19} K.

Interstellar scintillation could contribute to apparent flux density changes in extragalactic sources as well as create multiple ray paths that would introduce time delays like those due to gravitational lensing. While it should have very little effect at frequencies above 10 GHz, it is possible that weak scintillation is responsible for some of the short timescale flux density variation seen in extragalactic sources at these frequencies (Rickett 1990). Since scintillation is frequency dependent whereas lensing is achromatic, one can conduct an experiment at different frequencies. However, changes in source structure with frequency might make the interpretation of such an experiment difficult. A more powerful distinguishing feature is that delays due to scintillation change on a timescale of hours to days while microlensing delays change over periods of years since the time for the lens to cross its own Einstein ring is

$$t_{\text{cross}} = \frac{d_d \theta_E}{v_\perp} \tag{7.3}$$

where $v_\perp$ is the transverse velocity of the lens relative to the line of sight. For a solar mass lens in a galaxy at $z = 0.05$ with a transverse velocity of 600 km/s, this amounts to about 9 years.

7.3 Autocorrelation Signature of a Point Source

In order to examine a simple case, we consider the situation that would exist if a point source were imaged by a Schwarzschild potential. In this case, we have two images at the positions given in equation 1.12. The magnification of the Schwarzschild lens is given in equation 1.13. By substituting the image positions into this equation, we find that the magnification of the two images is

$$\mu_{\pm} = \frac{1}{4}\left[\frac{\tilde{\beta}}{\sqrt{\tilde{\beta}^2+4}} + \frac{\sqrt{\tilde{\beta}^2+4}}{\tilde{\beta}} \pm 2\right], \tag{7.4}$$

where $\tilde{\beta} = \frac{\beta}{\theta_E}$. Other quantities used below include:

$$|\mu_+| + |\mu_-| = \frac{\tilde{\beta}^2+2}{\tilde{\beta}\sqrt{\tilde{\beta}^2+4}} \tag{7.5}$$

$$|\mu_+\mu_-| = \frac{1}{\tilde{\beta}^2\left(\tilde{\beta}^2+4\right)} \tag{7.6}$$

We consider single polarization observations of a source of radio emission. Since will consider a phase coherent autocorrelation of the signal, we do not require that the total flux density of the source be variable at all and we will assume that it is not on the timescales of interest (~1 μs). Suppose that the electric field measured at the telescope is characterized by some source signal, $E(t)$, and that it arrives twice with some gravitational lensing induced time delay, Δ. Gravitational lensing also introduces two magnifications $\mu_{\pm}$. The measured signal at the telescope is

$$V(t) = \sqrt{\mu_+}E(t) + \sqrt{\mu_-}E(t+\Delta) + n(t), \tag{7.7}$$

where $n(t)$ is the noise. The rotation of the polarization vector between the two images of the source does not affect this result since the rotation is of order the deflection angle (Bertschinger 1996).

The autocorrelation of $V(t)$ is

$$\begin{aligned} R(\tau) &= \langle V(t)V(t-\tau)\rangle & (7.8)\\ &= \left\langle\left(\sqrt{|\mu_+|}E(t) + \sqrt{|\mu_-|}E(t+\Delta) + n(t)\right)\right. & (7.9)\\ &\quad \left.\times\left(\sqrt{|\mu_+|}E(t-\tau) + \sqrt{|\mu_-|}E(t+\Delta-\tau) + n(t-\tau)\right)\right\rangle & \\ &= \left(|\mu_+| + |\mu_-|\right)\langle E(t)E(t-\tau)\rangle + \langle n(t)n(t-\tau)\rangle & (7.10)\\ &\quad + \sqrt{|\mu_+\mu_-|}\left[\langle E(t)E(t+\Delta-\tau)\rangle + \langle E(t+\Delta)E(t-\tau)\rangle\right], & \end{aligned}$$

where $E(t)$ and $n(t)$ have been assumed to be uncorrelated so that terms of the form

$\langle E(t)n(t-\tau)\rangle$ are zero for all τ. If $E(t)$ and $n(t)$ are incoherent, the first and second terms in equation 7.10 vanish for all $\tau \neq 0$. At $\tau = 0$, these terms correspond to the total power received at the antenna, $(|\mu_+| + |\mu_-|)\langle E^2\rangle + \langle n^2\rangle$. The last two terms give peaks in the autocorrelation spectrum at $\tau = \pm\Delta$ with amplitude $\sqrt{|\mu_+\mu_-|}\langle E^2\rangle$. These peaks are the signature of a time delay in the data. The autocorrelation spectrum derived in equation 7.10 is illustrated in Figure 7.1. The autocorrelation spectrum that we measure with a real instrument is the convolution of the ideal spectrum described above with the autocorrelation of the impulse response function of the filter which defines the observing bandpass. As an example, the autocorrelation of the impulse response function of a 1 GHz bandpass filter formed by a high-pass RC filter and a low-pass eighth-order butterworth filter is shown in Figure 7.2. Such a filter has the sharp cutoff necessary to avoid aliasing when the signal is sampled at the Nyquist rate for use in a digital correlator. Though the autocorrelation of the impulse response function appears relatively well constrained near zero lag, note that the convolution of it with the total power (noise + signal) spike at $\tau = 0$ will create a very large signal over the τ's of interest. Therefore, precise knowledge of this function will be crucial to making a detection in a practical experiment.

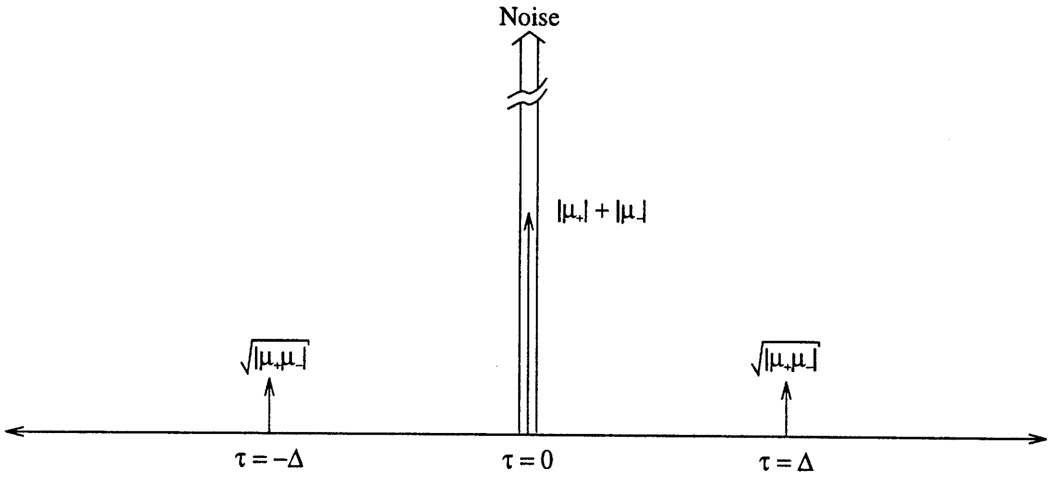

FIGURE 7.1: The correlation spectrum of an ideal point source lensed into two images with time delay Δ. There are two features at $\tau = 0$, which represent the total power due to noise and due to the source. The features at $\tau = \pm\Delta$ are the signature of the time delay.

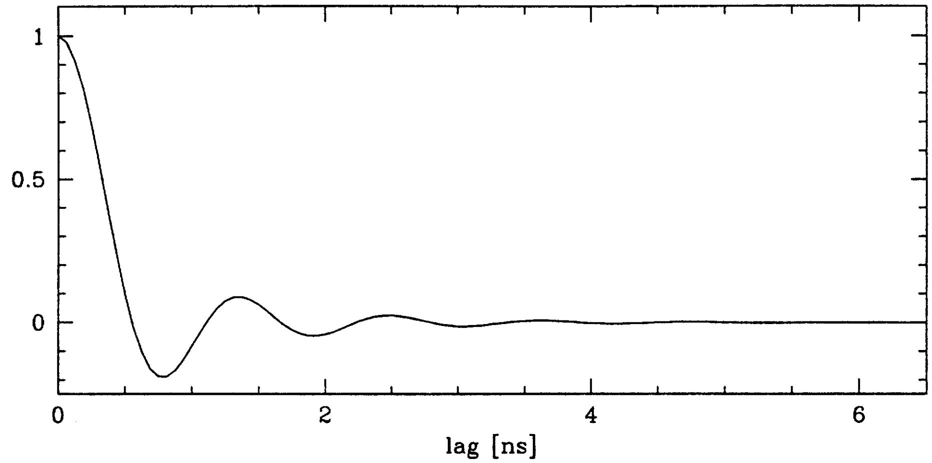

FIGURE 7.2: The autocorrelation of the impulse response function of a sample 1 GHz bandpass filter formed by a high-pass RC filter and a low-pass eighth order butterworth filter.

7.4 Noise in the Autocorrelation Spectrum

In order to calculate the noise in the autocorrelation spectrum we consider the autocorrelation at some fixed lag $-\rho$:

$$R(-\rho) = \langle V(t)V(t+\rho)\rangle \tag{7.11}$$

to find the noise in $R(-\rho)$ we need to find its power spectrum which we do by first finding the autocorrelation and then Fourier transforming. Starting with the autocorrelation of the output of the autocorrelator,

$$\phi_d(\tau) \ = \ \langle V(t)V(t+\rho)V(t-\tau)V(t+\rho-\tau)\rangle\,, \tag{7.12}$$

and using

$$\langle wxyz\rangle = \langle wx\rangle\langle yz\rangle + \langle wy\rangle\langle xz\rangle + \langle wz\rangle\langle xy\rangle \tag{7.13}$$

which holds if w, x, y, and z are jointly gaussian zero-mean random variables, we find

$$\begin{aligned}\phi_d(\tau) \ = \ & \langle V(t)V(t+\rho)\rangle\langle V(t-\tau)V(t+\rho-\tau)\rangle \qquad (7.14)\\ & + \langle V(t)V(t-\tau)\rangle\langle V(t+\rho)V(t+\rho-\tau)\rangle \\ & + \langle V(t)V(t+\rho-\tau)\rangle\langle V(t+\rho)V(t-\tau)\rangle\,.\end{aligned}$$

Because $V(t)$ is stationary, the first term in equation 7.14 equals $\langle V(t)V(t+\rho)\rangle^2$ and the second term is $\langle V(t)V(t-\tau)\rangle^2$. After substituting the value of $V(t)$, we have

$$\begin{aligned}
\phi_d(\tau) \;=\; & \Big\langle (|\mu_+| + |\mu_-|)E(t)E(t+\rho) + n(t)n(t+\rho) \\
& \quad + \sqrt{|\mu_+\mu_-|}\,[E(t)E(t+\Delta+\rho) + E(t)E(t+\Delta-\rho)] \Big\rangle^2 \\
& + \Big\langle (|\mu_+| + |\mu_-|)E(t)E(t-\tau) + n(t)n(t-\tau) \\
& \quad + \sqrt{|\mu_+\mu_-|}\,[E(t)E(t+\Delta+\tau) + E(t)E(t+\Delta-\tau)] \Big\rangle^2 \\
& + \Big\langle (|\mu_+| + |\mu_-|)E(t)E(t+\rho-\tau) + n(t)n(t+\rho-\tau) \\
& \quad + \sqrt{|\mu_+\mu_-|}\,[E(t)E(t+\Delta+\rho-\tau) + E(t)E(t-\Delta+\rho-\tau)] \Big\rangle \\
& \times \Big\langle (|\mu_+| + |\mu_-|)E(t)E(t-\rho-\tau) + n(t)n(t-\rho-\tau) \\
& \quad + \sqrt{|\mu_+\mu_-|}\,[E(t)E(t+\Delta-\rho-\tau) + E(t)E(t+\Delta+\rho+\tau)] \Big\rangle .
\end{aligned} \tag{7.15}$$

In order to check equation 7.15, first we take the case of a total power radiometer where there is no gravitational lens at all (i.e. $\tau = \rho = \mu_- = 0$ and $\mu_+ = 1$). For this case, we have

$$\phi_d(\tau) = \Big\langle V^2(t) \Big\rangle^2 + 2\Big\langle V(t)V(t-\tau) \Big\rangle^2 = \phi_{\mathrm{v}}^2(0) + 2\phi_{\mathrm{v}}^2(\tau). \tag{7.16}$$

The first term in equation 7.16 is a constant in the autocorrelation of the autocorrelator output and therefore a delta function at zero frequency in the Fourier transform of that output. It represents the D.C. term in the output. The second term gives the A.C. part and can be used to derive the noise expected in measurements from a total power radiometer. Next, we consider the possibility of looking for an autocorrelation at finite $\rho \neq 0$ when, in fact, none exists (i.e. $\Delta = \mu_- = 0$ and $\mu_+ = 1$). For this situation, we calculate

$$\begin{aligned}
\phi_d(\tau) \;=\; & \Big\langle V(t)V(t+\rho) \Big\rangle^2 + \Big\langle V(t)V(t-\tau) \Big\rangle^2 \\
& + \Big\langle V(t)V(t+\rho-\tau) \Big\rangle \Big\langle V(t)V(t-\rho-\tau) \Big\rangle
\end{aligned} \tag{7.17}$$

$$= \phi_{\mathrm{v}}^2(-\rho) + \phi_{\mathrm{v}}^2(\tau) + \phi_{\mathrm{v}}(-\rho+\tau)\phi_{\mathrm{v}}(\rho+\tau) \tag{7.18}$$

Since we have assumed that there is no delay (i.e. $\phi_{\mathrm{v}}(x) = 0$ for all $x \neq 0$) the constant part of $\phi_d(\tau)$ is zero and the D.C. term in the output of the autocorrelator is zero for all

$\rho \neq 0$. Since both $E(t)$ and $n(t)$ are gaussian white noise,

$$\phi_{\mathrm{v}}^2(\tau) + \phi_{\mathrm{v}}(-\rho+\tau) \times \phi_{\mathrm{v}}(\rho+\tau) = 2\phi_{\mathrm{v}}^2(\tau). \tag{7.19}$$

and we recover the noise expected from a total power radiometer with no input signal.

Finally, we consider the case where there is some gravitational time delay, $\Delta \neq 0$. For detection of the time delay, we operate the correlator at $\rho = \pm\Delta$ and find

$$\begin{aligned}
\phi_d(\tau) \;=\;& \Big\langle \left(|\mu_+| + |\mu_-|\right) E(t)E(t+\rho) + n(t)n(t+\rho) \\
&\quad + \sqrt{|\mu_+\mu_-|}(E(t)E(t+2\rho) + E(t)E(t)\Big\rangle^2 \\
&+ \Big\langle \left(|\mu_+| + |\mu_-|\right) E(t)E(t-\tau) + n(t)n(t-\tau) \\
&\quad + \sqrt{|\mu_+\mu_-|}(E(t)E(t+\rho+\tau) + E(t)E(t+\rho-\tau))\Big\rangle^2 \\
&+ \Big\langle \left(|\mu_+| + |\mu_-|\right) E(t)E(t+\rho-\tau) + n(t)n(t+\rho-\tau) \\
&\quad + \sqrt{|\mu_+\mu_-|}(E(t)E(t+2\rho-\tau) + E(t)E(t-\tau))\Big\rangle \\
&\times \Big\langle \sqrt{|\mu_+| + |\mu_-|}E(t)E(t-\rho-\tau) + n(t)n(t-\rho-\tau) \\
&\quad + \sqrt{|\mu_+\mu_-|}(E(t)E(t-\tau) + E(t)E(t+2\rho+\tau))\Big\rangle
\end{aligned} \tag{7.20}$$

$$\begin{aligned}
=\;& \left(|\mu_+| + |\mu_-|\right)^2 \phi_{\mathrm{e}}^2(-\rho) + \phi_{\mathrm{n}}^2(-\rho) + |\mu_+\mu_-| \left(\phi_{\mathrm{e}}(0) + \phi_{\mathrm{e}}(-2\rho)\right)^2 \\
&+ \left(|\mu_+| + |\mu_-|\right)^2 \phi_{\mathrm{e}}^2(\tau) + \phi_{\mathrm{n}}^2(\tau) + |\mu_+\mu_-| \left(\phi_{\mathrm{e}}(-\rho-\tau) + \phi_{\mathrm{e}}(\tau-\rho)\right)^2 \\
&+ \left[\left(|\mu_+| + |\mu_-|\right) \phi_{\mathrm{e}}(\tau-\rho) + \phi_{\mathrm{n}}(\tau-\rho) + \sqrt{|\mu_+\mu_-|} \left(\phi_{\mathrm{e}}(\tau-2\rho) + \phi_{\mathrm{e}}(\tau)\right)\right] \\
&\times \left[\left(|\mu_+| + |\mu_-|\right) \phi_{\mathrm{e}}(\tau+\rho) + \phi_{\mathrm{n}}(\tau+\rho) + \sqrt{|\mu_+\mu_-|} \left(\phi_{\mathrm{e}}(\tau) + \phi_{\mathrm{e}}(-\tau-2\rho)\right)\right]
\end{aligned} \tag{7.21}$$

The only non-zero constant term in equation 7.21 is $|\mu_+\mu_-|\,\phi_{\mathrm{e}}^2(0)$ which (after Fourier transforming) is the D.C. component of the autocorrelator output as expected from equation 7.10. If $\langle n^2(t)\rangle \gg \langle E^2(t)\rangle$, the A.C. part the autocorrelator output is

$$\phi_{\mathrm{n}}^2(\tau) + \phi_{\mathrm{n}}(\tau-\rho) \times \phi_{\mathrm{n}}(\tau+\rho) = 2\phi_{\mathrm{n}}^2(\tau) \tag{7.22}$$

which recovers the same noise properties of a simple total power radiometer without any additional factors.

7.5 Simulations of Extended Sources

If the source is incoherent, we can simulate the response of the autocorrelation experiment by dividing the source into pixels, treating each pixel as an independent source, and summing the effect over all pixels. This approach works as long as the pixels are small enough that there isn't a large time delay or magnification gradient across a single pixel. The most notable failure is the case where the source is directly behind the lens. This case will be handled analytically in the next section.

We have implemented software to simulate the autocorrelation spectrum due to an arbitrary extended source lensed by a Schwarzschild potential. A likely geometry for observing microlensing time delays is a background source (e.g. a BL Lac) at large redshift and a microlens in a galaxy somewhere along the line of sight. In order to facilitate comparison between the various lensing scenarios presented in this and the following sections, we assume a standard lensing geometry with the following parameters:

$$\begin{aligned} z_l &= 0.05 \\ z_s &= 1.00 \\ q_0 &= 0.5 \\ H_0 &= 80\,\mathrm{km\,s^{-1}\,Mpc^{-1}}. \end{aligned} \tag{7.23}$$

The results computed by our software for the case of a 100 mJy uniform disk source of radius 0.5, 1.0, and 2.0 μas located at a distance $\beta = \frac{\theta_E}{2}$ from a $1\,\mathrm{M}_\odot$ lens are shown in Figure 7.3. As the source gets larger, the flux is spread over more lags and the autocorrelation peaks become asymmetric since the magnification goes up near the lens. Also note that the structure of the source (taken in rings centered on the lens and multiplied by the magnification due to the lens) is encoded in the autocorrelation spectra. For the case of many microlenses, the images are spread into many microimages (Paczynski 1986a) and correspondingly many gravitational lens time delays. This spreads out the available flux in time delay space and makes it difficult to detect the microlensing delays except during periods when the gravitational lens magnification is very large.

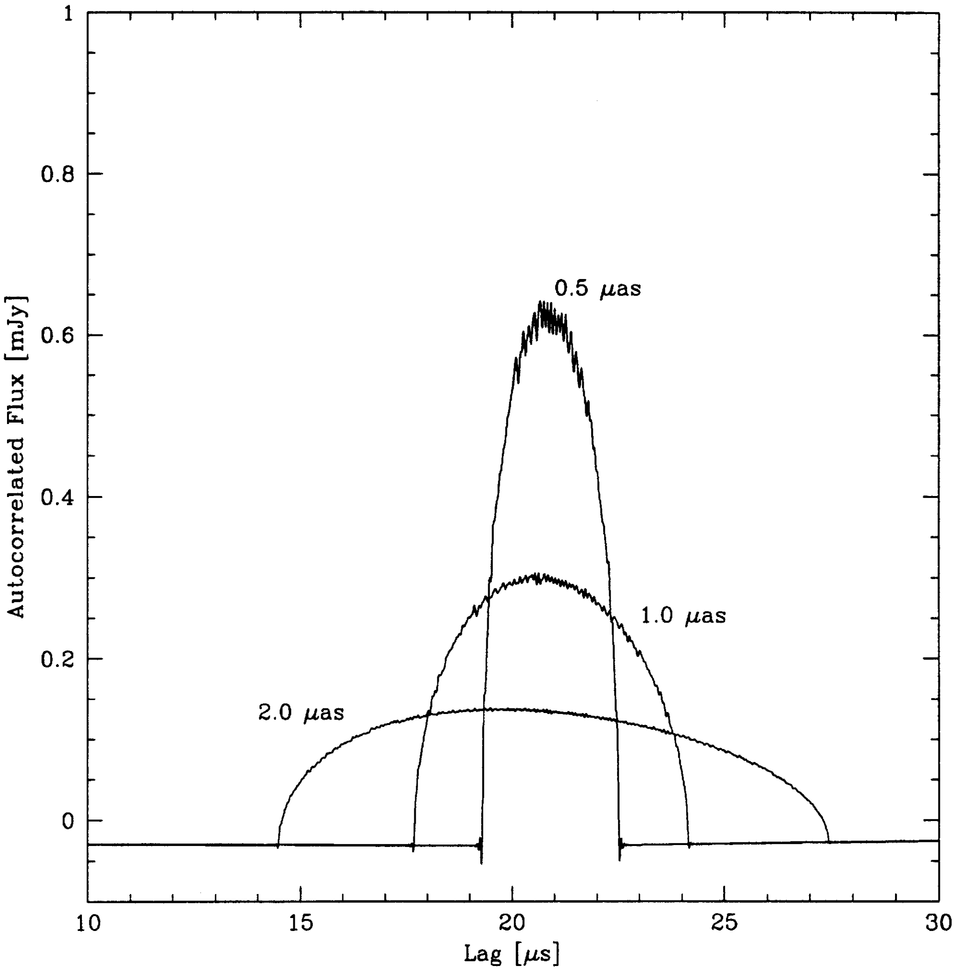

FIGURE 7.3: Simulated autocorrelation spectra for several disk sources of total flux density 100 mJy placed at $\theta_E/2$. Note that the larger sources show an increase in magnification near the lens (i.e. at small lags). The roughness of the curves is due to the pixelization of the source.

7.6 Microlenses in Front of Extended Sources

For a lens in front of a uniform extended source, we can find the autocorrelation signal analytically by integrating the area weighted by the surface brightness and the expected amplitude of the autocorrelation signal from equation 7.10 to obtain

$$\int T_b \theta_E^2 \frac{2k\nu^2}{c^2} |\mu_+ \mu_-| \, 2\pi\tilde{\beta} \, d\tilde{\beta} = \int T_b \theta_E^2 \frac{2k\nu^2}{c^2} \times \frac{1}{\sqrt{\tilde{\beta}^2 \left(\tilde{\beta}^2 + 4\right)}} \times 2\pi\tilde{\beta} \, d\tilde{\beta} \tag{7.24}$$
$$= \frac{4\pi T_b \theta_E^2 k\nu^2}{c^2} \ln \left[\tilde{\beta} + \sqrt{\tilde{\beta}^2 + 4}\right].$$

This integral is then evaluated over the range of $\tilde{\beta}$'s that contribute to a particular lag bin. The expected autocorrelation spectrum (before convolution by the autocorrelation of the impulse response function) for a 1 $\mathrm{M}_\odot$ lens under the conditions given in equation 7.23 is displayed in Figure 7.4. The area of the source that is visible to the autocorrelation technique consists of an annulus centered at the lens with the small $\tilde{\beta}$ limit set by how well the bandpass filter is known (see section 7.7) and the large $\tilde{\beta}$ limit determined by either occultation of the second image by the lens itself or failure of the weak-field approximation in equation 1.1. For the occultation case, we assume that the lens has the same density as the Sun and calculate the source position, $\tilde{\beta}$, that results in the image closest to the lens just grazing its surface. Starting from the lens equation for the Schwarzschild potential (equation 1.11) and requiring that the radius of the lensing object, $R_L = d_d\theta$, we have

$$\tilde{\beta}_{\max} = \left| \frac{\theta}{\theta_E} - \frac{\theta_E}{\theta} \right| = \left| \frac{R_L}{d_d\theta_E} - \frac{d_d\theta_E}{R_L} \right|. \tag{7.25}$$

where the assumption of Solar mass density yields $R_L = \sqrt[3]{\frac{M_L}{\mathrm{M}_\odot}}\,\mathrm{R}_\odot$. When the weak-field assumption is the problem, we can find the θ for which the terms which are second order in $\frac{GM}{c^2b}$ that were ignored in the derivation of the weak-field limit begin to become important. If we would like the second order terms to be less than 1% of the leading term, we have

$$\frac{GM}{c^2b} < \frac{1}{100} \tag{7.26}$$

which gives the limit on the impact parameter

$$b = d_d\theta \geq 50R_s \tag{7.27}$$

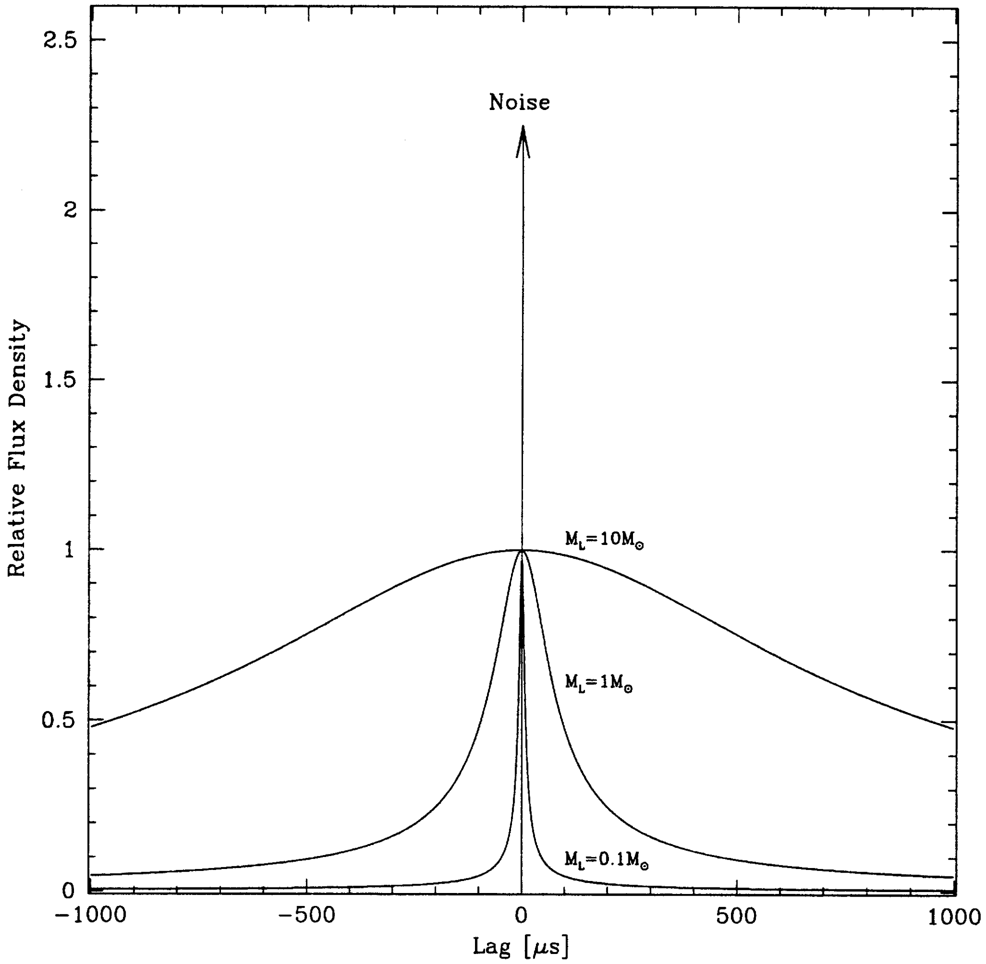

FIGURE 7.4: Expected autocorrelation spectrum (before convolution with the autocorrelation of the impulse response function) of a uniform surface brightness source behind lenses of mass 0.1, 1.0, and 10.0 $M_\odot$.

where $R_s = \frac{2GM}{c^2}$ is the Schwarzschild radius of the lensing mass. Inserting the limiting case into the lensing equation as above yields:

$$\tilde{\beta}_{\max} = \left|\frac{50R_s}{d_d\theta_E} - \frac{d_d\theta_e}{50R_s}\right| \tag{7.28}$$

The $\tilde{\beta}_{\max}$ calculated above typically occur at large lags and do not interfere in the calculations described in the next section. However, if one looks at low density lensing masses, lensing masses surrounded by an ionized plasma, or at very large lags, the proximity of the second image to the lens and the resulting $\tilde{\beta}_{\max}$ can become important.

7.7 Detectability Limits

Detection of microlensing time delays will require an experiment that minimizes the introduction of false time delay signatures in the signal, has a wide bandwidth, good electronics to minimize the noise, and has a stable bandpass filter for accurate subtraction of the autocorrelation of the impulse response function. As an example of a modern large radio telescope, we consider the Green Bank Telescope (GBT) which is presently under construction in Green Bank, West Virginia. The GBT will be a 100 m telescope with an off-axis feed system that results in a completely unblocked aperture. The unblocked aperture avoids the introduction of support structures in the ray path that might introduce reflections which mimic lensing time delays. Autocorrelators implemented in hardware have made possible the creation of large bandwidth autocorrelation engines (e.g. the GBT's autocorrelation spectrometer (see Heiles, 1993); we will assume an observing bandwidth of 1 GHz. For the following calculations we assume, for example, the GBT operating at 15 GHz where the system temperature is expected to be ∼30 K and the expected aperture efficiency is about 0.65 (Norrod 1995).

Since the time delay signal is contaminated by the noise signal at $\tau = 0$ convolved with the autocorrelation of the impulse response function of the bandpass filter, it is very important that the bandpass be well known and stable. The shape of the convolving function can be well measured by observations of empty sky, which may have to be repeated as the function changes which would reduce the observational efficiency. In the following, we will assume that the convolving function is well known. Reliable detections will also require that the telescope and electronics systems be free of reflections that introduce spurious delays on the timescales of interest. Such delays and their variability can be characterized by observations of empty sky.

Using the software described in section 7.5 we have calculated the expected observation time required to make a single-lag 5σ detection of a 100 mJy disk source using the GBT with autocorrelation lags 31.25 ns wide. This is accomplished by simulating the autocorrelation spectrum of the source (see for instance Figure 7.3), finding the lag bin which exhibits the maximum signal and then calculating the integration time necessary to detect that signal at a level of five times the thermal noise. Figure 7.5 displays contours of observing time (in hours) needed to make a detection for a variety of source positions and sizes and for lens masses $1\,\mathrm{M}_\odot$ and $0.1\,\mathrm{M}_\odot$.

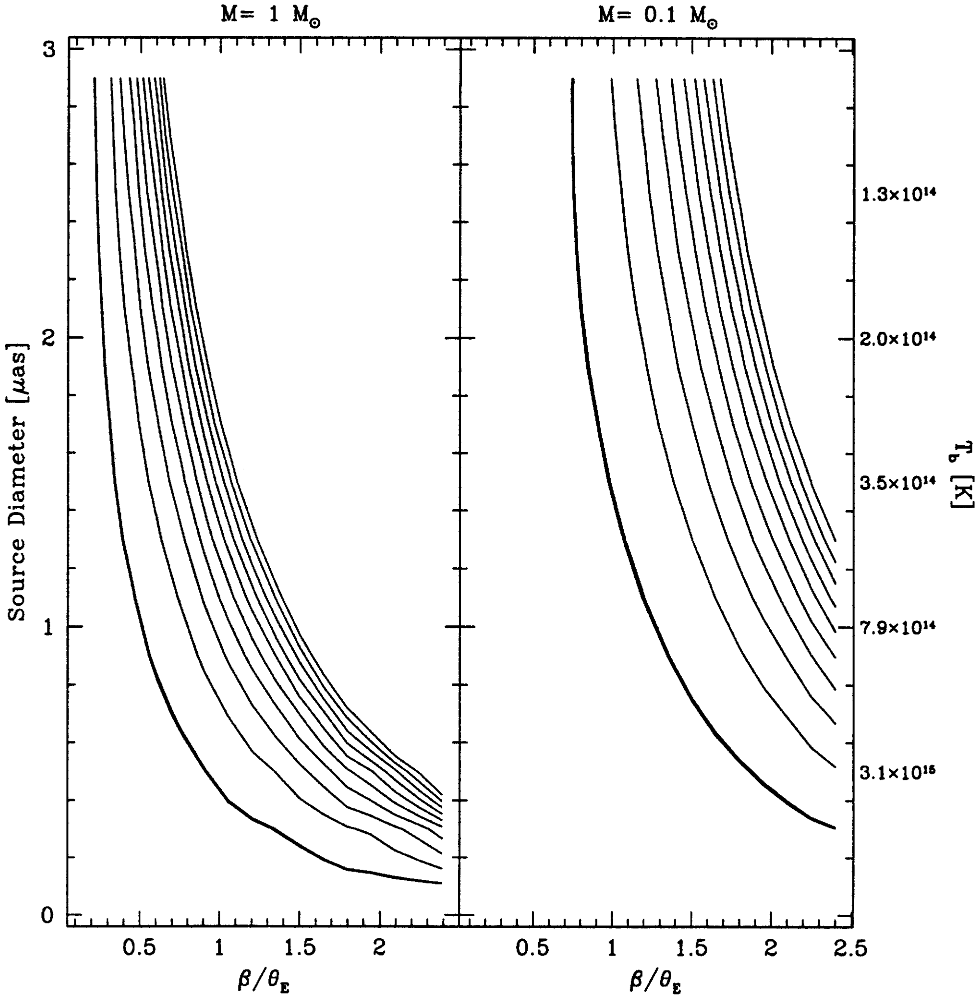

FIGURE 7.5: 5σ detection times for a 100 mJy disk source for a variety of source angular sizes and positions. Lens masses are 1.0 $\mathrm{M}_\odot$ (left) and 0.1 $\mathrm{M}_\odot$ (right) and the geometric parameters are those given in equation 7.23. The Einstein angles are 6.6 and 2.1 μas respectively and the contours begin at one hour (thick line) and continue in two hour increments.

We have also calculated the observation time to make a 5σ detection of a uniform source of brightness temperature T_b located directly behind a lens of mass M_L by using the analytic expression in section 7.6. We assume the geometric parameters in equation 7.23 and set the inner limit of $\tilde{\beta}$ such that the minimum delay is at $1\,\mu$s. Figure 7.6 displays the 5σ detection time for a single lag bin $1\,\mu$s wide. Note that increasing the lens mass beyond $0.1\,\mathrm{M}_\odot$ makes little difference for this choice of lag bin since the amount of area on the

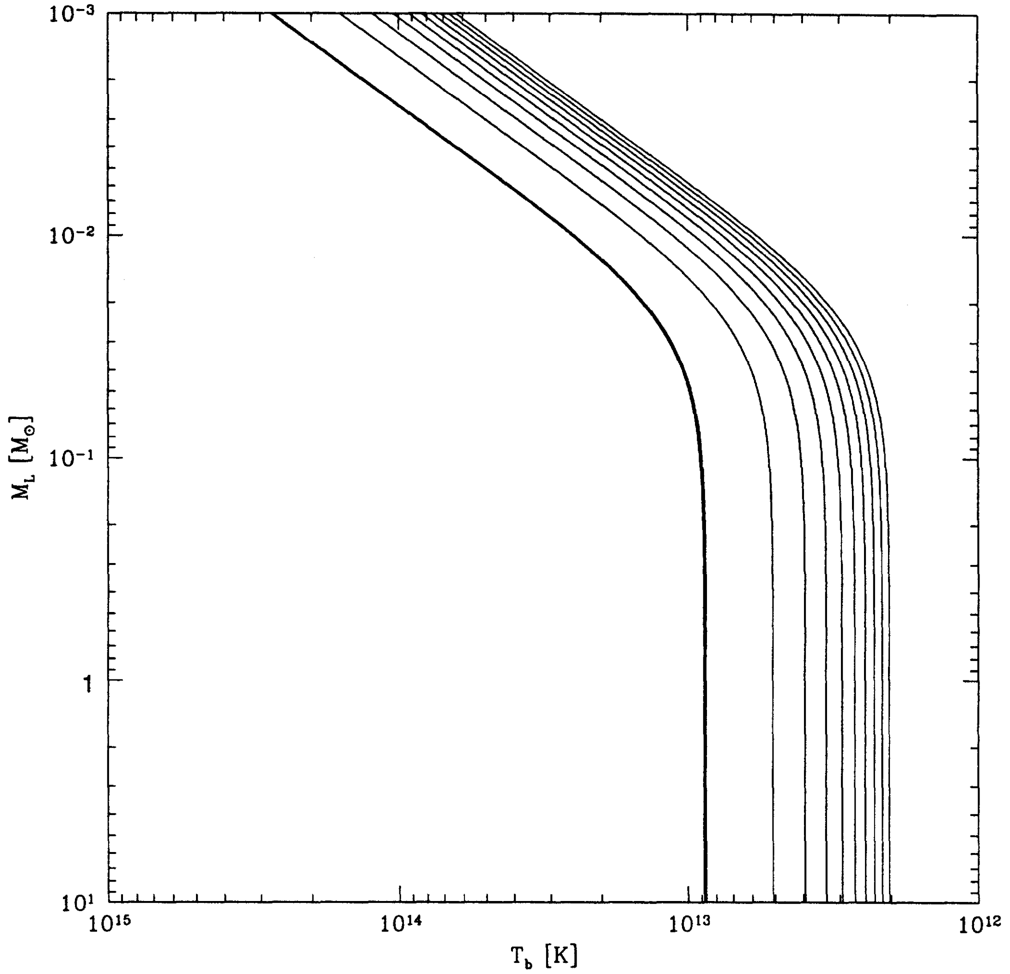

FIGURE 7.6: 5σ single-lag detection times for a uniform source of brightness temperature T_b located directly behind a microlens. Parameters are those given in equation 7.23, the lag bin is from 1–2 μs, and the contours start at one hour (thick line) and continue in two hour increments.

source that contributes to a given lag goes down (since the delay gradient goes up) at the same time that the magnification goes up.

7.8 Conclusion

We have made a complete analysis of an experiment to measure microlensing time delays by coherent autocorrelation of a radio signal for the case of a single microlens. After a detailed derivation of the noise properties of the signal, we have shown that one can expect to detect radio cores (if they have large apparent brightness temperatures) using microlenses in an intervening galaxy and a large radio telescope. Uniform surface brightness sources with lenses in front of them are detectable at smaller but still super-Compton surface brightnesses. Therefore, the best targets for a microlensing time delay search are bright intra-day variable objects with microlenses in galaxies near the line of sight. Detection of time delays in such objects would demonstrate the presence of high brightness temperatures in the source, compact objects in the lens, and provide some information on the structure of the source and the transverse velocity of the lens.

Chapter 8

Conclusion

We have described monitoring programs at 8 and 15 GHz that both fail to detect clear evidence for variability in the gravitational lens MG 0414+0534. In the course of the work, we have developed techniques for accurate flux density scale calibration and discovered that deconvolution errors in simple sources can result in flux density errors of as much as 20% in certain cases. We have developed a technique for the measurement and correction of these errors in simple sources and demonstrated its application to our data. We have shown one should be able to detect microlensing time delays by phase coherent autocorrelation of a radio signal given a large radio-telescope and sources with sufficient brightness temperature.

8.1 15 GHz Monitoring Program

The 15 GHz monitoring program consists of 63 observations made over a period of 183 days. It is plagued by problems with poor weather and low elevation observing which lead to difficulty with flux density calibration due to pointing errors caused by wind and due to changing atmospheric absorption by water vapor. After exclusion of observations that are suspected to be strongly affected by such systematic errors the remaining data (only 35 observations) have an RMS variability of 3.3%, 3.5%, 3.9%, and 3.7% for the A1, A2, B, and C images respectively. Structure function analysis shows that of this, 3.4% is correlated at zero lag and is thus associated with flux calibration errors.

The RMS variability in the flux ratios is consistent with that measured from simulated data so there is no evidence for variablity in the source. Various time delay analysis

---

[0] chapter8.tex v1.4 1996/08/07

techniques including the Press, Rybicki, Hewitt χ^2 (Press *et al.* 1992c) and the Discrete Correlation Function (Edelson & Krolik 1988) fail to detect any convincing signature of a time delay in the data.

8.2 8 GHz Monitoring Program

The 8 GHz program was designed avoid the atmospheric problems of the 15 GHz program as well as work at a frequency where the source is brighter and the instrument more sensitive. It takes advantage of new reduction techniques described below to extend the temporal coverage and thereby increase the signal-to-noise ratio for detection of time delays. The program consists of a total of 82 observations spread over ~300 days of which all but five are included in the analysis. After application of a correction for deconvolution errors, the total RMS in the lightcurves is 1.4%, 1.5%, and 1.7% for the A1+A2, B, and C images respectively (see Table 6.9 for more detail).

The non-parametric analysis of Pelt, *et al.* (1996) was applied to the data and yielded no convincing time delay information when compared with simulations of the observation. Examination of the flux density ratios yeilds the detection of a positive correlation between the A:B and C:B ratios. This correlation also exists in simulations which contain no variability but is stronger in the real data than in the simulations. Simulations which contain more of the observational details will be necessary to determine if this is indicative of low-level variability.

8.3 Data Analysis Techniques

Flux calibration for the 8 GHz program was performed using a model derived from a full-synthesis observation of the flux calibrator. Estimates of the flux calibration error are 2.6%, 0.87%, and 0.67% for the A, B, and C-arrays respectively. To our knowledge, this is the most stable 8 GHz flux calibration that has been demonstrated with this instrument to date.

We improved the measurement of flux densities in the data with a combination of two new techniques. First, CLEAN was restricted to place clean components in very small boxes at the positions of the images. This allowed the precise positions of images measured in A-array data to be used to assist in the deconvolution of much lower resolution C-array data. Second, total flux densities were measured by summing the clean components which appeared in each CLEAN box. This approach provides much more reliable measurements than fitting gaussians in the image especially when the resolution is comparable to the image separation.

For both monitoring programs, simulated data (with noise) were prepared and subjected to the same analysis procedures as the real data. In the 15 GHz data, we detect some biases due to deconvolution errors, but the variance in our simulations is of order the bias. In simulations of the 8 GHz program, the variance was much smaller and large (up to 20%) deconvolution errors were detected. The average error was used to create correction factors that were applied to the real data. Application of these factors reduced the RMS variability in the lightcurves by factors of 1.2, 1.5, and 2.8 for the A1+A2, B, and C images respectively.

8.4 Detectability of Time Delays

Hewitt, Chen, and Messier (1995) demonstrate the capability of a particular technique (the Press, Rybicki, Hewitt-χ^2) to extract time delays from simulated data when the signal-to-noise ratio for the variability on the time scale of the time delay is small. Their simulations show that monitoring programs with 100 observations are capable of making time delay measurements with < 10% error even when the signal-to-noise ratio is $\sim$2.

Hughes, *et al.* (1992) find that structure functions of most radio sources are well fit by power laws of unit index and that the median timescale for variability is 2.24 years. If one assumes a structure function of unit index (as defined in Section 4.4) and a characteristic timescale of τ_0 at which the structure function turns over, then we have

$$V(\tau) = \begin{cases} \sigma^2 \left(\frac{\tau}{\tau_0}\right) & \text{if } \tau < \tau_0 \\ \sigma^2 & \text{if } \tau > \tau_0 \end{cases} \tag{8.1}$$

where the long term RMS variability is σ. For a monitoring experiment on gravitational lens system with expected delay τ_d, we might require that the RMS variability at the lens delay, $\sqrt{V(\tau_d)}$, be a factor of α larger than the noise in the measurements, σ_n. This gives a lower limit on the detectable delay of

$$\min \tau_d = \left(\frac{\alpha \sigma_n}{\sigma}\right)^2 \tau_0. \tag{8.2}$$

Note that the minimum detectable delay depends on the square of α and σ_n as well as the inverse square of σ. This means that there is an important advantage for time delay extraction techniques which can operate with small α and for large σ in the source. It also shows the critical importance of minimizing the observational errors using techniques like those developed here.

If one assumes the τ_0 given above (2.2 years), $\sigma = 40\%$, $\alpha = 2$ (for <10% error in measuring the time delay) then the minimum detectable delays for the observational error achieved in this work are 2.4 and 22 days for the 8 and 15 GHz bands respectively. The difference here is entirely due to the measurement errors. It is possible that an increase in σ at higher frequencies might partially compensate for the associated increase in the measurement error. Aller, *et al.* (1992) report that 97% of the BL Lacs and QSOs in their sample exhibit at least 10% variability. If we still require $\alpha = 2$, then we find that the minimum detectable delays are 40 and 350 days for 8 and 15 GHz respectively. The details of observational and reduction procedure that minimize σ_n and α are therefore very important to the planning of time delay observations. Measurement of τ_0 and σ from long term monitoring experiments can also be used to understand the probability of success for a time delay detection. Even with no long term monitoring data about the source in a particular lens, one could use long term monitoring data from sources with similar identifications to find the statistical distribution of τ_0 and σ.

8.5 Prospects for Detection of Microlensing Time Delays

We have made a detailed analysis of an experiment to use phase coherent autocorrelation of a radio signal to detect microlensing time delays. Such delays should be detectable for high brightness temperature background sources with microlenses located in a galaxy along the line of sight. Detection of these delays would demonstrate the existence of high brightness temperature sources, compact masses in another galaxy or galaxy halo, and provide limited information on the structure of the source and the transverse velocity of the microlens.

8.6 Future Work

The soon to be completed Green Bank Telescope will provide an ideal instrument for the detection of microlensing time delays. It has a large unblocked aperture which gives high sensitivity as well as no obstructions in the ray path which might introduce spurious time delays. It will be equipped with a 900 MHz bandwidth spectrometer which could be put to use as an autocorrelation engine for such an experiment. The major remaining uncertainty is the effect of bandpass instability on the autocorrelation spectrum and the amount of observing time that will be used to calibrate such instabilities.

It is possible that MG0414 is a variable source and that our monitoring programs happened to observe it during a period of quiescence. The lack of a clear detection of variability is thus discouraging for future monitoring efforts but should not exclude them entirely.

Given the measured deconvolution errors in the simulated monitoring data, it is clear that deconvolution errors can be a critical problem for accurate flux density or even flux density ratio observations particularly in the face of changing uv-sampling. The success of the deconvolution error correction factors indicates that these errors are readily reproduced and corrected. The techniques developed here can be used directly to improve the accuracy and temporal baseline for other existing or proposed VLA based monitoring programs of objects with an easily modelled radio morphology thus resulting in a higher signal-to-noise ratio for the detection of time delays.

Given the significance of deconvolution errors demonstrated in this thesis, an approach for further research will be to fit model parameters to the uv-data directly. One could, for instance, fit adjustable fluxes with fixed image positions to the amplitudes of the visibilities and avoid using the phases altogether. Since this works with the data where the errors are well known, one can expect to derive proper χ^2 goodness of fit measures, achieve still more reliable flux density measurements, and make reasonable estimates of the error in the fit parameters.

Appendix A

AIPS Run File for U-Band Data Reduction

A.1 Introduction

This appendix contains the AIPS "run file" that was used to process the 15 GHz data (see chapter 3). The language used here is an interpreted subset of FORTRAN/66 that is (poorly) documented in "The AIPS Cookbook" distributed by NRAO and also (more thoroughly) in help files distributed with AIPS itself. The procedures in the file were designed to run in AIPS version `15APR92` with custom enhancements that were written by Samuel R. Conner (SRC) and added to the local M.I.T. installation of AIPS.

Each procedure begins with `proc <procedure name>` and ends with `return;finish`, comments begin with `$`, and all commands can be abbreviated by dropping characters at the end as long as the result remains unique (thus `return;finish` is usually abbreviated `ret;fin`). There are few comments in the code because they take up memory in the AIPS interpreter and the code almost fills the available space.

The major component procedures are:

`grind(N)` uses SRC's `readna` to read the Nth line in a list of observations to process, uses `loaduv` corresponding UV data, applys extra flagging to a few selected datasets, uses `calit` to find and apply the flux calibration and then enters a self-calibration loop which maps and phase-only self-calibrates the data until the fractional change in the image B flux density is less than 0.1%. Also saves the final reduced data and maps to disk.

`loaduv` loads a selected UV dataset from FITS format on and external disk and saves it on the AIPS disk `wdisk`.

`calit` removes the CL table that comes with the data (since some of the data have new CL table formats that are not compatible with this version of AIPS, then uses a model of 3C 48 to find the flux calibration and therefore the flux density of the phase calibrator (using the observation of the phase calibrator that occurs closest in time to the observation of 3C 48), and then finds phase and amplitude solutions for the phase calibrator. These are applied to the data and the data are separated into single source data files.

`obox` uses `maxfit` and an approximate starting location to find the peak of image B. Known offsets for the other components are then used to set small boxes at the locations of all image components.

`boxflux` uses `ccmrg` to reduce the number of clean components and then sums the clean components that appear in the box centered on each image. This is the central flux density measurement procedure.

`getnoise` uses `imstat` to calculate the RMS image noise in a large box to the south of the images of MG0414.

`setmx` sets all parameters of the MX task to standard values. This is used as the base setup for every call to MX.

`setpcal` sets all parameters of CALIB for use in phase-only self-calibration loop.

A.2 AIPS Run file – "`proc.run`"

```
$ CBM - new calibration with TIMERANG set for GETJY
$ $Id: proc.run,v 2.40 1996/05/09 20:56:23 cmoore Exp $
restore 0
docrt 1
PROC DECLARE
$for temporary names
STRING*20 DNAME,FNAME,wname,oname,pname,date,rname
STRING*80 vername
SCALAR nctmp
$for clock
STRING*2 hr,mn,sc
STRING*8 TIMSTRNG,tim1,tim2
$for HEAD
```

```
STRING*53 pounds,outlin
$stuff for the last map
SCALAR mclass, mseq,mdisk,mtype,mname
$fluxes
SCALAR A1,A2,B,C,P,IMNOISE
$positions
SCALAR cA1X,cA1Y,cA2X,cA2Y,cBX,cBY,cCX,cCY,cPX,cPy
$which one are we on?
SCALAR N,count,wdisk,ctmp
SCALAR oldb, oldp, diff, tmp
$boxflux
SCALAR xpix, ypix, numrow, xref, yref, cdeltx, cdelty, xpos, ypos
SCALAR ival, tmpx, tmpy
$round
SCALAR NUMIN, EXPON, X0, EXPFACT, X2, I1, DECLOC
STRING*13 TESTSTR
$for myconcat
STRING*48 MYTEMP
$for headt
STRING*48 outtmp,outptmp
FIN
$
vername = '$Id: proc.run,v 2.40 1996/05/09 20:56:23 cmoore Exp $'

proc myconcat
mytemp = outfile; outfile ''; concat; outfile = mytemp
ret;fin
$
$ random useful stuff cribbed mostly from MAPIT.001
$ GOWT - go and wait.  sets the task, goes, and waits.
PROC GOWT(TASK)
go; wait; ret; fin
$
$clrzap - clears and then zaps a file
PROC CLRZAP
clrstat; zap; ret; fin
$
$proc clock - returns time in TIMSTRNG HH:MM:SS
proc clock(timstrng)
daytim
hr=char(timer(4))
mn=char(timer(5))
sc=char(timer(6))
timstrng='  :  :  '
subst(timstrng,1,2)=hr; subst(timstrng,4,5)=mn
subst(timstrng,7,8)=sc
timerang 0
ret;fin
$
$ ROUND(NUMIN,EXPON,X0): round a number to the decimal place
$ written by Sam Conner                   given by 10**-EXPON

PROC ROUND(NUMIN,EXPON,X0)
 IF NUMIN>0 THEN EXPFACT=10**EXPON;ELSE;EXPFACT=-(10**EXPON);END
 X2=NUMIN+.5/EXPFA;X0=X2-MOD(X2*EXPFACT,1)/EXPFACT
 TESTSTR=CHAR(X0);DECLOC=0
 FOR I1=1 TO 12
  IF SUBSTR(TESTSTR,I1,I1)='.' THEN;DECLOC=I1;I1=12;END
 END
 IF DECLOC>0 THEN
  IF NUMIN<0 THEN
   X0=VALUE(SUBSTR(TESTSTR,1,DECLOC+EXPON+1))
  ELSE
   X0=VALUE(SUBSTR(TESTSTR,1,DECLOC+EXPON))
  END
 END
RET;FINI
```

```
$typound
POUNDS='###################################'
proc PRPND
type pounds
ret;fin

$output headline in a nice format
proc HEAD(OUTLIN)
prpnd;type '#',outlin;prpnd
ret;fin

$output headline in a nice format with the time
proc HEADT(OUTLIN)
clock(timstrng)
prpnd; type '#',timstrng;type '#',outlin;prpnd
outtmp=outfile;outptmp=outprint
outfile='MGLOGS:PROGRESS'; outprint=timstrng
puttxt; outprint=outlin; puttxt
outfile=outtmp;outprint=outptmp
ret;fin

$  Procedures to setup the adverbs correctly
$ setup for iterative phase-only self-cals
$ no smarts in here-- just help for manually runing
$ in an efficient manner.
$
$
PROC SETPCAL
calsour ''; qual -1; calcode ''; selband -1; selfreq -1; freqid 1
bchan 1; echan 0; antennas 0; subarray 0; uvrange 0 0
wtuv 0; docalib 0; gainuse 0; flagver 0; doband -1; bpver -1
smooth 0; nmaps 1; smodel 0; refant 9; solint 1; clr2name
invers 0
$ sometimes Antenna 9 is gone
if fname='JAN30' then refant=12;headt('setting refant to 12');end
if fname='MAR24' then refant=12;headt('setting refant to 12');end
if fname='MAR31' then refant=4;headt('setting refant to 4');end
if fname='APR01' then refant=4;headt('setting refant to 4');end
if fname='APR03' then refant=23;headt('setting refant to 23');end
if fname='APR05' then refant=4;headt('setting refant to 4');end
if fname='APR06' then refant=4;headt('setting refant to 4');end
if fname='APR22' then refant=4;headt('setting refant to 4');end
if fname='APR27' then refant=4;headt('setting refant to 4');end
if fname='APR29' then refant=4;headt('setting refant to 4');end
$
timerang=0
aparm 0,0,0,0,0,0,0,0,0,0
dparm 0
soltype ''; solmode 'P'; solcon 0
cparm 0,0,0,0,1

snver 1; antwt 0; gainerr 0; docat 1
in2disk=wdisk
$bug fix 22 Oct 94 CBM- added ncomp 0
ncomp 0
FINISH
$
$ setup for MX mapping between cals
PROC SETMX
clr2name; bchan 1; echan 0; channel 0; npoints 0; chinc 0; stokes ''
bif 0; eif 0; cellsize 0.02 0.02; imsize 256 256
nfield 1; fldsize 0; rashift 0; decshift 0
nboxes 0
uvtaper 0 0; uvrange 0 0; uvwtfn ''; uvbox 0; zerosp 0; xtype 5; ytype 5
xparm 0; yparm 0; gain 0.1; flux 0; minpatch 51; niter 1500; bcomp 0
bmaj 0; bmin 0; bpa 0
phat 0; factor 0; dotv -1; cmethod ' '
$send the uvwork file to the scratch disk
```

```
in2disk wdisk
FINISH
$
$ setup for uvflg
proc setflag
infile ''; sources ''; subarray 0; selband -1; selfreq -1; freqid -1
timerang 0; bchan 1; echan 0; bif 0; eif 0; antennas 0; baseline 0
stokes 'full'; flagver 1; opcode 'flag'; reason 'poor calibration'
edrop 0; bdrop 0
ret;fin
$
$set baddisk to exclude all but scratch disk
PROC BAD
baddisk 1 2 3 4 5
FINISH
$
$ do initial calibration
PROC calit
$ blow away the CL table
inext 'cl';invers 0; extdest
$ replace it with an empty one.
cparm 0,0,5,0; gowt('indxr')
$
zerosp 0; sources '0137+331'; qual -1; bif 0; eif 0
freqid 1; aparm 0;optyp 'calc'; calcode '';sysvel 0
restfreq 0 0; veltyp ''; veldef ''
gowt('setjy')

headt('running 3C 48 model calibration')
type 'loading 3c 48 model'
$ load model for 3c48
  outna '3C48MODEL';outcl '';outseq 0;outdi wdisk
  ncount 0;dotable 1;infile 'mgraw:3c48model.mrg.fits'
  ncount 0; dotable 1; nfiles 0; nmaps 1
  gowt('imlod');outna '';infile ''
type 'running calib'
setpcal; calsour '0137+331'; solint 2; solmode 'A&P'
in2na '3C48MODEL'; in2cl '';invers 0; uvrange 250 750;snver 0

$require SNR of 50 for solution
aparm(7) 50

$extend the uvrange in a couple of special cases (see notes for
$20 July 1994, 25 July 1994
if fname='JAN30' then headt 'extending uvrange for JAN30'
  uvrange 240 750; end
if fname='FEB18' then headt 'extending uvrange for FEB18'
  uvrange 175 750; end
if fname='FEB23' then headt 'extending uvrange for FEB23'
  uvrange 160 750; end
if fname='MAR24' then headt 'extending uvrange for MAR24'
  uvrange 150 750; end
if fname='APR20' then headt 'extending uvrange for APR20'
  uvrange 225 750; end
if fname='APR22' then headt 'extending uvrange for APR22'
  uvrange 195 750; end


gowt('calib')
$
headt('running phase calibrator calibration')
setpcal; clr2name; calsour '0423-013'; solmode 'A&P'
cparm 0 0 10 20 1
solint 2; snver 0
aparm(7) 50
gowt('calib')
$
headt('running GETJY,CLCAL, SPLIT')
```

```
$prep for GETJY
sources '0423-013';calsour '0137+331';soucode ''
bif 0;eif 0
calcode '';antennas 0;snver 0
subarray 0; selband -1; selfreq -1;freqid -1
$
$ set TIMERANG as a function of observing DATE
if fname='NOV04' then headt 'setting TIMERANG for NOV04'
  timerang 0 11 18 0 0 11 44 20;end
if fname='NOV13' then headt 'setting TIMERANG for NOV13'
  timerang 0 5 58 40 0 6 23 30;end
if fname='NOV14' then headt 'setting TIMERANG for NOV14'
  timerang 0 9 1 30 0 9 19 10;end
if fname='NOV18' then headt 'setting TIMERANG for NOV18'
  timerang 0 5 9 0 0 5 35 50 ;end
if fname='NOV25' then headt 'setting TIMERANG for NOV25'
  timerang 0 8 10 40 0 8 36 10 ;end
if fname='NOV26' then headt 'setting TIMERANG for NOV26'
  timerang 0 4 7 40 0 4 24 10 ;end
if fname='NOV29' then headt 'setting TIMERANG for NOV29'
  timerang 0 4 25 50 0 4 51 20 ;end
if fname='NOV30' then headt 'setting TIMERANG for NOV30'
  timerang 0 7 59 0 0 8 16 30 ;end
if fname='DEC03' then headt 'setting TIMERANG for DEC03'
  timerang 0 5 25 30 0 5 50 0 ;end
if fname='DEC15' then headt 'setting TIMERANG for DEC15'
  timerang 0 7 36 40 0 8 1 40 ;end
if fname='DEC27' then headt 'setting TIMERANG for DEC27'
  timerang 0 3 36 10 0 4 1 0 ;end
if fname='JAN04' then headt 'setting TIMERANG for JAN04'
  timerang 0 3 34 40 0 3 58 40 ;end
if fname='JAN06' then headt 'setting TIMERANG for JAN06'
  timerang 0 2 41 10 0 3 6 0 ;end
if fname='JAN07' then headt 'setting TIMERANG for JAN07'
  timerang 0 4 7 50 0 4 29 30 ;end
if fname='JAN21' then headt 'setting TIMERANG for JAN21'
  timerang 0 4 3 50 0 4 45 40 ;end
if fname='JAN24' then headt 'setting TIMERANG for JAN24'
  timerang 0 1 58 0 0 2 24 50 ;end
if fname='JAN30' then headt 'setting TIMERANG for JAN30'
  timerang 0 2 12 40 0 2 29 20 ;end
if fname='FEB03' then headt 'setting TIMERANG for FEB03'
  timerang 0 3 54 30 0 4 18 0 ;end
if fname='FEB06' then headt 'setting TIMERANG for FEB06'
  timerang 0 3 45 0 0 4 6 30 ;end
if fname='FEB12' then headt 'setting TIMERANG for FEB12'
  timerang 0 0 16 40 0 0 44 0 ;end
if fname='FEB14' then headt 'setting TIMERANG for FEB14'
  timerang 0 3 5 10 0 3 36 0 ;end
if fname='FEB18' then headt 'setting TIMERANG for FEB18'
  timerang 0 4 20 0 0 4 49 40 ;end
if fname='FEB27' then headt 'setting TIMERANG for FEB27'
  timerang 0 3 22 20 0 3 44 10 ;end
if fname='MAR05' then headt 'setting TIMERANG for MAR05'
  timerang 0 22 49 40 0 23 17 30 ;end
if fname='MAR24' then headt 'setting TIMERANG for MAR24'
  timerang 0 0 58 40 0 1 35 30 ;end
if fname='MAR31' then headt 'setting TIMERANG for MAR31'
  timerang 0 0 8 10 0 0 37 30 ;end
if fname='APR01' then headt 'setting TIMERANG for APR01'
  timerang 1 0 2 0 1 0 29 40 ;end
if fname='APR03' then headt 'setting TIMERANG for APR03'
  timerang 0 19 22 40 0 19 44 20;end
if fname='APR05' then headt 'setting TIMERANG for APR05'
  timerang 0 22 50 0 0 23 13 30;end
if fname='APR15' then headt 'setting TIMERANG for APR15'
  timerang 0 23 11 10 0 23 34 40;end
if fname='APR20' then headt 'setting TIMERANG for APR20'
```

```
  timerang 0 23 17 20 0 23 45 10 ;end
if fname='APR22' then headt 'setting TIMERANG for APR22'
  timerang 0 23 8 50 0 23 37 40;end
if fname='APR27' then headt 'setting TIMERANG for APR27'
  timerang 0 18 51 20 0 19 25 40;end
if fname='APR29' then headt 'setting TIMERANG for APR29'
  timerang 0 18 13 20 0 18 38 40 ;end
if fname='MAY01' then headt 'setting TIMERANG for MAY01'
  timerang 0 17 8 10 0 17 24 10;end
if fname='MAY03' then headt 'setting TIMERANG for MAY03'
  timerang 0 20 25 40 0 20 52 30 ;end
$
gowt('getjy')
sources '0414+053','0423-013';calsour '0137+331','0423-013'
soucode ''; qual -1; calcode ''; timerang 0; subarray 0
antennas 0; selband -1; selfreq -1; freqid -1;opcode ''; smotype ''
interpol '2PT'; intparm 0; gainver 0; gainuse 0; snver 0; gainver 0
$ this depends on the previous run on setpcal to set refant
gowt('clcal')
qual -1; calcode ''; timerang 0; stokes ''; bchan 1; bpver -1
smooth 0; douvcomp -1; aparm 0; docalib 1; gainuse 0; dopol -1
blver -1; flagver 0; doband -1; selband -1; selfreq -1; freqid -1
chansel 0; bif 0; eif 0; outdisk=indisk; outclass 'calix'
gowt('split')

$set up object name (oname)
graddres '0414'; ofmfile=wname; in2file='';dparm 0;myconcat
oname=outprint
$set up phase cal name (pname)
graddres '0423'; ofmfile=wname; in2file='';dparm 0;myconcat
pname=outprint
type 'renaming uv data files...'
  inna '0414+053';inclass 'calix'; outname=oname;rename
  inna '0423-013';inclass 'calix'; outname=pname;rename

type 'removing 3c48 model...'
  inna '3C48MODEL';incl '';inseq 0
  intyp 'ma';zap;intyp ''

type 'removing multisource database...'
  inna=wname; incla ''; intype 'uv'; indisk=wdisk;zap;recat
  headt('done with calibration step')
FINISH
$
$proc GETCC - sets ncomp to the last acceptable clean component
$take up to factor times the first negative CC
proc GETCC(factor)
opcode 'fact'
ncomp 0;flux 0;pixval 0
invers 0; ccstat
if (error > -1) then headt('ccstat returns error',error);end
ret;fin

$proc obox - sets boxes for 0414
proc obox
$find B
blc 85 168 1;trc 114 198 1
doinvers -1
imstat
imsize 5 5;prtlev -1;maxfit
cbx=pixxy(1);cby=pixxy(2)
if (error > 0) then
  if (oname = '0414MAR09') then prpnd; type 'error in maxfit (obox)'
  type 'applying drift correction for 0414MAR09'
  blc 83 137 1; trc 115 184 1; doinvers -1;imstat; imsize 5 5; prtlev -1
  maxfit
  cbx=pixxy(1);cby=pixxy(2)
  prpnd; end;end;
```

```
if (error > 0) then prpnd; type 'error in maxfit (obox)';exit;end
$calculate positions of other components
ca1x=cbx - 29.28;ca1y=cby - 96.63
round(ca1x,0,x0);ca1x = x0;round(ca1y,0,x0);ca1y=x0
ca2x=cbx - 35.91;ca2y=cby - 76.49
round(ca2x,0,x0);ca2x=x0;round(ca2y,0,x0);ca2y=x0
ccx=cbx + 68.20;ccy=cby - 81.70
round(ccx,0,x0);ccx=x0;round(ccy,0,x0);ccy=x0
round(cbx,0,x0);cbx=x0
round(cby,0,x0);cby=x0
nbox 4
box(1,1)=ca1x - 3;box(2,1)=ca1y - 3; box(3,1)=ca1x + 3; box(4,1)=ca1y + 3
box(1,2)=ca2x - 3;box(2,2)=ca2y - 3; box(3,2)=ca2x + 3; box(4,2)=ca2y + 3
box(1,3)=cbx - 3;box(2,3)=cby - 3; box(3,3)=cbx + 3; box(4,3)=cby + 3
box(1,4)=ccx - 3;box(2,4)=ccy - 3; box(3,4)=ccx + 3; box(4,4)=ccy + 3
ret;fin
$
proc pflux
pixxy 129.0 129.0;imsize 10 10
outname ''; outclass ''; outseq 0; ngauss 1; ctype 0; gmax 0; gpos 0
niter 0; domax 1; dowidth 1; dooutput -1; offset 0; domodel -1; outfile ''
imsize 5 5;maxfit;maxfit;p=pixval*1000.0
ret;FINISH
$
proc bflux
obox
blc = (cbx-3),(cby-3),1
trc = (cbx+3),(cby+3),1
doinvers -1
imstat
tmp=pixval
prtlev -1
imsize 3 3
maxfit;b=pixval*1000.0
if (error > -1) then b=0.0;end
$ check for sanity
tmp=(tmp-pixval) / pixval
if (tmp > .005) then b=-1;end
if (tmp < -.03) then b=-2;end
ret;FINISH
$
proc cflux
obox
blc = (ccx-3),(ccy-3),1
trc = (ccx+3),(ccy+3),1
doinvers -1
imstat
tmp=pixval
prtlev -1
imsize 3 3
maxfit;c=pixval*1000.0
if (error > -1) then c=0.0;end
$ check for sanity
tmp=(tmp-pixval) / pixval
if (tmp > .005) then c=-1;end
if (tmp < -.03) then c=-2;end
ret;FINISH
$
proc a1flux
obox
blc = (ca1x-3),(ca1y-3),1
trc = (ca1x+3),(ca1y+3),1
doinvers -1
imstat
tmp=pixval
prtlev -1
imsize 3 3
maxfit;a1=pixval*1000.0
```

```
if (error > -1) then a1=0.0;end
$ check for sanity
tmp=(tmp-pixval) / pixval
if (tmp > .005) then a1=-1;end
if (tmp < -.03) then a1=-2;end
ret;FINISH
$
proc a2flux
obox
blc = (ca2x-3),(ca2y-3),1
trc = (ca2x+3),(ca2y+3),1
doinvers -1
imstat
prtlev -1
imsize 3 3
tmp=pixval
maxfit;a2=pixval*1000.0
if (error > -1) then a2=0.0;end
$ check for sanity
tmp=(tmp-pixval) / pixval
if (tmp > .005) then a2=-1;end
if (tmp < -.03) then a2=-2;end
ret;FINISH
$
proc fluxes
a1flux
a2flux
bflux
cflux
head('Object Flux Density (mJy)')
type 'A1 ',a1
type 'A2 ',a2
type 'B ',b
type 'C ',c
prpnd
RET;FINISH
$
$getnoise - get noise in image of 0414 (uses a box south of the images)
proc getnoise
blc 98 21 1
trc 233 53 1
doinvers -1
imstat; imnoise= 1000*pixstd
ret;fin
$
proc outflux
keyword 'DATE-OBS'
gethe
outprint=keystrng
$ put out the observation date from the header
outfile 'MGLOGS:logfile'
puttxt
$ now get the fluxes
fluxes
getnoise
graddres=char(a1);ofmfile=char(a2)
in2file=char(b);outprint=char(c)
reason=char(imnoise)
dparm 2
myconcat
type outprint
$outputs fluxes in order a1,a2,b,c in mJy then image noise in mJy/Beam
outfile 'MGLOGS:logfile'
puttxt
ret;fin
$
proc outpflux
pflux
```

```
outprint=char(p)
type outprint
outfile 'MGLOGS:logfile'
puttxt
ret;fin
$

$boxflux - add up the clean components in the clean boxes centered on each source
proc boxflux
 a1=0;a2=0;b=0;c=0
 inext 'cc'; invers 0;outvers 0
 gowt('ccmrg')
 keyword 'num row'; getthead; numrow=keyval(1)
 keyword 'cdelt1';gethead; cdeltx=keyvalue(1)
 keyword 'cdelt2';gethead; cdelty=keyvalue(1)
 keyword 'crpix1'; gethead; xref=keyval(1)
 keyword 'crpix2'; gethead; yref=keyval(1)
 for ival= 1 to numrow
   pixxy ival 2; tabget; xpix=keyval(1)/cdeltx + keyval(2)/cdeltx + xref
   pixxy ival 3; tabget; ypix=keyval(1)/cdelty + keyval(2)/cdelty + yref
   pixxy ival 1; tabget; flux=keyval(1)*1000 + keyval(2)*1000
   type ival,xpix,ypix,'flux',flux
$ A1 flux
   tmpx = ABS(xpix-ca1x)
   tmpy = ABS(ypix-ca1y)
   if (tmpx < 5 & tmpy < 5) then a1=a1+flux
     flux=0;end
$A2 flux
   tmpx = ABS(xpix-ca2x)
   tmpy = ABS(ypix-ca2y)
   if (tmpx < 5 & tmpy < 5) then a2=a2+flux
     flux=0;end
$B flux
   tmpx = ABS(xpix-cbx)
   tmpy = ABS(ypix-cby)
   if (tmpx < 5 & tmpy < 5) then b=b+flux
     flux=0;end
$C flux
   tmpx = ABS(xpix-ccx)
   tmpy = ABS(ypix-ccy)
   if (tmpx < 5 & tmpy < 5) then c=c+flux
     flux=0;end
$be paranoid
   if (flux <> 0) then type 'Lost CC in boxflux',ival;exit;end
 end;
$get rid of the left over CC table
inext 'cc';invers 0;extdest
$print out results
head('Object Flux Density (mJy) from clean components')
type 'A1 ',a1
type 'A2 ',a2
type 'B ',b
type 'C ',c
prpnd
ret;fin
$
proc outbox
 keyword 'DATE-OBS'
 gethe
 outprint=keystrng
$ put out the observation date from the header
 outfile 'MGLOGS:boxlog'
 puttxt
$ now get the fluxes
 boxflux
 getnoise
 graddres=char(a1)
 ofmfile=char(a2)
```

```
 in2file=char(b)
 outprint=char(c)
 reason=char(imnoise)
 dparm 2
 myconcat
 type outprint
$outputs fluxes in order a1,a2,b,c in mJy then image noise in mJy/Beam
 outfile 'MGLOGS:boxlog'
 puttxt
 ret;fin
$
$readna - read the nth file name for grinding
proc readna(N)
infile 'MGDATA:NAMES'
inname ''; outprint ''
bcount=N
getstrng
if (error > -1) then headt('error in readna'); type 'n',N
type 'error',error; end
return OUTPRINT
outprint ''
fin
$ proc loaduv - given that fname contains a name, uvlod it
$ into the work disk
proc loaduv
doall 1
object ''; qual -1; band '';bcount 1; ncount 0; intape 0
nfiles 0; graddres='MGDATA:'; ofmfile=fname; in2file='';dparm 0
myconcat; infile = outprint; douvcomp -1; doconcat -1;
outseq 0
wname=fname
outname=fname; outclass=''; outdisk=wdisk
gowt('uvlod')
ret;fin
$
$
$
$proc pbox - set boxes for 0423
proc pbox
$find the source
blc 115 114 1
trc 145 145 1
doinvers -1; imstat; imsize 5 5; maxfit
nboxes 1
round(pixxy(1),0,x0); pixxy(1)=x0; cpx=x0
round(pixxy(2),0,x0); pixxy(2)=x0; cpy=x0
box(1,1)=pixxy(1) - 3; box(2,1)=pixxy(2) - 3
box(3,1)=pixxy(1) + 3; box(4,1)=pixxy(2) + 3
ret;fin
$
$boxpflux - add up the clean components in the clean boxes centered on
$           phase calibrator
proc boxpflux
 p=0
 inext 'cc'; invers 0;outvers 0
 gowt('ccmrg')
 keyword 'num row'; getthead; numrow=keyval(1)
 keyword 'cdelt1';gethead; cdeltx=keyvalue(1)
 keyword 'cdelt2';gethead; cdelty=keyvalue(1)
 keyword 'crpix1'; gethead; xref=keyval(1)
 keyword 'crpix2'; gethead; yref=keyval(1)
 for ival= 1 to numrow
   pixxy ival 2; tabget; xpix=keyval(1)/cdeltx + keyval(2)/cdeltx + xref
   pixxy ival 3; tabget; ypix=keyval(1)/cdelty + keyval(2)/cdelty + yref
   pixxy ival 1; tabget; flux=keyval(1)*1000 + keyval(2)*1000
$  type ival,xpix,ypix,'flux',flux
$ P flux
   tmpx = ABS(xpix-cpx)
```

```
   tmpy = ABS(ypix-cpy)
   if (tmpx < 5 & tmpy < 5) then p=p+flux
     flux=0;end
$be paranoid
   if (flux <> 0) then type 'Lost CC in boxpflux',ival;exit;end
 end;
$get rid of the left over CC table
inext 'cc';invers 0;extdest
$print out results
head('Phase Cal Flux Density from clean components')
type ' ',p,'mJy'
prpnd
ret;fin
$
$proc outpbox
proc outpbox
 keyword 'DATE-OBS'
 gethe
 outprint=keystrng
$ put out the observation date from the header
 outfile 'MGLOGS:boxlog'
$ puttxt
$ now get the fluxes
 boxpflux
 getnoise
 graddres=char(p)
 ofmfile=char(imnoise)
 in2file=''
 dparm 2
 myconcat
 type outprint
$outputs flux density in mJy then image noise in mJy/Beam
 outfile 'MGLOGS:boxlog'
 puttxt
 ret;fin
$
$
$
$proc getmodel - get the model from the data area and store it with name model
proc getmodel
outname '0414model';outclass ''; outseq 0
outdisk=wdisk;ncount 0;dotable 1; nfiles 0;nmaps 1
infile 'mgdata:0414MODEL'
gowt('imlod')
outname '0423model';infile 'mgdata:0423MODEL'
gowt('imlod')
ret;fin
$
$proc clean - removes uvwork files from all disks, ibeams from the present disk
proc clean
inna ''; inclass 'IBEAM'; inseq 0; intype ''; detime 0
doconfrm -1; indisk=wdisk; alldest
indisk 0; inclass 'UVWORK'; inseq 0; intype ''; detime 0
alldest; indisk=wdisk
ret;fin
$
$ scans - list scans to printer

proc scans
docrt -1;optype 'scan';inext '';inver 1;sources '';timerang 0
stokes '';bif 1;eif 2;uvrange 0;docalib 0;dparm 0;outprint ''
gowt('listx');docrt 1
ret;fin

$  slist - read in and print a scans listing for all listed sources in NAMES
$
proc slist
for N=1 to 100
```

```
  headt('Begin Observation')
  type 'N=',N; prpnd
  infile 'MGXRAW:NAMES'
  inname ''; outprint ''
  bcount=N
  getstrng
  if (error > -1) then headt('error in readna'); type 'n',N
  type 'error',error; end
  fname=OUTPRINT
  if (error > -1) then exit
  else
    doall 1
    object ''; qual -1; band '';bcount 1; ncount 0; intape 0
    nfiles 0; graddres='MGXRAW:'; ofmfile=fname; in2file='';dparm 0
    myconcat; infile = outprint; douvcomp -1; doconcat -1;
    outseq 0
    wname=fname
    outname=fname; outclass=''; outdisk=wdisk
    gowt('uvlod')
   inna = wname; inclass ''; inseq 0;indisk=wdisk
   scans
   intyp 'uv';indisk wdisk
   zap
  end
end
ret;fin
$
$
$ grind - read in from tape and then reduce one observation set wdisk
$   before use
proc grind(N)
  headt('Begin Observation')
  type vername
  type 'N=',N; prpnd
  fname=readna(N)
  if (error > -1) then exit
  else
   loaduv
   inna = wname; inclass ''; inseq 0;indisk=wdisk
$
$hacks to fix up problems not detected in the initial flagging
$

   if fname = 'NOV04' then type 'doing special flags for NOV04'
     setflag; antenna 28; timerang 0 12 0 40 0 12 0 40
     gowt('uvflg');end
   if fname = 'NOV23' then type 'doing special flags for NOV23'
     setflag; antenna 2; timerang 0 6 1 40 0 6 1 40
     gowt('uvflg');end
   if fname = 'NOV25' then type 'doing special flags for NOV25'
     setflag; antenna 22; timerang 0 8 44 0 0 8 44 0
     gowt('uvflg'); antenna 2; timerang 0 8 52 50 0 8 52 50
     gowt('uvflg'); end
   if fname = 'DEC03' then type 'doing DEC03 fixup and flags'
     inext 'cl'; invers 2; extdest; inext 'sn'; invers 0; extdest
     sources '0423-013',''; bif 0; eif 0; zerosp 0; optype 'rese'
     gowt('setjy')
     setflag; antennas 2 4; timerang 0 6 20 20 0 7 0 0
     gowt('uvflg');end
   if fname = 'JAN06' then type 'doing special flags for JAN06'
     setflag; antenna 28; gowt('uvflg'); end
   if fname = 'JAN24' then type 'doing special flags for JAN24'
     setflag; antenna 28; baseline 7; gowt('uvflg')
     baseline 0; end
   if fname = 'JAN30' then type 'doing special flags for JAN30'
     setflag; antenna 25; bif 2; eif 2
     gowt('uvflg');bif 1; end
   if fname = 'FEB23' then type 'doing special flags for FEB23'
```

```
     setflag; antenna 28; timerang 0 4 41 30 0 4 41 30
     gowt('uvflg');antenna 28; bif 1;eif 1
     timerang 0 5 24 10 0 5 24 10; gowt('uvflg')
     antenna 23; bif 2; eif 2; timerang 0 5 22 40 0 5 22 50
     gowt('uvflg'); end
   if fname = 'MAR15' then type 'doing special flags for MAR15'
     setflag; antenna 3; bif 1; eif 1
     timerang 0 22 37 30 0 23 16 0; gowt('uvflg')
     antenna 24; bif 2; eif 2; gowt('uvflg')
     antenna 17; bif 2; eif 2; timerang 0 23 29 10 0 23 46 50
     gowt('uvflg')
     $more to come ?
     end
   if fname = 'MAR18' then type 'doing special flags for MAR18'
     setflag; antenna 18; timerang 1 0 3 0 1 0 15 10
     gowt('uvflg'); bif 2;eif 2; antenna 16; gowt('uvflg')
     antenna 10; bif 1; eif 1; timerang 0 23 54 10 1 0 1 0
     gowt('uvflg'); antennas 7 14 17 20 21 26 28;bif 2;eif 2
     timerang 0 23 36 20 0 23 51 50; gowt('uvflg'); bif 1;eif 1
     antennas 4; gowt('uvflg'); antennas 26
     timerang 0 23 21 0 0 23 26 20; gowt('uvflg')
     timerang 0 23 21 0 0 23 51 50; bif 2;eif 2; antenna 19
     gowt('uvflg')
     end
   if fname = 'MAR24' then type 'doing special flags for MAR24'
     setflag; antenna 14; gowt('uvflg');end
   if fname = 'MAR31' then type 'doing special flags for MAR31'
     setflag; antenna 9; baseline 28; timerang 0 1 3 0 0 1 3 0
     gowt('uvflg');end
   if fname = 'APR03' then type 'doing special flags for APR03'
     setflag; antenna 5 16; timerang 0 19 59 10 0 19 59 50
     gowt('uvflg'); antenna 15; timerang 0 20 0 0 0 20 6 40
     gowt('uvflg'); antenna 8; timerang 0 20 8 30 0 20 8 30
     gowt('uvflg'); antenna 15; timerang 0 20 10 0 0 20 22 50
     gowt('uvflg'); end
   if fname = 'APR20' then type 'doing special flags for APR20'
     setflag; antenna 1; timerang 0 23 52 50 0 23 52 50
     gowt('uvflg'); antenna 1; bif 2;eif 2
     timerang 0 23 53 10 0 23 53 10; gowt('uvflg')
   end
   calit

   $now we have names set to objects+MGnn e.g. 0414MG2
   $do dirty maps
$   headt('Making Dirty Maps')
$   setmx; niter 0; inname = oname; incl='calix';inseq 0
$   outname='*D'; in2di = wdisk; gowt('mx')
$   inna=outna;incl 'uvwork'; intype 'uv'; indisk=wdisk;zap
$   incl '?BEAM'; intype 'ma' ; indisk=wdisk;zap
$   inna = pname; incl='calix';inseq 0
$   outname='*D'; gowt('mx')
$   inna=outna;incl 'uvwork'; intype 'uv'; indisk=wdisk;zap
$   incl '?BEAM'; intype 'ma' ; indisk=wdisk;zap
$   inna=oname

   $now do a map to set the clean boxes
   headt('Making an initial map of 0414+053')
   setmx; inname = oname;incl='';inseq 0
   outname=inna; outclass ''; in2disk = wdisk
   gowt('mx')
   incl 'uvwork'; intype 'uv'; indisk=wdisk;zap
   incl '?BEAM'; intype 'ma' ; indisk=wdisk;zap
   recat

   $set the clean boxes and get the first cc model
   headt('Setting clean boxes for initial 0414 CC model')
   incl 'icln'; intype 'ma'; indisk=wdisk
   obox; zap; recat;incl 'CALIX';inseq 0; inname=oname
```

```
   setmx; nbox 4
   gowt('mx')
   incl 'uvwork'; intype 'uv'; indisk=wdisk;zap
   incl '?BEAM'; intype 'ma' ; indisk=wdisk;zap
   recat

$ do the calibration for 0414
   for count=1 to 20
     graddres 'Begin 0414 calibration iteration'
     ofmfile =char(count);in2file ''
     dparm 1; myconcat; headt(outprint)

     inna=oname;incl 'ICLN'; inseq 0
     getcc(-2)
     nctmp = ncomp(1)
     bflux; oldb=b
     prpnd; type 'Using',nctmp,'clean components.'
     type 'bflux=',b
     prpnd

     prpnd; type 'Setting Clean Boxes'
     obox
     prpnd

     $change the name of the old data set
     $so that we can easily zap it when calix is done
     inna=oname; incl 'calix'; outna =inna
     outclass 'cal'; outseq 0; rename

     setpcal;in2na=oname; in2cl='icln';in2seq=0
     inna=oname; incl='cal';inseq=0
     outname=oname; outcl ''; outseq=0
     if (count < 2) then aparm(9)=1;end
     ncomp(1) = nctmp; type 'using',ncomp(1),'Clean Components'
     gowt('calix')

     type 'cleaning up old uvdata.'
     inclass 'cal';intype 'uv'; indisk=wdisk;zap

     type 'cleaning up old map.'
     inna=oname; incl='icln'; indisk=wdisk;inseq=0;intype 'ma'
     zap

     recat

     setmx;nbox 4;incl='calix';inseq=0;in2disk=wdisk;gowt('mx')
     incl 'uvwork'; intype 'uv';indisk=wdisk; zap
     incl '?BEAM'; intype 'ma' ;indisk=wdisk; zap
     recat
     incl 'icln';obox
     bflux; diff=(b - oldb) / oldb * 100
     $test for failure in bflux
     if (b < 0) then headt('failure in bflux');exit;end
     type 'diff is'
     type diff
$ cannot end on first iteration
     if (count=1) then diff = 10;end
     if (diff < 0.1) then ctmp=count;count=20;prpnd;prpnd;prpnd;end
   end;

   type 'cleaning up old map.'
   inna=oname; incl='icln'; indisk=wdisk;inseq=0;intype 'ma'
   zap
   recat

$make map for finding fluxes with MAXFIT (with .1" restoring beam)
   prpnd; type 'making MAXFIT map of 0414';prpnd
   setmx;nbox 4;incl='calix';inseq=0;in2disk=wdisk
```

```
   bmaj 0.1;bmin 0.1
   gowt('mx')
   incl 'uvwork'; intype 'uv';indisk=wdisk; zap
   incl '?BEAM'; intype 'ma' ;indisk=wdisk; zap
   recat
   $record final fluxes to file
   incl 'icln'; outflux
   zap;recat

$make final map
   prpnd; headt 'making final map of 0414 residuals';prpnd
   setmx;nbox 4;incl='calix';inseq=0;in2disk=wdisk
   bmaj -1
   gowt('mx')
   incl 'uvwork'; intype 'uv';indisk=wdisk; zap
   incl '?BEAM'; intype 'ma' ;indisk=wdisk; zap
   recat
$move the residual map to a new name
$and make the final CLEAN map
   incl 'icln'; intype 'ma'
   graddres fname; ofmfile 'res'; in2file ''; outprint '';dparm 0;myconcat
   rname=outprint
   outname rname;userid 0; outclass 'imap';outseq 0; rename
$now make the clean map
   headt('restoring the CLEAN components for the final map')
   inname rname; incl 'imap'; blc 0; in2na rname; in2cl incl
   outname oname; outcl 'icln'; niter 0; bmaj 0;bmin 0; bpa 0
   gowt('rstor');clr2na
   inna oname;incl 'icln'
$find fluxes by adding CC's
   outbox
$do some JMFTX'ing
$label the output file
   graddres = '0414 self-calibration iterations ='
   ofmfile = char(ctmp)
   in2file ''
   dparm 1
   myconcat
   outfile 'MGLOGS:JMFITLOG'
   puttxt

   userid 0; ctype 0
   gmax 0; gpos 0; gwidth 0; niter 0
   domax 1; dopos 1; dowidth 1
   docrt 1; outprint ''; dooutput -1; offset 0
   domodel -1

$fit A1-A2 simultaneously with fixed positions
   outprint 'A1 and A2'; puttxt
   $find B
   blc 85 168 1;trc 114 198 1
   doinvers -1
   imstat
   imsize 2 2;prtlev -1;maxfit
   cbx=pixxy(1);cby=pixxy(2)
   if (error > 0) then prpnd; type 'error in maxfit (obox)';exit;end
   $calculate positions of other components
   ca1x=cbx - 29.24;ca1y=cby - 96.56
   ca2x=cbx - 35.86;ca2y=cby - 76.47

   gpos(1,1)=ca1x;gpos(2,1)=ca1y
   gpos(1,2)=ca2x;gpos(2,2)=ca2y
   ngauss 2; outname ''; outclass '';
   blc 54 81 1
   trc 74 112 1
   niter 100
   dopos 0
   gowt('jmftx')
```

```
$fit B alone
   obox
   outprint 'B alone'; puttxt
   ngauss 1
   gpos(1,1)=cbx;gpos(2,1)=cby
   blc = (cbx - 15),(cby - 15),1
   trc = (cbx + 15),(cby + 15),1
   gowt('jmftx')
$fit C alone
   outprint 'C alone'; puttxt
   ngauss 1
   gpos(1,1)=ccx;gpos(2,1)=ccy
   blc = (ccx - 15),(ccy - 15),1
   trc = (ccx + 15),(ccy + 15),1
   gowt('jmftx')


$save the goods off to our data disk

   graddres 'mgtape:'
   ofmfile oname
   in2file '.icln'
   outprint ''
   dparm 0
   myconcat
   outfile = outprint
   intype 'ma';incl 'icln';inna oname
   dostokes -1; dotable 1; dotwo -1; donewtab 1; format 0
   gowt('fittp')
   zap; in2file '.calix'; outprint ''; myconcat
   outfile = outprint
   incl 'calix';intype 'uv'; gowt('fittp');zap
   recat

   graddres 'mgtape:'
   ofmfile oname
   in2file '.resid'
   outprint ''
   dparm 0
   myconcat
   outfile = outprint
   intype 'ma'; incl 'imap'
   inna rname
   dostokes -1; dotable 1; dotwo -1; donewtab 1; format 0
   gowt('fittp')
   zap; recat

   $a map to set the clean box for 0423
   headt('Making an initial map of 0423-013')
   setmx; inna=pname; incl ''; intyp 'uv';inseq 0
   outname=inna; outcl ''; in2disk=wdisk
   gowt('mx')
   incl 'uvwork'; intype 'uv'; indisk=wdisk;zap
   incl '?BEAM'; intype 'ma' ; indisk=wdisk;zap
   recat

   $set the box and make the first cc model
   headt('Setting clean box for inital 0423 CC model')
   incl 'icln'; intype 'ma';indisk wdisk;pbox
   zap; recat; incl 'calix'; inseq 0; inna=pname
   setmx; nbox 1
   gowt('mx')
   incl 'uvwork'; intype 'uv'; indisk=wdisk;zap
   incl '?BEAM'; intype 'ma' ; indisk=wdisk;zap
   recat

$ do the calibration for 0423
   for count=1 to 20
```

```
     graddres 'Begin 0423 calibration iteration'
     ofmfile =char(count);in2file ''
     dparm 1; myconcat; headt(outprint)

     inna=pname;incl 'ICLN'; inseq 0
     getcc(-2)
     pflux; oldp=p

     prpnd; type 'Using',ncomp,'clean components.'
     type 'flux=',p
     prpnd

     prpnd
     type 'Setting Clean Box'
     pbox
     prpnd

     $change the name of the old data set
     $so that we can easily zap it when calix is done
     inna=pname; incl 'calix'; outna =inna
     outclass 'cal'; outseq 0; rename

     setpcal;in2na=pname; in2cl='icln';in2seq=0
     inna=pname; incl='cal';inseq=0
     outname=pname; outcl ''; outseq=0
     if (count < 3) then aparm(9)=1;end
     gowt('calix')

     type 'cleaning up old uvdata.'
     inclass 'cal';intype 'uv'; indisk=wdisk;zap

     type 'cleaning up old map.'
     inna=pname; incl='icln'; indisk=wdisk;inseq=0;intype 'ma'
     indisk=wdisk;zap
     recat

     setmx;nbox 1;incl='calix';inseq=0;in2disk=wdisk
     gowt('mx')
     incl 'uvwork'; intype 'uv';indisk=wdisk; zap
     incl '?BEAM'; intype 'ma' ;indisk=wdisk; zap
     recat

     incl 'icln'

     pflux; diff = (p-oldp)/oldp * 100
     pbox;
     if (count < 2) then diff=10;end
     if (diff < 0.1) then count=20;end
   end;

   type 'cleaning up old map.'
   inna=pname; incl='icln'; indisk=wdisk;inseq=0;intype 'ma'
   zap
   recat

$make uvplot
   prpnd; type 'making uvplot of 0423';prpnd
   incl='calix';inseq 0; outname '';outcl 'uvavg'
   xinc 1; yinc 60; opcode ''; optype ''
   gowt('uvavg')

   incl='uvavg';inseq=0;timerang 0;antennas 0;uvrange  0
   baseline 0;subarray 0;bif 1;bparm 0 12;cparm 0;xinc 1
   sources ''
   keyword 'DATE-OBS'
   gethe
   outprint=keystrng
$   gowt('uvplx')
```

```
   invers 0;lpen 1
$   gowt('lwpla')
   incl 'uvavg';inseq 0; intype 'uv'
   clrzap

$make final map
   prpnd; type 'making final map of 0423';prpnd
   setmx;nbox 1;incl='calix';inseq=0;in2disk=wdisk
   gowt('mx')
   incl 'uvwork'; intype 'uv';indisk=wdisk; zap
   incl '?BEAM'; intype 'ma' ;indisk=wdisk; zap
   recat

   $record final fluxes to file
   incl 'icln'; outpflux; outpbox

$save the goods off to our data disk
   graddres 'mgtape:'
   ofmfile pname
   in2file '.icln'
   outprint ''
   dparm 0
   myconcat
   outfile = outprint
   dostokes -1; dotable 1; dotwo -1; donewtab 1; format 0
   intype 'ma'
   gowt('fittp')
   zap; in2file '.calix'; outprint ''; myconcat
   outfile = outprint
   incl 'calix'; intype 'uv';gowt('fittp');zap
   recat
$save the message file
   priority 0;prnumber 0; prtask '';prtime 0; docrt -1
   outprint 'MGTAPE:messages'; prtmsg; docrt 1;clrmsg
 end;
ret;fin
$

$ concat - a verb to concatenate strings
$ getstrng - get a string from a file
$ getarrary - get numbers from a file
$ puttxt - put text in a file
$ wformat - put numbers in a file with format ala fortran
$
$
$ some extras

$$$$$$$$$$$$$$$$$$$$$$$$$$$$$$$$$$$$$
$
$ extuv - a munged version of grind for extracting uvdata
$
proc extuv
for N=1 to 60
  headt('Begin Observation')
  type 'N=',N; prpnd
  fname=readna(N)
  if (error > -1) then N=100
  else
   clrmsg
   loaduv
   inna = wname; inclass ''; inseq 0;indisk=wdisk

   zerosp 5.0 0; sources '0423-013'
   bif 1; eif 2
   optype ''; calcode ''; freqid 1; aparm 0
   gowt('setjy')
   setpcal; clr2name; calsour '0423-013'; solmode 'A&P'
   cparm 0 0 10 20 1
```

```
   solint 10
   gowt('calix')
   sources '0137+331','0542+498','0521+166','0423-013','';soucode ''
   timerang 0; subarray 0
   antennas 0; selband -1; selfreq -1; opcode ''; smotype ''
   interpol '2PT'; gainver 0; gainuse 0; snver 1; gainver 0
   gainuse 0
   go clcal; wait clcal

   uvrange 100 300; niter 32000; stokes ''
   sources '0542+498',''; wtuv 0; docrt 0
   timerang 0; antennas 0; baseline 0
   docalib 1; gainuse 0; xinc 0; smooth 0
   opcode 'clip'; aparm .1 .1 0.01 0.01
   graddres='MGUV:';ofmfile='0542';in2file=fname;outprint ''
   dparm 0; myconcat
$ now OUTPRINT is set for uvfnd
   gowt('uvfnd')
   getna 1; clrzap
 end
end
ret;fin
$$$$$$$$$$$$$$$$$$$$$$$$$$$$$$$$$$$$$$$$
$
$ extel - a munged version of grind for extracting elevations
$
proc extel
for N=1 to 100
  headt('Begin Observation')
  type 'N=',N; prpnd
  fname=readna(N)
  if (error > -1) then N=100
  else
   clrmsg
   loaduv
   inna = wname; inclass ''; inseq 0;indisk=wdisk
   timerang 0
   uvrange 0; antennas 0; subarray 0
   sources '0137+331',''
   bif 1; eif 1
   docrt 0; optype 'gain'
   inext 'cl'
   dparm(1) 11
   outprint 'mglogs:elevation.3c48'
   gowt('listx')
   intype 'uv'; clrzap
 end
end
ret;fin

$Proc clrall - Clears all old messages
proc clrall
i=prnum
prnum -1
clrmsg
prnum = i
ret;fin

$kill gets, clrstat's and zaps
proc kill(tmp)
getna tmp
clrstat
zap
ret;fin

$getoma - get object map
proc getoma(oname)
graddres '0414';ofmfile oname;in2file '';dparm 0;myconcat
```

```
outname outprint;outclass 'ICLN';outseq 0
graddres 'MGTAPE:';ofmfile=outprint; in2file='.icln'
outprint '';myconcat
infile = outprint; outdisk=wdisk
gowt('imlod');outname ''
ret;fin

$getresid- get residual 0414 map
proc getresid(oname)
outname '';outclass 'IMAP';outseq 0
graddres '0414';ofmfile oname;in2file '';dparm 0;myconcat
graddres 'MGTAPE:';ofmfile=outprint; in2file='.resid'
outprint '';dparm 0; myconcat
infile = outprint; outdisk=wdisk
gowt('imlod');outname ''
ret;fin

$getpma - get phase cal map
proc getpma(oname)
graddres '0423';ofmfile oname;in2file '';dparm 0;myconcat
outname outprint;outclass 'ICLN';outseq 0
graddres 'MGTAPE:';ofmfile=outprint; in2file='.icln'
outprint '';myconcat
infile = outprint; outdisk=wdisk
gowt('imlod'); outname ''
ret;fin

$getouv - get object uv data
proc getouv(oname)
graddres '0414';ofmfile oname;in2file '';dparm 0;myconcat
outname outprint;outclass 'CALIX';outseq 0
graddres 'MGTAPE:';ofmfile=outprint; in2file='.calix'
outprint '';myconcat
infile = outprint
douvcomp -1;doconcat -1; outseq 0; outdisk=wdisk
gowt('uvlod'); outname ''
ret;fin

$getpuv - get phase calibrator uv data
proc getpuv(oname)
graddres '0423';ofmfile oname;in2file '';dparm 0;myconcat
outname outprint;outclass 'CALIX';outseq 0
graddres 'MGTAPE:';ofmfile=outprint; in2file='.calix'
outprint '';myconcat
infile = outprint
douvcomp -1;doconcat -1; outseq 0;outdisk=wdisk
gowt('uvlod'); outname ''
ret;fin

$getraw
proc getraw(oname)
graddres 'MGRAW:AH478';ofmfile oname; in2file '';dparm 0;myconcat
infile = outprint
object '';band '';intape 1; nfiles 0; douvcomp -1
doconcat -1; outname '';outclass '';outdisk wdisk
gowt('uvlod')
ret;fin
$
$getdata
proc getdata(oname)
graddres 'MGDATA:';ofmfile oname; in2file '';dparm 0;myconcat
infile = outprint; outprint ''
object '';band '';intape 1; nfiles 0; douvcomp -1
doconcat -1; outname '';outclass '';outdisk wdisk
gowt('uvlod')
ret;fin
$
$ proc dir(i) clrna's and then does a cat
```

```
proc dir(i)
clrna; indi i; cat
ret;fin
$
$$$$$$$$$$$$$$$$$$$$$$$$$$$$$$$$$$$$$
$
$ plots - a munged version of grind for doing uvplt's of calibrated data
$
proc plots
for N=1 to 100
  headt('Begin Observation')
  type 'N=',N; prpnd
  fname=readna(N)
  if (error > -1) then N=100
  else
   clrmsg
   getpuv(fname)
   inna = wname; inclass ''; inseq 0;indisk=wdisk


   sources '0424-013',''
   timerang 0; antennas 0; baseline 0; uvrange 0
   docalib 0; gainuse 0; xinc 0; smooth 0; bparm 0;bif 2
   gowt('uvplt'); invers 0; functype ''; dparm 0
   graddres 'DA06:0424plot'; ofmfile = char(N); in2file ''
   myconcat; outfile=outprint;lpen 2
   gowt ('lwpla')

   getna 1; zap
 end
end
ret;fin


$$$$$$$$$$$$$$$$$$$$$$$$$$$
$set up a few things
clrall
bad
wdisk 6
uvcopprm(4) 1
headt(subst(vername,1,40))
```

Appendix B

AIPS Run Files for X-Band Data Reduction

B.1 Introduction

This appendix contains the two "run files" that were used to process the 8 GHz data (see chapter 5). The language used here is essentially the same as that used in the 15 GHz run file of appendix A except that the procedures run in the `15JAN96` version of AIPS which has some new tasks and that the Conner extensions are not used.

There are two files, with a set of utility procedures (`util.proc`) that is loaded before the main file (`proc.run`). The reduction strategy is simmilar to the one used for the 15 GHz data and important differences are noted below:

`calit` uses a better model of 3C 48 (see section 5.3) and can use either of two scans on 3C 48 to do its work. The choice of scans is controlled by the use of the `calset` variable which may be set to 1 or 2. Where there were observational reasons to prefer one of the scans, the preferred scan was placed in `calset 1`.

`grind` now takes a name since SRC's `readln` procedure is not available. The self-calibration loop now ends when the RMS map noise in an off-source region improves by 0.05% or less.

`obox` now uses a fixed position for image B when working with C-array data since there is no peak to set the position with C-array resolution.

`setmx` uses a slightly larger cell size for all of the data and sets a larger image size for

C-array data.

imnoise finds the noise in a non-signal region of the map to the west of the images in order to avoid flux from A1+A2 when the beam gets large. For C-array data, it uses a different box than for A and B-array data.

B.2 Utilities — "`util.proc`"

```
$ utility routines for use alone and with proc.run
$ $Id: util.proc,v 1.28 1995/12/08 22:48:08 cmoore Exp $
restore 0
proc DECLARE
SCALAR wdisk,tmp,mdisk,ucount
STRING*20 name,dname,fname,wname,msgfile
$stuff for round
SCALAR NUMIN, EXPON, X0, EXPFACT, X2, I1, DECLOC
STRING*13 TESTSTR
$ prpnd
STRING*53 POUNDS
$ head
STRING*53 OUTLIN
STRING*80 utilver
$ temp name storage
STRING*80 tmpinna
STRING*10 tmpincl
SCALAR tmpinseq,tmpindi
STRING*10 tmpinty
$savedata stuff
SCALAR ICH,LCH
STRING*48 FITSFILE
STRING*12 SVNAME
STRING*6  SVCLASS
STRING*2  SVTYPE
STRING*1 LASTCH
fin
$ wdisk = the work disk, mdisk = disk where the 3c48 model lives
$
utilver = '##$Id: util.proc,v 1.28 1995/12/08 22:48:08 cmoore Exp $'

$ GOWT - go and wait.  sets the task, goes, and waits.
PROC GOWT(TASK)
go; wait; ret; fin
$clrzap - clears status and then zaps a file
PROC CLRZAP
clrstat; zap; ret; fin
$zaps work files
proc wzap
   incl 'uvwork'; intype 'uv';indisk=wdisk; zap
   incl '?BEAM'; intype 'ma' ;indisk=wdisk; zap; incl ''
   recat
ret;fin
$Proc clrall - Clears all old messages
proc clrall
i=prnum;prnum -1;;clrmsg;prnum = i
ret;fin
$kill gets, clrstat's, zaps, and restores the original contents of inname,etc
proc kill(tmp)
tmpinna = inname; tmpincl = inclass; tmpinseq= inseq; tmpinty=intype
getna tmp; clrstat; zap
inna = tmpinna; inclass =  tmpincl; inseq = tmpinseq; intype = tmpinty
```

```
ret;fin
$
proc mkill(i,j)
for ucount = i to j by 1
kill ucount; end
ret;fin
$ proc dir(i) clrna's and then does a cat and restores file info if
$              indi hasn't changed
proc dir(i)
tmpinna = inname; tmpincl = inclass; tmpinseq= inseq; tmpinty=intype
tmpindi = indisk;clrna; indi i; cat
if indisk = tmpindi then
   inna = tmpinna; inclass =  tmpincl; inseq = tmpinseq; intype = tmpinty
end
ret;fin

$clears out 2 SN tables and the highest numbered CL
proc clrcal
inext 'cl';invers 0;extdest;inext 'sn';extdest;extdest
ret;fin

$
$ ROUND(NUMIN,EXPON,X0): round a number to the decimal place
$ written by Sam Conner                  given by 10**-EXPON

PROC ROUND(NUMIN,EXPON,X0)
 IF NUMIN>0 THEN EXPFACT=10**EXPON;ELSE;EXPFACT=-(10**EXPON);END
 X2=NUMIN+.5/EXPFA;X0=X2-MOD(X2*EXPFACT,1)/EXPFACT
 TESTSTR=CHAR(X0);DECLOC=0
 FOR I1=1 TO 12
  IF SUBSTR(TESTSTR,I1,I1)='.' THEN;DECLOC=I1;I1=12;END
 END
 IF DECLOC>0 THEN
  IF NUMIN<0 THEN
   X0=VALUE(SUBSTR(TESTSTR,1,DECLOC+EXPON+1))
  ELSE
   X0=VALUE(SUBSTR(TESTSTR,1,DECLOC+EXPON))
  END
 END
RET;FINI

$type some pounds
POUNDS='###################################'
proc PRPND
type pounds; ret;fin
$output headline in a nice format
proc head(outlin)
prpnd;type '##',outlin;prpnd
ret;fin
$save the message file and clear it
proc savemsg
priority 0;prnumber 0; prtask '';prtime 0; docrt -1
outprint msgfile; prtmsg; docrt 1;outprint ''
clrmsg;ret;fin
$ proc loaduv - given that fname contains a name, uvlod it
$ into the work disk
proc loaduv
doall 1
object ''; qual -1; band '';bcount 1; ncount 0; intape 0
nfiles 0; infile = 'XFLAG:' !! fname
douvcomp -1; doconcat -1;outseq 0;wname=fname
outname=fname; outclass=''; outdisk=wdisk
gowt('uvlod');ret;fin
$

$getoma - get object map
proc getoma(fname)
outname '';outclass 'ICLN';outseq 0
```

```
infile = 'XTAPE:0414' !! fname !! '.icln'
outdisk=wdisk;gowt('imlod');outname ''
ret;fin

$getresid- get residual 0414 map
proc getresid(fname)
outname '';outclass 'IMAP';outseq 0
infile = 'XTAPE:0414' !! fname !! '.resid'
outdisk=wdisk; gowt('imlod');outname ''
ret;fin

$getouv - get object uv data
proc getouv(fname)
outname '';outclass 'CALIB';outseq 0
infile = 'XTAPE:0414' !! fname !! '.calib'
douvcomp -1;doconcat -1; outseq 0; outdisk=wdisk
gowt('uvlod'); outname ''
ret;fin
$getpma - get phase cal map
$proc getpma(oname)
$graddres '0423';ofmfile oname;in2file '';dparm 0;myconcat
$outname outprint;outclass 'ICLN';outseq 0
$graddres 'MGTAPE:';ofmfile=outprint; in2file='.icln'
$outprint '';myconcat
$infile = outprint; outdisk=wdisk
$gowt('imlod'); outname ''
$ret;fin

$ extel -  extracting elevations
$
proc extel(fname)
  head('Begin Observation')
  loaduv
  inna = wname; inclass ''; inseq 0;indisk=wdisk
  timerang 0
  uvrange 0; antennas 0; subarray 0
  sources '0137+331',''
  bif 1; eif 1; docrt 0; optype 'gain'
  inext 'cl'; dparm(1) 11
  outprint 'XBAND:elevation.3c48'
  gowt('listx');intype 'uv'; clrzap
ret;fin

$set baddisk to exclude all but scratch disk
PROC BAD
baddisk 1 2 3 4
FINISH

clrall
$
docrt 1

type subst(utilver,1,60)

msgfile = 'xband:messages'
type 'message file',msgfile
```

B.3 Main Procedures — "proc.run"

```
$ proc.run - reduction software for MG0414 X-band monitoring run
$ original taken from proc.run for the U-band data (version 2.38 1994/11/07)
$ depends on util.proc being loaded first
$ $Id: proc.run,v 1.60 1996/05/24 04:52:24 cmoore Exp $
```

```
PROC DECLARE
STRING*20 month
SCALAR day, carray, calset
$for temporary names
STRING*20 oname,pname,rname
STRING*80 vername,tname
SCALAR nctmp
$stuff for the last map
SCALAR mclass, mseq,mdisk,mtype,mname,reference
$fluxes
SCALAR A1,A2,B,C,P,IMNOISE,OLDNOISE
$positions
SCALAR cA1X,cA1Y,cA2X,cA2Y,cBX,cBY,cCX,cCY,cPX,cPy
$which one are we on?
SCALAR N,count,ctmp
SCALAR oldb, oldp, diff, tmp
$boxflux
SCALAR xpix, ypix, numrow, xref, yref, cdeltx, cdelty, xpos, ypos
SCALAR ival, tmpx, tmpy,saveiter
FIN
$
vername = '##$Id: proc.run,v 1.60 1996/05/24 04:52:24 cmoore Exp $'

$proc histid - write id info into history
proc histid
dohist 0;comment 'Processed by:'; hinote
comment subst(utilver,1,60); hinote
comment subst(vername,1,59); hinote
comment ''; ret;fin

$  Procedures to setup the adverbs correctly
$ setup for iterative phase-only self-cals
$
PROC SETPCAL
calsour ''; qual -1; calcode ''; selband -1; selfreq -1; freqid 1
bchan 1; echan 0; antennas 0; subarray 0; uvrange 0 0
wtuv 0; docalib 0; gainuse 0; flagver 0; doband -1; bpver -1
smooth 0; nmaps 1; smodel 0; refant reference; solint 1; clr2name
invers 0;cmethod ''; cmodel ''; smodel 0
ncomp 0; timerang=0; aparm 0,0,0,0,0,0,0,0,0,0
dparm 0;soltype ''; solmode 'P'; solcon 0
cparm 0,0,0,0,1
snver 0; antwt 0; gainerr 0; docat 1;in2disk=wdisk
FINISH
$
$ setup for NX mapping between cals
PROC SETNX
clr2name; bchan 1; echan 0; channel 0; npoints 0; chinc 0; stokes ''
bif 0; eif 0; cellsize 0.03 0.03; imsize 256 256
nfield 1; fldsize 0; rashift 0; decshift 0; nboxes 0
uvtaper 0 0; uvrange 0 0; uvwtfn ''; uvbox 0; zerosp 0; xtype 5; ytype 5
xparm 0; yparm 0; gain 0.1; flux 0; minpatch 51; niter 1500; bcomp 0
bmaj 0; bmin 0; bpa 0; phat 0; factor 0; dotv -1; cmethod ' '
if (carray = 1) then type 'using C array parameters';imsize 512 512;end
$send the uvwork file to the scratch disk
in2disk wdisk
FINISH
$
$ setup for uvflg
proc setflag
infile ''; sources ''; subarray 0; selband -1; selfreq -1; freqid -1
timerang 0; bchan 1; echan 0; bif 0; eif 0; antennas 0; baseline 0
stokes 'full'; flagver 1; opcode 'flag'; reason 'poor calibration'
edrop 0; bdrop 0; uvrange 0 0; doband -1; bpver -1; dparm 0; smooth 0
dohist 1; docalib 1;gainuse 0;ret;fin
$
$ added for uband polarization work
```

```
proc setpolcal
timerang 0; antennas 0; uvrange 0; bif 0; eif 0; docalib 1
gainuse 0; clr2na; pmodel 0; solint 2; soltype 'appr'
prtlev 1; refant reference; cparm 0;bparm 0;ret;fin
$
$ do initial calibration -  name is already set
PROC calit
zerosp 0; sources '0137+331',''; qual -1; bif 0; eif 0
aparm 0;optyp 'calc'; calcode '';sysvel 0
restfreq 0 0; veltyp ''; veldef '';freqid 1
gowt('setjy')
$
head('running 3C 48 model calibration')
$ assume that model is loaded on disk 2 under name 3c48model
setpcal; calsour '0137+331',''; solint 2; solmode 'A&P'
in2na '3C48MODEL'; in2cl '';in2di mdisk
invers 0; uvrange 0 400;snver 0
$require SNR of 10 for solution
aparm(7) 10
$use dft since we are dealing with wildly varying sampling
cmethod 'dft'; cmodel 'comp' ; gowt('calib'); clr2name
$
head('running phase calibrator calibration')
setpcal; clr2name; calsour '0424+020',''; solmode 'A&P'
cparm 0 0 10 20 1; solint 1; snver 0; aparm(7) 10
gowt('calib')
$
head('running GETJY,CLCAL, SPLIT')
$prep for GETJY
sources '0424+020','';calsour '0137+331','';soucode ''
bif 0;eif 0; calcode '';antennas 0;snver 0
subarray 0; selband -1; selfreq -1;freqid -1
$
$ set TIMERANG as a function of observing DATE
timerang 0
if calset=1 then
type 'Using calset 1'
if fname='MAR01' then timerang 0 1 31 30 0 1 37 10;end
if fname='MAR06' then timerang 0 23 19 10 0 23 27 30;end
if fname='MAR09' then timerang 0 0 13 40 0 0 19 30;end
if fname='MAR13' then timerang 0 19 40 30 0 19 46 50;end
if fname='MAR17' then timerang 0 19 54 20 0 20 1 0;end
if fname='MAR19' then timerang 0 0 27 30 0 0 38 0;end
if fname='MAR20' then timerang 0 18 59 0 0 19 10 30;end
if fname='MAR28' then timerang 0 1 58 50 0 2 10 20;end
if fname='MAR30' then timerang 0 0 21 0 0 0 32 10;end
if fname='APR06' then timerang 0 1 9 40 0 1 15 10;end
if fname='APR11' then timerang 0 20 2 20 0 20 10 0;end
if fname='APR19' then timerang 0 22 58 30 0 23 5 40;end
if fname='APR25' then timerang 0 21 1 40 0 21 10 50;end
if fname='APR28' then timerang 0 23 39 0 0 23 43 50;end
if fname='APR29' then timerang 0 17 6 20 0 17 12 0;end
if fname='MAY02' then timerang 0 21 24 0 0 21 29 20;end
if fname='MAY09' then timerang 0 21 25 40 0 21 31 40;end
if fname='MAY12' then timerang 0 23 14 20 0 23 19 40;end
if fname='MAY14' then timerang 0 21 7 30 0 21 12 10;end
if fname='MAY16' then timerang 0 20 37 20 0 20 46 20;end
if fname='MAY18' then timerang 0 18 20 10 0 18 26 40;end
if fname='MAY23' then timerang 0 20 0 20 0 20 6 40;end
if fname='MAY26' then timerang 0 18 48 20 0 18 55 20;end
if fname='MAY30' then timerang 0 20 43 30 0 20 49 10;end
if fname='JUN01' then timerang 0 21 4 30 0 21 12 40;end
if fname='JUN02' then timerang 0 18 39 10 0 18 45 10;end
if fname='JUN11' then timerang 0 19 16 0 0 19 22 0;end
if fname='JUN17' then timerang 0 19 21 10 0 19 28 20;end
if fname='JUN21' then timerang 0 13 48 30 0 14 0 40;end
if fname='JUN25' then timerang 0 18 6 20 0 18 19 10;end
if fname='JUN28' then timerang 0 17 37 30 0 17 45 20;end
```

```
if fname='JUL02' then timerang 0 19 1 40 0 19 10 50;end
if fname='JUL05' then timerang 0 15 57 50 0 16 5 0;end
if fname='JUL10' then timerang 0 17 5 30 0 17 11 10;end
if fname='JUL14' then timerang 0 15 36 30 0 15 42 30;end
if fname='JUL19' then timerang 0 17 30 20 0 17 41 40;end
if fname='JUL23' then timerang 0 16 1 10 0 16 7 0;end
if fname='JUL28' then timerang 0 16 11 20 0 16 17 20;end
if fname='JUL31' then timerang 0 15 59 30 0 16 5 20;end
if fname='AUG04' then timerang 0 16 26 0 0 16 31 30;end
if fname='AUG08' then timerang 0 15 11 0 0 15 16 30;end
if fname='AUG11' then timerang 0 12 31 50 0 12 39 30;end
if fname='AUG14' then timerang 0 13 49 40 0 13 59 40;end
if fname='AUG17' then timerang 0 11 51 20 0 11 59 10;end
if fname='AUG20' then timerang 0 10 57 20 0 11 5 40;end
if fname='AUG22' then timerang 0 13 10 20 0 13 21 0;end
if fname='AUG25' then timerang 0 16 5 10 0 16 16 20;end
if fname='AUG29' then timerang 0 9 36 10 0 9 42 0;end
if fname='SEP01' then timerang 0 14 7 40 0 14 18 30;end
if fname='SEP03' then timerang 0 14 20 0 14 42 20;end
if fname='SEP05' then timerang 0 10 44 0 0 10 55 50;end
if fname='SEP08' then timerang 0 12 11 0 0 12 20 30;end
if fname='SEP13' then timerang 0 11 54 20 0 12 0 50;end
if fname='SEP15' then timerang 0 11 44 0 0 11 53 0;end
if fname='SEP18' then timerang 0 10 46 20 0 10 53 10;end
if fname='SEP22' then timerang 0 8 48 10 0 8 56 0;end
if fname='SEP25' then timerang 0 11 34 10 0 11 43 50;end
if fname='SEP27' then timerang 0 11 25 30 0 11 35 50;end
if fname='OCT01' then timerang 0 9 55 10 0 10 2 0;end
if fname='OCT05' then timerang 0 11 24 20 0 11 34 30;end
if fname='OCT12' then timerang 0 11 25 0 0 11 36 30;end
if fname='OCT18' then timerang 0 8 3 40 0 8 12 0;end
if fname='OCT22' then timerang 0 8 31 10 0 8 39 30;end
if fname='OCT30' then timerang 0 11 55 10 0 12 1 10;end
if fname='NOV03' then timerang 0 9 57 50 0 10 9 40;end
if fname='NOV07' then timerang 0 9 13 40 0 9 24 50;end
if fname='NOV10' then timerang 0 9 31 0 0 9 42 50;end
if fname='NOV14' then timerang 0 6 11 20 0 6 25 10;end
$if fname='NOV17' then timerang 0 4 19 20 0 4 27 40;end
if fname='NOV21' then timerang 0 7 33 20 0 7 41 0;end
if fname='NOV24' then timerang 0 4 10 0 0 4 17 40;end
if fname='DEC01' then timerang 0 3 59 0 0 4 17 10;end
if fname='DEC04' then timerang 0 7 28 30 0 7 39 10;end
if fname='DEC07' then timerang 0 3 8 10 0 3 25 10;end
if fname='DEC11' then timerang 0 3 26 10 0 3 38 30;end
if fname='DEC14' then timerang 0 1 47 0 0 1 57 50;end
if fname='DEC17' then timerang 0 3 19 0 0 3 29 50;end
if fname='DEC20' then timerang 0 5 9 20 0 5 19 30;end
if fname='DEC24' then timerang 0 5 24 10 0 5 32 0;end
if fname='DEC28' then timerang 0 2 26 20 0 2 34 40;end
if fname='JAN01' then timerang 0 4 12 0 0 4 19 10;end
end;
if calset=2 then
type 'Using calset 2.'
if fname='MAR01' then timerang 0 1 12 0 0 1 21 40;end
if fname='MAR06' then timerang 0 23 36 30 0 23 44 0;end
if fname='MAR09' then timerang 0 0 29 50 0 0 35 0;end
if fname='MAR13' then timerang 0 19 21 50 0 19 35 0;end
if fname='MAR17' then timerang 0 19 54 20 0 20 1 0;end
if fname='MAR19' then timerang 0 0 49 50 0 0 55 20;end
if fname='MAR20' then timerang 0 19 13 30 0 19 19 10;end
if fname='MAR28' then timerang 0 2 17 50 0 2 20 30;end
if fname='MAR30' then timerang 0 0 37 0 0 0 42 50;end
if fname='APR06' then timerang 0 0 50 20 0 0 55 50;end
if fname='APR11' then timerang 0 20 16 0 0 20 22 40;end
if fname='APR19' then timerang 0 23 15 40 0 23 20 20;end
if fname='APR25' then timerang 0 21 21 30 0 21 26 20;end
if fname='APR28' then timerang 0 23 15 40 0 23 27 10;end
if fname='APR29' then timerang 0 16 50 10 0 16 55 30;end
```

```
if fname='MAY02' then timerang 0 21 3 50 0 21 13 10;end
if fname='MAY09' then timerang 0 21 25 40 0 21 31 40;end
if fname='MAY12' then timerang 0 23 14 20 0 23 19 40;end
if fname='MAY14' then timerang 0 20 52 10 0 20 57 10;end
if fname='MAY16' then timerang 0 20 58 20 0 21 4 10;end
if fname='MAY18' then timerang 0 18 3 40 0 18 10 0;end
if fname='MAY23' then timerang 0 19 41 50 0 19 47 50;end
if fname='MAY26' then timerang 0 18 48 20 0 18 55 20;end
if fname='MAY30' then timerang 0 21 3 30 0 21 9 0;end
if fname='JUN01' then timerang 0 20 40 20 0 20 51 50;end
if fname='JUN02' then timerang 0 18 51 0 0 18 57 40;end
if fname='JUN11' then timerang 0 19 0 30 0 19 10 40;end
if fname='JUN17' then timerang 0 19 7 50 0 19 14 50;end
if fname='JUN21' then timerang 0 14 6 40 0 14 13 20;end
if fname='JUN25' then timerang 0 18 32 10 0 18 43 50;end
if fname='JUN28' then timerang 0 17 24 0 0 17 31 50;end
if fname='JUL02' then timerang 0 18 38 10 0 18 50 0;end
if fname='JUL05' then timerang 0 16 10 50 0 16 17 50;end
if fname='JUL10' then timerang 0 17 22 10 0 17 27 40;end
if fname='JUL14' then timerang 0 15 20 40 0 15 26 20;end
if fname='JUL19' then timerang 0 17 46 50 0 17 52 40;end
if fname='JUL23' then timerang 0 15 46 20 0 15 52 30;end
if fname='JUL28' then timerang 0 15 53 40 0 15 59 20;end
if fname='JUL31' then timerang 0 15 41 50 0 15 47 30;end
if fname='AUG04' then timerang 0 16 44 0 0 16 49 30;end
if fname='AUG08' then timerang 0 15 28 30 0 15 34 0;end
if fname='AUG11' then timerang 0 12 45 0 0 12 52 30;end
if fname='AUG14' then timerang 0 14 4 40 0 14 10 40;end
if fname='AUG17' then timerang 0 11 38 20 0 11 45 50;end
if fname='AUG20' then timerang 0 11 10 10 0 11 17 20;end
if fname='AUG22' then timerang 0 12 49 20 0 12 58 40;end
if fname='AUG25' then timerang 0 16 21 30 0 16 26 50;end
if fname='AUG29' then timerang 0 9 24 30 0 9 31 40;end
if fname='SEP01' then timerang 0 14 24 0 0 14 29 30;end
if fname='SEP03' then timerang 0 14 54 30 0 15 3 10;end
if fname='SEP05' then timerang 0 11 7 0 0 11 14 20;end
if fname='SEP08' then timerang 0 12 25 30 0 12 32 20;end
if fname='SEP13' then timerang 0 12 6 10 0 12 12 40;end
if fname='SEP15' then timerang 0 11 58 20 0 12 4 50;end
if fname='SEP18' then timerang 0 10 34 30 0 10 41 20;end
if fname='SEP22' then timerang 0 9 1 0 0 9 7 30;end
if fname='SEP25' then timerang 0 11 49 10 0 11 55 20;end
if fname='SEP27' then timerang 0 11 41 10 0 11 47 10;end
if fname='OCT01' then timerang 0 9 43 30 0 9 50 10;end
if fname='OCT05' then timerang 0 11 40 0 0 11 45 50;end
if fname='OCT12' then timerang 0 11 42 0 0 11 48 20;end
if fname='OCT18' then timerang 0 8 17 30 0 8 25 10;end
if fname='OCT22' then timerang 0 8 17 10 0 8 25 10;end
if fname='OCT30' then timerang 0 11 43 20 0 11 49 30;end
if fname='NOV03' then timerang 0 10 15 40 0 10 22 0;end
if fname='NOV07' then timerang 0 9 30 20 0 9 36 20;end
if fname='NOV10' then timerang 0 9 48 20 0 9 54 30;end
if fname='NOV14' then timerang 0 5 48 50 0 5 58 50;end
$if fname='NOV17' then timerang 0 3 58 50 0 4 12 50;end
if fname='NOV21' then timerang 0 7 20 30 0 7 27 50;end
if fname='NOV24' then timerang 0 4 23 10 0 4 30 10;end
if fname='DEC01' then timerang 0 4 23 10 0 4 32 20;end
if fname='DEC04' then timerang 0 7 44 40 0 7 50 10;end
if fname='DEC07' then timerang 0 3 31 10 0 3 39 20;end
if fname='DEC11' then timerang 0 3 44 30 0 3 53 20;end
if fname='DEC14' then timerang 0 2 3 50 0 2 12 0;end
if fname='DEC17' then timerang 0 3 19 0 0 3 29 50;end
if fname='DEC20' then timerang 0 4 55 50 0 5 3 20;end
if fname='DEC24' then timerang 0 5 10 50 0 5 18 20;end
if fname='DEC28' then timerang 0 2 39 40 0 2 46 30;end
if fname='JAN01' then timerang 0 4 24 10 0 4 30 20;end
end;
if (timerang(2) = 0 & timerang(3) = 0 ) then
```

```
 type 'failed to set timerang in proc calit.';exit
 exit
end

gowt('getjy')
sources '0414+053','0424+020',''
calsour '0424+020',''
soucode ''; qual -1; calcode ''; timerang 0; subarray 0
antennas 0; selband -1; selfreq -1; freqid -1;opcode ''; smotype ''
interpol '2PT'; intparm 0; gainver 0; gainuse 0; snver 0; gainver 0
$ this depends on the previous run on setpcal to set refant
snver 2;gowt('clcal');snver 1
sources '0137+331','';calsour '0137+331','';interpol 'self'
gowt('clcal')
interpol '2PT'; sources '0542+498','';calsour '0424+020',''
snver 2;gowt('clcal');ret;fin


proc dosplit
qual -1; calcode ''; timerang 0; stokes ''; bchan 1; bpver -1
smooth 0; douvcomp -1; aparm 0; docalib 1; gainuse 0; dopol -1
blver -1; flagver 0; doband -1; selband -1; selfreq -1; freqid -1
chansel 0; bif 0; eif 0; outdisk=indisk; outclass 'calib'
gowt('split')

oname= subst(sources(1),1,4) !! fname
inna sources(1); inclass 'calib'; outname=oname;rename
FINISH
$
$proc GETCC - sets ncomp to the last acceptable clean component
$take up to factor times the first negative CC
$then copies to a new CC table only the acceptable CC's and
$calls CCMRG on the new table
proc GETCC(factor)
type '## getcc:'; userid 0; invers 1; ecount 0; flux 0
gowt('ccfnd'); keyword 'nthcc'; gethead; ecount = keyvalue(1)
type '## ecount is',ecount; inext 'cc'; invers 1; outvers 2
clroname; bcount 1; optype 'copy'; aparm 0; keyword ''
keyvalue 0; keystrng ''; timerang 0; gowt('tabed')
invers 2; outvers 3; gowt('ccmrg')
invers 3; factor 0; gowt('ccfnd')
keyword 'nthcc'; gethead
ncomp(1) = keyvalue(1); type '## ncomp is',ncomp(1)
ret;fin

$proc obox - sets boxes for 0414
proc obox
$find B
if (carray = 0) then
  blc 93 150 1;trc 120 178 1
  doinvers -1; imstat
  imsize 4 4;prtlev -1;maxfit
  cbx=pixxy(1);cby=pixxy(2)
else type 'using C array paramters'
  cbx = 234.29; cby=292.30;end
if (error > 0) then prpnd; type 'error in maxfit (obox)';exit;end
$calculate positions of other components
ca1x=cbx - 19.43;ca1y=cby - 64.20
round(ca1x,0,x0);ca1x = x0;round(ca1y,0,x0);ca1y=x0
ca2x=cbx - 23.77;ca2y=cby - 50.96
round(ca2x,0,x0);ca2x=x0;round(ca2y,0,x0);ca2y=x0
ccx=cbx + 45.65;ccy=cby - 54.30
round(ccx,0,x0);ccx=x0;round(ccy,0,x0);ccy=x0
round(cbx,0,x0);cbx=x0
round(cby,0,x0);cby=x0
nbox 4
clbox(1,1)=ca1x - 3;clbox(2,1)=ca1y - 3; clbox(3,1)=ca1x + 3;
 clbox(4,1)=ca1y + 3
```

```
clbox(1,2)=ca2x - 3;clbox(2,2)=ca2y - 3; clbox(3,2)=ca2x + 3;
 clbox(4,2)=ca2y + 3
clbox(1,3)=cbx - 3;clbox(2,3)=cby - 3; clbox(3,3)=cbx + 3;
 clbox(4,3)=cby + 3
clbox(1,4)=ccx - 3;clbox(2,4)=ccy - 3; clbox(3,4)=ccx + 3;
 clbox(4,4)=ccy + 3
ret;fin
$
proc pflux
pixxy 65.0 65.0;imsize 10 10
outname ''; outclass ''; outseq 0; ngauss 1; ctype 0; gmax 0; gpos 0
niter 0; domax 1; dowidth 1; dooutput -1; offset 0; domodel -1; outfile ''
imsize 5 5;maxfit;maxfit;p=pixval*1000.0
ret;FINISH
$
proc bflux
obox;blc = (cbx-3),(cby-3),1; trc = (cbx+3),(cby+3),1
doinvers -1; imstat; tmp=pixval; prtlev -1; imsize 3 3
maxfit;b=pixval*1000.0;if (error > -1) then b=0.0;error=-1;end
$ check for sanity
tmp=(tmp-pixval) / pixval
if (tmp > .005) then b=-1;end
if (tmp < -.03) then b=-2;end
ret;FINISH
$
$getnoise - get noise in image of 0414 (uses a box west of the images)
proc getnoise
if (carray = 0) then blc 192 11  1;trc 246 246 1
else type 'using C array parameters';
blc 415 11; trc 500 500;end
doinvers -1;imstat; imnoise= 1000*pixstd;ret;fin
$
proc outpflux
pflux; type '## pflux',pflux; ret;fin
$
$boxflux - add up the clean components in the clean boxes centered on each source
proc boxflux
 a1=0;a2=0;b=0;c=0
 inext 'cc'; invers 0;outvers 0
 gowt('ccmrg')
 keyword 'num row'; getthead; numrow=keyval(1)
 keyword 'cdelt1';gethead; cdeltx=keyvalue(1)
 keyword 'cdelt2';gethead; cdelty=keyvalue(1)
 keyword 'crpix1'; gethead; xref=keyval(1)
 keyword 'crpix2'; gethead; yref=keyval(1)
 for ival= 1 to numrow
   pixxy ival 2; tabget; xpix=keyval(1)/cdeltx + keyval(2)/cdeltx + xref
   pixxy ival 3; tabget; ypix=keyval(1)/cdelty + keyval(2)/cdelty + yref
   pixxy ival 1; tabget; flux=keyval(1)*1000 + keyval(2)*1000
   if (ival < 15) then type ival,xpix,ypix,'flux',flux;end
$ A1 flux
   tmpx = ABS(xpix-ca1x); tmpy = ABS(ypix-ca1y)
   if (tmpx < 5 & tmpy < 5) then a1=a1+flux
     flux=0;end
$A2 flux
   tmpx = ABS(xpix-ca2x); tmpy = ABS(ypix-ca2y)
   if (tmpx < 5 & tmpy < 5) then a2=a2+flux
     flux=0;end
$B flux
   tmpx = ABS(xpix-cbx); tmpy = ABS(ypix-cby)
   if (tmpx < 5 & tmpy < 5) then b=b+flux
     flux=0;end
$C flux
   tmpx = ABS(xpix-ccx); tmpy = ABS(ypix-ccy)
   if (tmpx < 5 & tmpy < 5) then c=c+flux
     flux=0;end
$be paranoid
   if (flux <> 0) then type 'Lost CC in boxflux',ival;exit;end
```

```
 end;
$get rid of the left over CC table
inext ’cc’;invers 0;extdest
$print out results
head(’Object Flux Density (mJy) from clean components’)
type ’A1+A2’,a1+a2; type ’B ’,b; type ’C ’,c; prpnd
ret;fin
$
proc outbox
$ put out the observation date from the header
 keyword ’DATE-OBS’; gethe
 type ’## Observation Date’,keystrng
$ now get the fluxes
 boxflux; getnoise
 type ’### 0414boxflux’,a1+a2,b,c,imnoise
$outputs fluxes in order a1,a2,b,c in mJy then image noise in mJy/Beam
 ret;fin
$
$
$proc pbox - set boxes for 0424
proc pbox
$find the source
blc 57 57  1; trc 72 72  1
doinvers -1; imstat; imsize 5 5; maxfit
nboxes 1
round(pixxy(1),0,x0); pixxy(1)=x0; cpx=x0
round(pixxy(2),0,x0); pixxy(2)=x0; cpy=x0
clbox(1,1)=pixxy(1) - 3; clbox(2,1)=pixxy(2) - 3
clbox(3,1)=pixxy(1) + 3; clbox(4,1)=pixxy(2) + 3
ret;fin
$
$
$ grind - read in from tape and then reduce one observation
$   set wdisk and fname before use
proc grind
  $output version numbers
  type subst(utilver,1,60)
  type subst(vername,1,59)
  head(’Begin Observation’)
  type ’### filename=’,fname
  loaduv;
  inna = fname; inclass ’’; inseq 0;indisk=wdisk
  histid; calit; sources ’0414+053’,’’; dosplit
  type ’##removing multisource database’
  inna=wname; incla ’’; intype ’uv’; indisk=wdisk
  zap;recat

  $now do a map to set the clean boxes, first self-cal to a model
  head(’Phase-cal and making an initial map of 0414+053’)
  inna oname; incl ’’; inseq 0
  setpcal; aparm(9) 1
  in2di mdisk; in2na ’0414model’; in2cl ’ICLN’
  ncomp 0;cmethod ’dft’; gowt(’calib’)
  incl ’calib’; inseq 1; zap; recat;clr2na

  setmx; inname = oname;incl=’’;inseq 0
  outname=inna; outclass ’’; in2disk = wdisk
  gowt(’mx’);wzap

  $set the clean boxes and get the first cc model
  head(’Setting clean boxes for initial 0414 CC model’)
  incl ’icln’; intype ’ma’; indisk=wdisk
  obox; zap; recat;incl ’CALIB’;inseq 0; innname=oname
  setmx; nbox 4; gowt(’mx’);wzap

$ do the calibration for 0414
   for count=1 to 20
     type ’## Begin 0414 calibration iteration’,count
```

```
     inna=oname;incl 'ICLN'; inseq 0; getcc(2)
     nctmp = ncomp(1); getnoise;oldnoise=imnoise
     prpnd; type 'Using',nctmp,'clean components.'
     type 'interation=',count
     type 'image noise=',imnoise; prpnd

     prpnd; type 'Setting Clean Boxes';obox; prpnd

     $change the name of the old data set
     $so that we can easily zap it when calib is done
     inna=oname; incl 'calib'; outna =inna
     outclass 'cal'; outseq 0; rename

     setpcal;in2na=oname; in2cl='icln';in2seq=0
     inna=oname; incl='cal';inseq=0
     outname=oname; outcl ''; outseq=0
     if (count < 2) then aparm(9)=1;end
     ncomp(1) = nctmp; type 'using',ncomp(1),'Clean Components'
     if (count > 2) then solint = 0.5;end
$     if (count > 3) then solint = 0.33333;end
     gowt('calib')

     type 'cleaning up old uvdata.'
     inclass 'cal';intype 'uv'; indisk=wdisk;zap

     type 'cleaning up old map.'
     inna=oname; incl='icln'; indisk=wdisk;inseq=0;intype 'ma'
     zap; recat

     setmx;nbox 4;incl='calib';inseq=0;in2disk=wdisk;gowt('mx')
     wzap;incl 'icln';obox
     getnoise; diff=(imnoise - oldnoise) / oldnoise * 100
     type '##diff is',diff
$ cannot end on first iteration
     if (count=1) then diff = -10;end
     if (diff > -0.05) then ctmp=count;count=20;prpnd;prpnd;prpnd;end
   end;

   type 'cleaning up old map.'
   inna=oname; incl='icln'; indisk=wdisk;inseq=0;intype 'ma'
   zap; recat

$make final map
   prpnd; head 'making final map of 0414 residuals';prpnd
   setmx;nbox 4;incl='calib';inseq=0;in2disk=wdisk
   bmaj -1; gowt('mx');wzap
$move the residual map to a new name
$and make the final CLEAN map
   incl 'icln'; intype 'ma';rname=fname !! 'res'
   outname rname;userid 0; outclass 'imap';outseq 0; rename
$now make the clean map
   head('restoring the CLEAN components for the final map')
   inname rname; incl 'imap'; blc 0; in2na rname; in2cl incl
   outname oname; outcl 'icln'; niter 0; bmaj 0;bmin 0; bpa 0
   gowt('rstor');clr2na; inna oname;incl 'icln'
$find fluxes by adding CC's
   outbox
$do some JMFIT'ing
$label the output file
   type '## 0414 self-calibration iterations =',ctmp
   userid 0; ctype 0; gmax 0; gpos 0; gwidth 0; niter 0
   domax 1; dopos 1; dowidth 1;docrt 1; outprint ''
   dooutput -1; offset 0; domodel -1
$fit A1-A2 simultaneously with free positions
   type '## A1 and A2'; obox
   gpos(1,1)=ca1x;gpos(2,1)=ca1y
   gpos(1,2)=ca2x;gpos(2,2)=ca2y
```

```
   ngauss 2; outname ''; outclass '';
   tmpx=ca2x-16; tmpy=ca1y-16
   blc tmpx,tmpy,1
   tmpx=ca1x+16;tmpy=ca2y+16
   trc tmpx,tmpy,1
   niter 100; gowt('jmfit')
$fit B alone
   obox; type '## B alone'; ngauss 1
   gpos(1,1)=cbx;gpos(2,1)=cby
   blc = (cbx - 16),(cby - 16),1
   trc = (cbx + 16),(cby + 16),1
   gowt('jmfit')
$fit C alone
   type '## C alone'; ngauss 1
   gpos(1,1)=ccx;gpos(2,1)=ccy
   blc = (ccx - 16),(ccy - 16),1
   trc = (ccx + 16),(ccy + 16),1
   gowt('jmfit')

$save the goods off to our data disk
   tname = 'XTAPE:' !! oname
   outfile = tname !! '.icln'
   intype 'ma';incl 'icln';inna oname
   dostokes -1; dotable 1; dotwo -1; donewtab 1; format 0
   gowt('fittp'); zap; recat
   outfile = tname !! '.calib'; incl 'calib';intype 'uv'
   gowt('fittp');zap; recat

   outfile = tname !! '.resid'; intype 'ma'; incl 'imap'
   inna rname; dostokes -1; dotable 1; dotwo -1; donewtab 1
   format 0; gowt('fittp'); zap; recat
ret;fin

proc doit(fname)
clrtemp
month = subst(fname,1,3); day = value(subst(fname,4,6))
$ test for C-array data
carray = 0
if (month = 'SEP' & day > 12) then carray=1;end
if ( month = 'OCT' ! month = 'NOV' ! month = 'DEC')
the carray=1;end
if ( month = 'JAN') then carray = 1 end;
type 'C array = ' !! char(carray)
grind; savemsg
ret;fin

clrall
$set up a few things
reference = 4;mdisk = 2;wdisk = 5;bad
$ output version number
type subst(utilver,1,60)
type subst(vername,1,59)
```

Bibliography

Alard, C., Mao, S., & Guibert, J., 1995, *Astronomy & Astrophysics* **300**, L17

Alcock, C., Akerlof, C., Allsman, R., *et al.*, 1993, *Nature* **365**, 621

Aller, M., Aller, H., & Hughes, P., 1992, *Ap.J.* **399**, 16

Angonin-Williame, M., Vanderriest, C., Hammer, F., & Magain, P., 1994, *Astronomy & Astrophysics* **281**, 388

Annis, J. & Luppino, G. A., 1993, *Ap.J. (Letters)* **407**, L69

Aubourg, E., Bareyre, P., Breehin, P., *et al.*, 1993, *Nature* **365**, 623

Baldwin, J., Beckett, M., Boysen, R., Burns, D., Buscher, D., Cox, G., Haniff, C., Mackay, C., Nightingale, N., Rogers, J., Scheuer, P., Scott, T., Tuthill, P., Warner, P., Wilson, D., & Wilson, R., 1996, *Astronomy & Astrophysics* **306**, 13

Bar-Kana, R., 1996, *Ap.J.*, in press

Bennett, C. L., Lawrence, C. R., Burke, B. F., Hewitt, J. N., & Mahoney, J., 1986, *Ap.J. (Suppl)* **61**, 1

Bertschinger, E., 1996, personal communication

Canizares, C. R., 1981, *Nature* **291**, 620

Clark, B., 1980, *Astronomy & Astrophysics* **89**, 377

Cornwell, T. & Fomalont, E. B., 1989, in R. A. Perley, F. R. Schwab, & A. H. Bridle (eds.), *Sythesis Imaging in Radio Astronomy*, No. 6 in Conference Series, pp 185–197, Astronomical Society of the Pacific

Crane, P. C. & Napier, P. J., 1989, in R. A. Perley, F. R. Schwab, & A. H. Bridle (eds.), *Sythesis Imaging in Radio Astronomy*, No. 6 in Conference Series, pp 139–165, Astronomical Society of the Pacific

Edelson, R. & Krolik, J., 1988, *Ap.J.* **333**, 646

Einstein, A., 1915, *Sitzungsber. Preuss Akad. Wissensch., erster Halbband* p. 831

Ellithorpe, J. D., 1995, *Ph.D. thesis*, M.I.T.

Falco, E. E., Lehár, J., & Shapiro, I. I., 1996, *HST Observations and Models of The Gravitational Lens MG0414+0534*, Submitted to Ap.J.

Grogin, N. A. & Narayan, R., 1996, *Erratum on: A New Model of the Gravitational Lens 0957+561 and a Limit on the Hubble Constant*, Submitted to Ap.J.

Heiles, C., 1993, *The Proposed GBT Correlator*, GBT Memo Series No. 108

Hewitt, J., Burke, B., Turner, E., Schneider, D., Lawrence, C., Langston, G., & Brody, J., 1988, in J. Moran, J. Hewitt, & K. Lo (eds.), *Gravitational Lenses: Proceedings, Cambridge, Massachusetts, USA 1988*, No. 330 in Lecture Notes in Physics, pp 147–158, Springer-Verlag

Hewitt, J., Chen, G., & Messier, M., 1995, *A.J.* **109**, 1956

Hewitt, J., Turner, E., Lawrence, C., Schneider, D., & Brody, J., 1992, *Ap.J.* **104**, 968

Hjorth, P. G., Villemoes, L. F., Teuber, J., & Florentin-Nielsen, R., 1992, *Astronomy & Astrophysics* **255**, L20

Högbom, J., 1974, *Ap.J. (Suppl)* **15**, 417

Hughes, P., Aller, H., & Aller, M., 1992, *Ap.J.* **396**, 469

Katz, C. & Hewitt, J., 1993, *Ap.J. (Letters)* **409**, L9

Katz, C., Moore, C., & Hewitt, J., 1996, Submitted to Ap.J.

Keeton, C. & Kochanek, C., 1995, in C. Kochanek & J. Hewitt (eds.), *Astrophysical Applications of Gravitational Lensing: Proceedings of 173rd Symposium of the IAU*, Kluwer

Kochanek, C., 1991, *Ap.J.* **373**, 354

Kolb, E. W. & Turner, M. S., 1990, *The Early Universe*, Addison-Wesley

Krauss, L. M. & Small, T. A., 1991, *Ap.J.* **378**, 22

Lawrence, C., Cohen, J., & Oke, J., 1995a, *A.J.* **110**, 2583L

Lawrence, C., Elston, R., Jannuzi, B., & Turner, E., 1995b, *A.J.* **110**, 2570

Lebach, D., Corey, B., Shapiro, I., Ratner, M., Webber, J., Rogers, A., Davis, J., & Herring, T., 1995, *Phys. Rev. Lett.* **75(8)**, 1439

Lehár, J., Hewitt, J. N., Roberts, D. H., & Burke, B., 1992, *Ap.J.* **384**, 453

Moore, C. B. & Hewitt, J. N., 1996, *15 GHz Monitoring of the Gravitational Lens MG0414+0534*, Submitted to Ap.J.

Narayan, R., 1991, *Ap.J. (Letters)* **378**, L5

Narayan, R. & Bartelmann, M., 1996, *Lectures on Gravitational Lensing*

Narayan, R. & Nityananda, R., 1986, *Ann.Rev.Astr.Ap.* **24**, 127

Norrod, R. D., 1995, *GBT Surface Accuracy*, GBT Memo Series No. 119

O'Dea, C. P., Baum, S. A., & Stanghellini, C., 1991, *Ap.J.* **380**, 66

Paczynski, B., 1986a, *Ap.J.* **301**, 503

Paczynski, B., 1986b, *Ap.J.* **304**, 1

Patnaik, A. R. & Porcas, R. W., 1995, in C. Kochanek & J. Hewitt (eds.), *Astrophysical Applications of Gravitational Lensing: Proceedings of 173rd Symposium of the IAU*, p. 305, Kluwer

Pelt, J., Hoff, W., Kayser, R., Refsdal, S., & Schramm, T., 1994, *Astronomy & Astrophysics* **286**, 775

Pelt, J., Kayser, R., Refsdal, S., & Schramm, T., 1996, *Astronomy & Astrophysics* **305**, 97

Perley, R., 1990, *The VLA Calibration Manual*, Distributed by the VLA Array Operations Center

Peterson, J. & Falk, T., 1991, *Ap.J.* **374**, L5

Press, W. H., Flannery, B. P., Teukolsky, S. A., & Vetterling, W. T., 1992a, *Numerical Recipes*, Cambridge University Press, 2nd edition

Press, W. H., Rybicki, G. B., & Hewitt, J. N., 1992c, *Ap.J.* **385**, 404

Press, W. H., Rybicki, G. B., & Hewitt, J. N., 1992b, *Ap.J.* **385**, 416

Quirrenbach, A., Witzel, A., Krichbaum, T., Hummel, C., Wegner, R., Schalinski, C., Ott, M., Alberdi, A., & Rioja, M., 1992, *Astronomy & Astrophysics* **258**, 279

Refsdal, S., 1964a, *M.N.R.A.S.* **128**, 295

Refsdal, S., 1964b, *M.N.R.A.S.* **128**, 307

Rickett, B., 1990, *Ann.Rev.Astr.Ap.* **28**, 561

Rybicki, G. B. & Press, W. H., 1992, *Ap.J.* **398**, 169

Schechter, P. L. & Moore, C. B., 1993, *A.J.* **105**, 1

Schild, R. E., 1990, *A.J.* **100**, 1771

Schneider, P. & Schmid-Burgk, J., 1985, *Astronomy & Astrophysics* **148**, 369

Schwab, F., 1984, *A.J.* **89**, 1076

Seljak, U., 1994, *Ap.J.* **436**, 509

Shu, F. H., 1991, *The Physics of Astrophysics: Volume I Radiation*, University Science Books

Simonetti, J., Cordes, J., & Heeschen, D., 1985, *Ap.J.* **296**, 46

Soldner, J., 1804, *Berliner Astron. Jahrb.* p. 161

Spillar, E., 1993, *Ap.J.* **403**, 20

Thompson, A. R., 1989, in R. A. Perley, F. R. Schwab, & A. H. Bridle (eds.), *Sythesis Imaging in Radio Astronomy*, No. 6 in Conference Series, pp 11–37, Astronomical Society of the Pacific

Thompson, A. R., Moran, J. M., & George W. Swenson, J., 1994, *Interferometry and Synthesis in Radio Astronomy*, Krieger Publishing Company

Udalski, A., Szymański, M., Kaluzny, J., Kubiak, M., & Mateo, M., 1992, *Acta Astron.* **42**, 253

Vanderriest, C., Angonin-Willamie, M., & Rigaut, F., 1995, in C. Kochanek & J. Hewitt (eds.), *Astrophysical Applications of Gravitational Lensing: Proceedings of 173rd Symposium of the IAU*, Kluwer

Vanderriest, C., Schneider, J., Herpe, G., Chevreton, M., Moles, M., & Wlérick, G., 1989, *Astronomy & Astrophysics* **215**, 1

Wagner, S., Witzel, A., Heidt, J., Krichbaum, T., Qian, S., Quirrenbach, A., Wegner, R., Aller, H., Aller, M., Anton, K., Appenzeller, I., Eckart, A., Kraus, A., Naundorf, C., Kneer, R., Steffen, W., & Zensus, J., 1996, *A.J.* **111**, 2187

Walsh, D., Carswell, R., & Weymann, R., 1979, *Nature* **279**, 381

Zwicky, 1937, *Phys. Rev* **51**, 290